EXPERIMENTAL INVESTIGATION OF PRESSURIZED CONCRETE TUNNEL LININGS

A THESIS SUBMITTED TO
THE GRADUATE SCHOOL OF NATURAL AND APPLIED SCIENCES
OF
MIDDLE EAST TECHNICAL UNIVERSITY

BY

MÜNCI TUNÇ KALAYCIOĞLU

IN PARTIAL FULFILLMENT OF THE REQUIREMENTS
FOR
THE DEGREE OF MASTER OF SCIENCE
IN
CIVIL ENGINEERING

JUNE 2019

Approval of the thesis:

EXPERIMENTAL INVESTIGATION OF PRESSURIZED CONCRETE TUNNEL LININGS

submitted by **MÜNCI TUNÇ KALAYCIOĞLU** in partial fulfillment of the requirements for the degree of **Master of Science in Civil Engineering Department, Middle East Technical University** by,

Prof. Dr. Halil Kalıpçılar
Dean, Graduate School of **Natural and Applied Sciences** ______________

Prof. Dr. Ahmet Türer
Head of Department, **Civil Engineering** ______________

Prof. Dr. Erdem Canbay
Supervisor, **Civil Engineering Department, METU** ______________

Prof. Dr. Kağan Tuncay
Co-supervisor, **Civil Engineering Department, METU** ______________

Examining Committee Members:

Prof. Dr. Barış Binici
Civil Engineering Department, METU ______________

Prof. Dr. Yalın Arıcı
Civil Engineering Department, METU ______________

Assist. Prof. Dr. Cenan Mertol
Civil Engineering Department, Atılım University ______________

Date:

I hereby declare that all information in this document has been obtained and presented in accordance with academic rules and ethical conduct. I also declare that, as required by these rules and conduct, I have fully cited and referenced all material and results that are not original to this work.

Name, Surname: Münci Tunç Kalaycıoğlu

Signature :

ABSTRACT

EXPERIMENTAL INVESTIGATION OF PRESSURIZED CONCRETE TUNNEL LININGS

Kalaycıoğlu, Münci Tunç
M.S., Department of Civil Engineering
Supervisor: Prof. Dr. Erdem Canbay
Co-Supervisor: Prof. Dr. Kağan Tuncay

June 2019, 125 pages

Behaviour of pressurized tunnels are determined by the mechanical and geometrical properties of lining, mechanical properties and overburden pressure, and the quality of contact zone between rock and lining. These factors form the backbone of the design process of tunnels with internal pressure. Estimating crack widths and damage patterns is challenging due to the nonlinear interaction of natural and artificial layers. In this study, influence of key parameters and FRP-fabric-wrap repairing method were experimentally investigated.

Eight specimens which were %40-scaled replicas of typical cross-section used in Topçam Dam, a reinforced concrete tunnel built into weak rock were tested. 1)No confinement, 2)No confinement fiber reinforced concrete, 3)Low confinement (rock present) 4)High confinement (stressed rock), 5)High confinement and imperfect contact, 6)FRP-repaired high confinement imperfect contact, 7)High confinement and imperfect contact with FRC, and 8)High confinement and improved contact. Mechanical properties of weak rock was simulated with a special light weight concrete composite. Loading of the specimens was done by applying pressure in two orthogonal directions with hydraulic jacks and pressure transmitting sections. Experimental data collection was confirmed with digital image correlation results. The study demonstrated the behaviour of horse-shoe shaped pressurized tunnels using a novel experimental approach, a first in the literature, with the key variables of: in-situ state of stress, contact of lining and mechanical properties of lining. Results showed that the level of confinement strongly affects the behaviour, soffit voids are critical and infringe the assumption of continuous load distribution, FRC does not improve the capacity of the section but distribute crack locations and control crack widths.

Keywords: Tunnel, Pressurized Tunnels, Experimental Investigation, Contact, Weak Rock Tunneling, DIC

ÖZ

İÇ BASINÇLI TÜNELLERDE BETONARME KAPLAMA DAVRANIŞININ DENEYSEL OLARAK İNCELENMESİ

Kalaycıoğlu, Münci Tunç
Yüksek Lisans, İnşaat Mühendisliği Bölümü
Tez Yöneticisi: Prof. Dr. Erdem Canbay
Ortak Tez Yöneticisi: Prof. Dr. Kağan Tuncay

Haziran 2019 , 125 sayfa

Basınçlı tünellerin davranışını, kaplamanın mekanik ve geometrik özellikleri, mekanik özellikleri ve aşırı yük basıncı ve kaya ile kaplama arasındaki temas bölgesinin kalitesi belirler. Bu faktörler, içbasınçlı tünel tasarımının bel kemiğini oluşturur. Doğal ve yapay katmanların doğrusal olmayan etkileşimi nedeniyle çatlak genişliklerinin ve hasar desenlerinin tahmin edilmesi güçtür. Bu çalışmada, temel parametrelerin etkisi ve FRP-kumaş sargı tamir yöntemi deneysel olarak incelenmiştir.

Zayıf kayaya inşa edilmiş betonarme bir tünel olan Topçam Barajında kullanılan tipik kesitlerin %40'lık ölçekli kopyaları olan sekiz örnek test edilmiştir. 1) Kaya Sınırlamasız, 2) Kaya Sınırlamasız, elyaf donatılı beton, 3) Düşük sınırlama (kaya mevcut) 4) Yüksek sınırlama (gerilimli kaya), 5) Yüksek sınırlama ve kusurlu temas, 6) FRP ile tamir edilmiş Yüksek sınırlamalı, kusurlu temas, 7) Yüksek sınırlama ve kusurlu temas, elyaf donatılı beton, ve 8) Yüksek sınırlama ve geliştirilmiş temas. Zayıf kayanın mekanik özellikleri, özel bir hafif beton kompoziti ile elde edildi. Numunelerin yüklenmesi, hidrolik krikolar ve basınç aktarma bölümleri ile iki dikey yönde basınç uygulanarak yapıldı. Deneysel veri toplama, dijital görüntü korelasyon sonuçlarıyla doğrulandı. Çalışma, at nalı biçimli basınçlı tünellerin davranışını, literatürde birincisi olan yeni bir deneysel yaklaşım kullanarak, yerinde stres durumu, kaplama teması ve kaplamanın mekanik özellikleri gibi değişkenlerle göstermiştir. Sonuçlar, sınırlandırma seviyesinin davranışı kuvvetle etkilediğini, altta kalan boşlukların kritik olduğunu ve sürekli yük dağılımının varsayımını ihlal ettiğini, FRC'nin kesitin kapasitesini iyileştirmediğini, ancak çatlak konumlarını dağıttığını ve çatlak genişliklerini kontrol ettiğini göstermiştir.

Anahtar Kelimeler: Tünel, İçbasınçlı Tüneller, Deneysel Araştırma, Temas, Zayıf Kaya Tünelleri, DIC

Necla Tan'a

ACKNOWLEDGMENTS

I would like to thank to my family and friends for their endless support, which could have made "everything" possible.

I would like to express gratitude to Con-Ak Company for post-tension application, and thank our laboratory staff for their effort throughout the study.

Most importantly, for accepting me to the study and giving me insight, I would like to express my deepest appreciation to my supervisors, Professors Erdem Canbay and Kağan Tuncay, and to project members, Professors Barış Binici, Yalın Arıcı, and I. Özgür Yaman, without whom this work would not be possible.

This research was supported by the Scientific and Technological Research Council of Turkey, Grant no: 215M870.

TABLE OF CONTENTS

LIST OF TABLES

TABLES

LIST OF FIGURES

FIGURES

LIST OF ABBREVIATIONS

AAC	Autoclaved Aerated Concrete
DIC	Digital Image Correlation
DSLR	Digital Single-Lens Reflex
DSI	State Hydraulic Works of Turkey
FRP	Fiber Reinforced Polymer Fabric
FRC	Fiber Reinforced Concrete
LVDT	Linear Variable Differential Transducer
METU	Middle East Technical University
PTFE	Polytetrafluoroethylene
TBM	Tunnel Boring Machine
NC	Specimen with No Rock
NCF	Specimen with No Rock, Fiber Reinforced Lining
LC	Specimen with Low Confinement provided by Rock
HCP	Specimen with High Confinement provided by Pre-stressed Rock, Perfect Contact
HCI	Specimen with High Confinement provided by Pre-stressed Rock, Imperfect Contact
HCIR	FRP-Reinforced Specimen with High Confinement provided by Pre-stressed Rock, Imperfect Contact
HCIF	Specimen with High Confinement provided by Pre-stressed Rock, Imperfect Contact, Fiber Reinforced Lining
HCH	Specimen with High Confinement provided by Pre-stressed Rock, Improved Contact

CHAPTER 1

INTRODUCTION

1.1 Pressurized Tunnels

Water gives life to soil and it is the common essential substance for all terrestrial organisms. Societies are formed and thrive around clean water resources since crops were first sown. Irrigation channels were formed to support agricultural societies in the Indus Valley and the Fertile Crescent. Artificial reservoirs for irrigation have been present since 2000 BCE. In Ancient Egypt, the Pharaoh used to tax the farm owners by measuring the water level of Nile, in the same way flood waters were captured to be used in drought season. Another example are the Kareez structures constructed around 800 BCE, which make use of relatively high groundwater table of hills to irrigate croplands on drought season. Some of these structures were lined to reduce permeability of ground, but they were not pressurized conduits, i.e. they worked with open flow channel principles. Energy production using perpetual motion of water is as old as these tunnel structures: Harvesting energy with water-powered mills to grind grains has been common starting from 300 BCE. In the course of industrialization, manner of harvesting energy from nature evolved, as well. Industrial revolution started with the development of steam engine, which revolutionized the waterwheel driven woven techniques. Demand for power production increased in the industrial age and the hunger for energy never ended. Dams were first built in this era, and became widespread around the world before machine age. Hydroelectric power plants with dams are still being used today, and have the largest production share after fossil fueled power plants. In their modern form, these electrical power generating turbines are fed with water from reservoirs with pressurized tunnels.

Dry galleries and tunnels are common in our daily lives: densely populated metropolises have subway systems, cities are connected by rail or motorways which pass through hills and mountains, rather than climbing them. Mining tunnels should also be taken into consideration despite their infrequency. Together with pressurized tunnels, design and analysis parameters and risks during construction stage of all tunnels are similar. However, on their service lives, expected loads and working principles distinguish pressurized tunnels from others. Dry tunnels are built to support the discontinuity created in rock stratum, prevent the gallery from collapsing under overburden pressure, and keep passengers or workers safe inside the tunnel. In the pressurized tunnels, water that is being conveyed through the tunnel threatens the structural integrity of overlying stratum and the tunnel. Specifically, high hydrostatic pressure on tunnel walls might, and often does, shift the stress state of lining to tensile zone, at which the strength of rock and concrete is far more lower than the compressive.

Use of concrete in tunnel constructions is more common and financially beneficial compared to the use of steel, arising from not only the material cost but also the transportation. Despite the fact that hydroelectric power plants are located in relatively remote areas, transportation to mouth of the tunnel is not the only problem during the construction. Long tunnels constructed with drill and blast methodology need continuous conveyance to operate. There is hauled ground matter to be carried outside, and blasting equipment, initial and permanent support of the gallery to be brought to the area of operation. Heavy transportation requirements shape the geometry of the tunnel. There are three conventional tunnel geometry: curvilinear, circular, and horseshoe cross-sections. Curvilinear cross-sections have an arch on top and their side walls are linear, which is not a desired feature since they are weak against horizontal pressure induced by rock. Circular tunnels are ideal in that sense, because they do not have any stress localization areas inherited by their shape. Therefore, close to uniform stress distribution of inner pressure would be experienced by the lining. Unfortunately, with drill and blast operations, it is rather hard to construct a circular concrete lining. Horseshoe sections on the other hand, have arc shaped side walls, close to flat inverts on their bottom side, and an arch for the crown. Construction process is relieved thanks to their flat bottoms, this is why long concrete tunnels are often produced as horseshoe shapes. Still, corners of horseshoe concrete linings experience stress concentration.

Load acting on a pressurized tunnel during its service life is a function of energy grade line of water. That is the elevation of energy head of water, dependent on height difference of reservoirs, roughness of lining surface, and hydraulic radius of tunnel. Most critical locations on pipe systems are the egress or close to downstream, because of high stresses. This is not the case for the pressurized tunnels, since different soil and rock layers exist underground, one tunnel lining might be subjected to various site conditions along its length. Weak rock formations can be present between strong layers which extensively affect the behavior of lining. Rock layers that are squeezing or swelling require to be treated differently at both construction and service stages. After taking the site conditions into account, construction has to be done with high precision and care. Discontinuity at any degree between rock and lining layers have very serious outcomes.

Causes of failure in tunnel structures with inner pressure during construction stage are: flawed characterization of site conditions, mistreatment of surrounding rock, or negligence of material properties. Grobbelaar (1994) offers three possible failure planes connected with the solidification process of lining concrete, first is caused by cold joints due to interruptions in casting process (a in Fig. 1.1). Second failure plane is perpendicular to the tunnel length, and caused by shrinkage of lining concrete (b in Fig. 1.1). The third and the one that is investigated by this study among other parameters is again related with shrinkage: soffit voids that may be present between rock and lining is increased by shrinkage of concrete, leading to failure by internal pressure fluctuations (c in Fig. 1.1). Grouting of the contact zone is prescribed for the soffit void problem, but it is stated that grouting where it is unnecessary, may also damage the lining.

Problems caused by soffit void phenomenon exist in the tunnel considered in this study, which is the energy tunnel of the Topçam Dam at Ordu Province. The 7.5-kilometers-long tunnel is built with drill and blast method, similar to most of the pressurized tunnels in Turkey. The tunnel has a 3.6 meter diameter on its center line. Longitudinal and radial cracks occurred along the length of the tunnel, after the first filling/probation period. Aside from these reasons, experimental investigation of

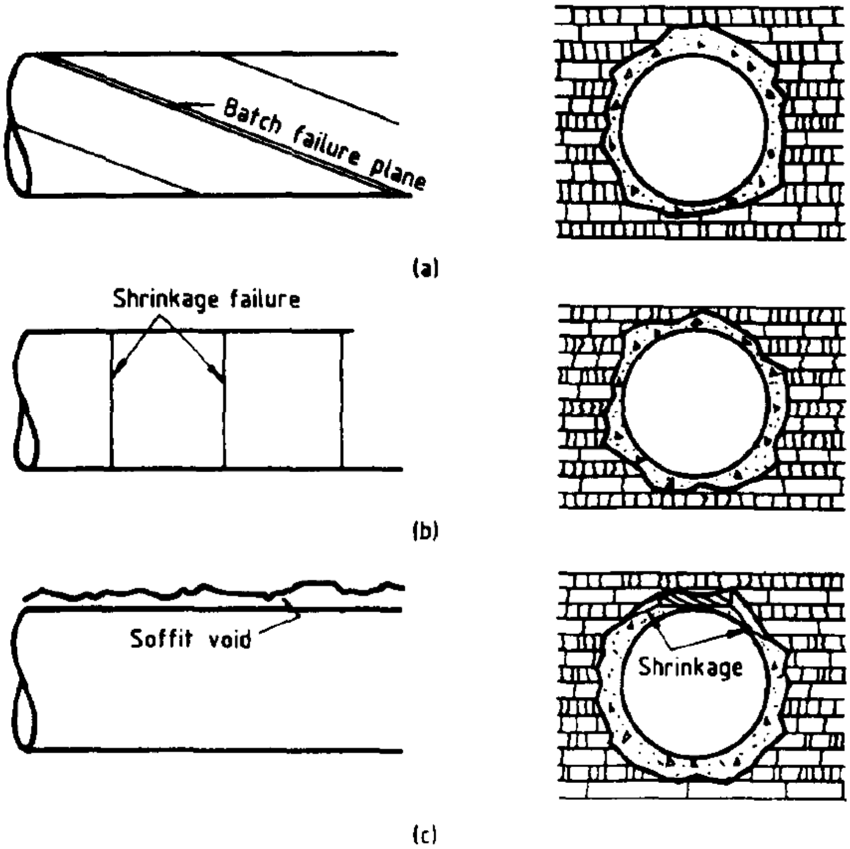

Figure 1.1: Failure modes of tunnel lining until setting, after Grobbelaar (1994)

pressurized tunnels are rare in the literature. Based on these facts, this study presents possible effects of these site conditions along with effects due to material parameters, specifically the use of fiber reinforced concrete linings, based on experimental work. Thanks to its large scope, this work exceeds being a case-study and unveils the behavior of pressurized tunnel linings under extreme conditions.

1.2 Research Needs

Momentum gained by sustainable energy production practices is irrefutable for the past two decades. Hydroelectric power plants (HPP) still covers 49.7 % of the non-fuel based energy production according to IEA, 2018. Same report states that the focus on reservoir-less hydroelectric power generation projects with much smaller capacities are gaining continuous support and interest on large scaled projects are on the decline. Nonetheless, pressurized tunnels are being built regardless of the size of HPPs. Even though pressurized tunneling practice has a collective experience over a century, structural stability issues are still being encountered according to Basnet and Panthi (2018). Base assumption of designing a tunnel lining is that the concrete lining and the surrounding rock mass will act and deform in a unified manner.

Economical convenience and ease of production pushes the contractors to use reinforced concrete linings for the construction of pressurized tunnels. Common practice guidelines in the literature on this subject prescribe an elastic approach. In Turkey, State Hydraulic Works (DSI) is the state agency responsible for planning, managing, execution, and operation of water resources, which includes HPP and most of the pressurized tunnels. Although extensive construction guidelines are provided by the institute, the guidelines do not specify or at least recommend a method for the analysis and design of pressurized tunnels, except that it should be done under three dimensional stress assumptions and in computer environment. The construction works, on the other hand, are streamlined by the specifications. Since weak rock formations are common in Turkey, thorough specifications on the methodology of drilling, boring and grouting applications are present. Documents on the methodology and the equipment for control measurements on dams are sophisticated, while very limited amount of data is required to be gathered from field prior to design steps, according to DSI. The absence of design guidelines in one of the respectable institutes of the government is a great lack of direction, which creates the cornerstone of this study.

Site measurements can be found in the literature that are obtained for health monitoring purposes. But gathering and cross-analyzing data from these on-site measurements with uncontrolled support conditions is a lot harder and unreliable, compared to laboratory results. Very few experimental studies exist that assesses the performance of pressurized reinforced concrete tunnel linings. Since a controlled environment is necessary for a sound generalization and decisive comparison of different cases, it is vital to collect data using experimental work.

1.3 Object and Scope

The goal of this study is to investigate the behavior of reverse-horseshoe shaped pressurized tunnel linings made of reinforced concrete, experimentally. The scope of this study contains literature review, design and construction procedures of experiments, results of experiments, and finally instigation and suggestions for construction of pressurized tunnels.

In order to accurately portray the behavioral changes of tunnel with respect to key parameters, a novel experimental approach was used. Selected key parameters were 1) Degree of in-situ stress active on rock mass, 2) Quality of contact between lining and rock interface, and 3) Addition of synthetic fibers to the concrete recipe. Along with these ground conditions and material properties, the performance of fiber reinforced polymer (FRP) fabric wrap repair method was tested.

Table 1.1: Experimental Program

	NC	NCF	LC	HCP	HCI	HCIR	HCIF	HCH
Overburden	N/A	N/A	Negligible	Ideal	Ideal	Ideal	Ideal	Ideal
Contact	N/A	N/A	Ideal	Ideal	Imperfect			Improved
FRC		✓					✓	✓
	Overburden Group			Control	Contact Group			

Total of eight distinct specimens were built to assess the influence of these three key parameters and one repair method (Table 1.1). First key parameter was investigated by comparing the specimens with no rock, NC, unstressed rock, LC, and the ideal specimen with high overburden pressure, HCP. Consequences of having deficient contact on lining-rock interface was observed with the specimens HCP, HCH and HCI, the ideal specimen, its counterpart with irregular contact loss, and continuous contact loss along its crown, respectively. At two important specimens, NC and HCI, effect of additions of synthetic fiber reinforcements to the lining mixture was observed, with NCF and HCIF. And the performance of FRP wrap was seen at HCIR specimen, which was obtained by repairing HCI specimen.

CHAPTER 2

LITERATURE SURVEY

2.1 Classification of Rocks and Design of Tunnels

In order to design any structure properly, boundary conditions should be well understood. For tunnel structures, rock layer both supports the lining and applies load to it at the same time. Although most critical load is caused by outlying media for dry tunnels, pressurized tunnels are subjected to inside pressure. Complexity of the pressurized tunnel problem is due to the independence of support and loading conditions, which is caused by the variation of rock strength along the tunnels length and the inner pressure. Intensity of loading changes along the length of a tunnel, so does the strength, integrity and characteristics of rock mass surrounding the tunnel. In order to enable comparison between different rock sites, a rock mass classification convention is necessary. Several methods of rock classification exist in the literature and most of them prescribe a unique methodology for tunnel design by using their own parameters. Notable classification methods may be listed as Terzhagi's Method, Q system (RQD), Rock Structure Rating (RSR), and Rock Mechanics Rating (RMR), Geological Strength Index (GSI).

Terzaghi (1943) classified rock types into 9 groups 75 years ago: 1)hard and intact, 2)hard stratified or schistose, 3)massive, moderately jointed, 4)moderately blocky and seamy, 5)very blocky and seamy, 6)completely crushed but chemically intact, 7)squeezing rock, moderate depth, 8)squeezing rock, great depth, 9)swelling rock. Different predictions of load and related precautions were prescribed for every group, from unlined tunnel construction to shortly-spaced thick circular steel ribs.

30 years later, Barton et al. (1973) introduced a more quantitative and complex

method for the classification and load designation: the Q System. Q System uses the calculated rock mass quality value, Q, for the calculation of roof load and for the related empirical design method. Q is found by using the formula given in equation 2.1. It depends on six parameters: Rock quality designation (RQD), joint set number (J_n), joint roughness number(J_r), joint alteration number (J_a), joint water reduction factor (J_w), and stress reduction factor (SRF). Three fractions in equation (2.1) account for the block size, inter-block shear strength, and active stress, respectively.

$$Q = \frac{RQD}{J_n}\frac{J_r}{J_a}\frac{J_w}{SRF} \tag{2.1}$$

Another method for the classification of rock masses was proposed by Wickham et al. (1972), to support its related design method. Rock Structure Rating (RSR) system not only takes the morphology of rocks into account, but also their formation class. Three basic parameters are present in this method, general area geology coefficient (A), joint pattern parameter (B), and ground water parameter (C). RSR value is the sum of these three parameters, and is used along with the diameter of the gallery opening to calculate rock mass load and rib ratio. Later on, empirical equations for determining the thickness of shotcrete layer, spacing of rock bolts and steel ribs are given.

Bieniawski (1973) defined the Rock Mechanics Rating (RMR) system which classifies rock into five classes using six parameters. Parameters depend on uniaxial compressive strength, quality of drill core, joint frequency, joint orientation, joint condition, and water inflow. Following the classification, a design guide for primary support was given for rockbolts, shotcrete and steel ribs. Two decades later, Bieniawski (1993) restated the classification method and the empirical design method that comes with it, with case examples while correlated RMR with Q and RSR systems.

These three methods were correlated with each other in several works: Rutledge (1978), Goel et al. (1995), Palmstrom (2008), Laderian and Abaspoor (2012). Majority of these comparisons were made with local data, and their results reflect the subjectivity of methods. When examined, strong variations can be found between the correlations made by different researchers. This indicates a statistical impossibility, judgments on different sites based on different quantitative and qualitative methods being compared by different people. As originally stated by Wickham (1972) and later directly quoted by Bieniawski (1973), classification of a rock structure to predict ground support is a questionable subject, but an effort towards evaluating significant geological parameters is essential.

Hoek et al. (1995) introduced Geological Strength Index (GSI) for rock mass classification, which requires visual inspection of site conditions and the chart (Fig. 2.2). The design of the classified rock is done with respect to the generalized Hoek-Brown failure criterion, Eqn. 2.2, by Hoek and Brown (1994). Where σ_1, σ_3, represent the major and minor principal stresses, σ_{ci} is the unconfined compressive strength, and m_b, s, and a are material constants calculated by Eqns. 2.3,2.4, and 2.5, respectively. The disturbance factor, D, is a coefficient representing the care used in detonation in D&B method and the precision of TBM head choice, ideal case being represented with 0. The poor choice of D may lead to extremely conservative design, as stated by Hoek and Brown (2018). Material characteristics of rock at Topçam Dam were calculated according to this methodology, which was later improved and practical applications were demonstrated, Hoek and Brown (2018).

$$\sigma_1 = \sigma_3 + \sigma_{ci}\big[m_b\frac{\sigma_3}{\sigma_{ci}} + s\big]^a \tag{2.2}$$

$$m_b = m_i \exp\big[\big(GSI - 100\big)/\big(28 - 14D\big)\big] \tag{2.3}$$

$$s = \exp\big[\big(GSI - 100\big)/\big(9 - 3D\big)\big] \tag{2.4}$$

$$a = 1/2 + 1/6\big[\exp\big(-GSI/15\big) - \exp\big(-20/3\big)\big] \tag{2.5}$$

The deformation modulus for weak rock is estimated using Eqn. 2.6, using GSI value, the disturbance factor D, and the intact rock modulus E_i, according to Hoek and Diederichs (2006). The visual observations at site were interpreted the GSI of fractured andesite between 20-40, laboratory tests indicated that intact rock modulus was 26.5 GPa. For different disturbance factors, result of Eqn. 2.6 is shown on Fig. 2.1. The ideal case, D=0, sets the upper limit for the deformation modulus.

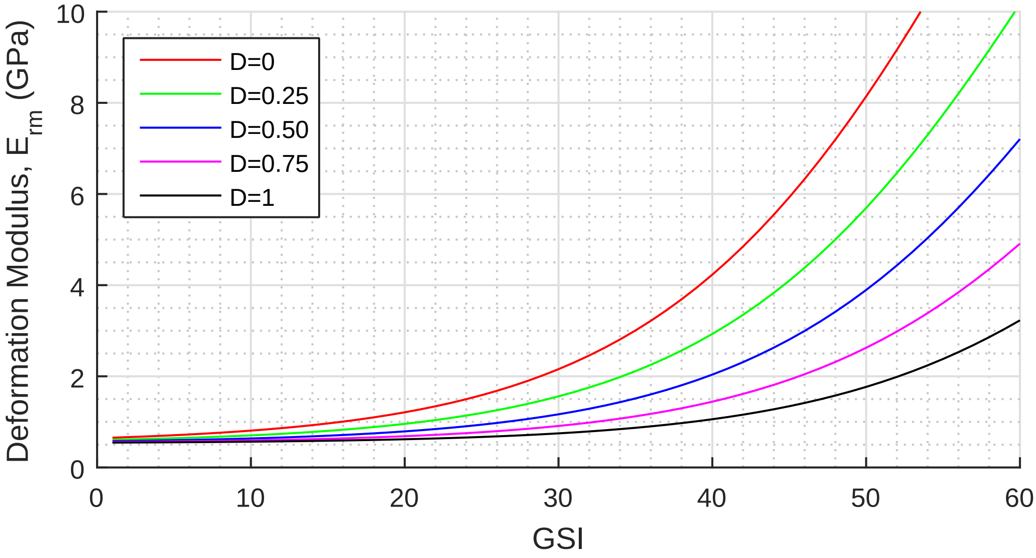

Figure 2.1: Deformation modulus for $E_i = 26.5$ GPa

$$E_{rm} = E_i \left\{ 0.02 + \frac{1 - D/2}{1 + \exp\left[\left(60 + 15D - GSI \right) / 11 \right]} \right\} \tag{2.6}$$

Regardless how rocks are grouped on which system of classification, rheological models state that when a gallery is opened in rock, formation of a plastic zone around the gallery is probable, depending on mechanical properties of the medium and stress and strain states. Kastner (1949) explains this phenomenon by two possibilities, elastic behavior of rock and formation of plastic zone. In the former, rock mass response is elastic and as a result, tangential stress is maximum at the wall of the gallery and radial stress is zero. For the latter possibility, the plastic case, radial and tangential stresses diminish in a continuous fashion from the plastic boundary to the tunnel face. Radius of this plastic zone is calculated with Equation 2.7 where k_p is passive lateral earth pressure, σ_{ci} is unconfined compressive stress, P_0 is hydrostatic pressure acting on rock mass and r is radius of opening. It is also stated that for drill and blast construction techniques, this radius must be amplified by $\%100$ and $\%25$ for normal blasting and controlled blasting respectively.

$$R_P = r \left[\frac{2}{k_p + 1} \left(\frac{\sigma_{ci} + P_0(k_p - 1)}{\sigma_{ci}} \right) \right]^{\frac{1}{k_p - 1}} \tag{2.7}$$

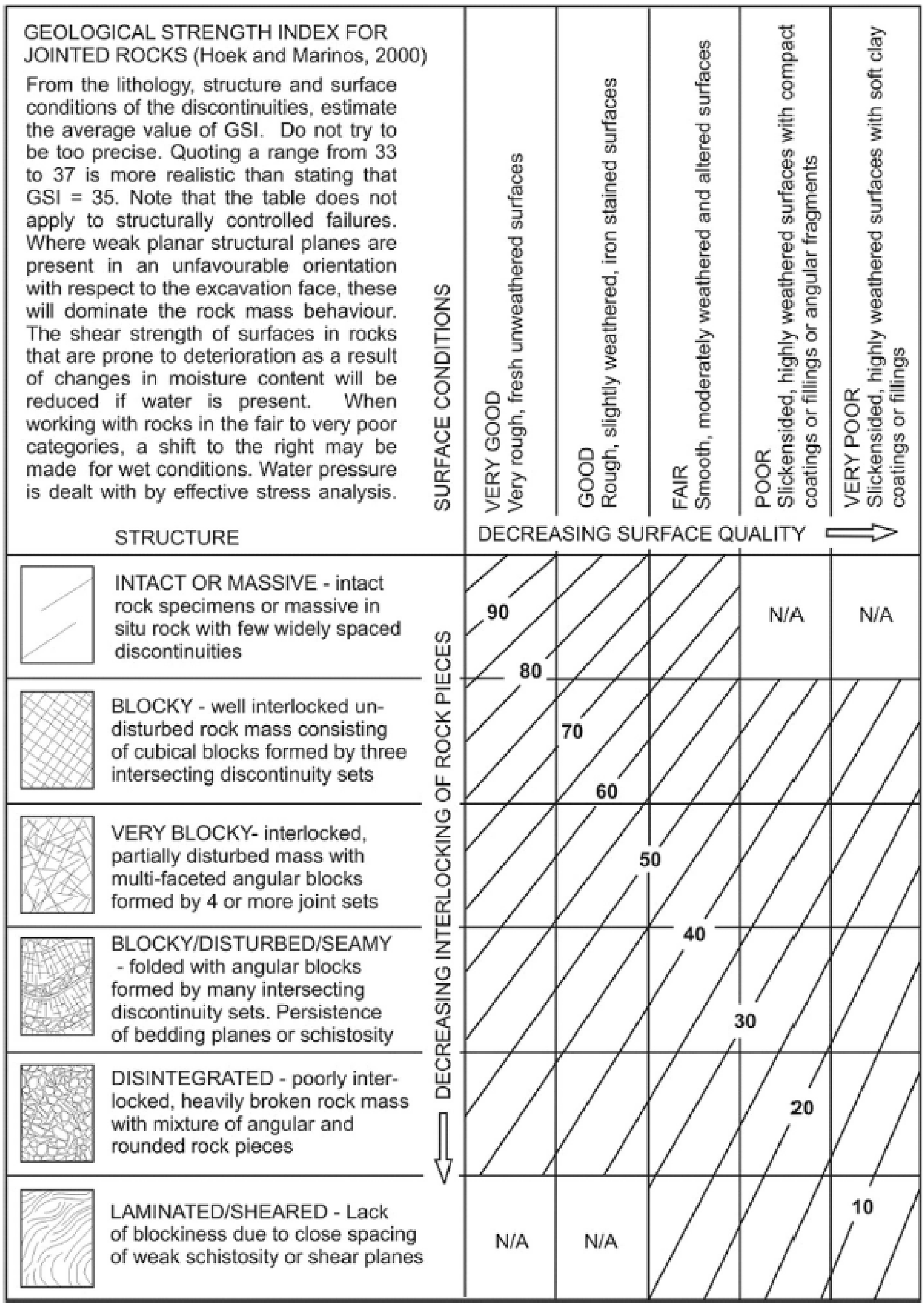

Figure 2.2: GSI chart, after Hoek and Brown (2018)

2.2 Design and Analysis Practices of Pressurized Tunnels

One method for the design of pressurized tunnels is given by Sinha (1989), starting by determining the type of lining: plain concrete liners up to 35 meters of water head (or 0.34 MPa internal pressure), reinforced concrete liners up to 70 meters of water head (0.69 MPa), mild steel liners for 154 meters of water head (1.52 MPa), and steel liners with reinforced concrete lining together from thereon. Following that, minimum thicknesses for steel and concrete linings are prescribed. Design load cases are a) external geological loading on lining without inner hydrostatic pressure, b) sole hydraulic pressure, and c) only external hydraulic pressure, referring to overburden on construction stage, water pressure during service life and leaked water pressure acting outside of tunnel during maintenance procedures, respectively. Internal pressure is considered to be shared by lining and host rock proportional to their elastic moduli and diameters, by applying elastic theory and assuming perfect contact between rock and concrete layers.

Unlined pressure tunnels are common in the Norwegian tunneling practice. When rock mass is durable, impermeable, and overburden pressure acting on it is adequate, unlined pressure conduits are structurally safe, according to Palmstrom (1987). Numerous examples are present in the Norwegian unlined pressure tunnel history, one important case is the unlined inlet tunnel of Nyset-Stegtje HPP: with a maximum water head of 1000 meters. Joint treatments against water leakage on faults and rock layer interfaces were prescribed by Palmstrom (1987). For a realistic factor of safety, FEM approach was introduced and calibrated on existing tunnels that collapsed. After the calibration of the FEM, several other pressurized conduits were analyzed and results were reported to be satisfactory, although all initial factor of safeties (calculated by the ratio of overburden pressure to inner pressure) were replaced. Tunnels in working condition were proven to be safe, and some failed tunnels that initially thought to be safe were accounted for. In the final remarks, a modification for the depth of tunnel was recommended to adjust the factor of safety.

Indian Standard (first edition 1976, first revision 1987) gives very detailed provisions for structural design and construction methods of penstocks and pressure tunnels. On the matter of penstocks, it gives different specifications for surface penstocks, buried penstocks in rock, and special conditions of penstocks . Similarly, for pressure conduits, standard has 7 parts: general design, geometric design, hydraulic design, structural design of concrete lining in rock, structural design of concrete lining in soft strata and soils, tunnel supports and structural design of steel lining. Extensive geological surveys are prescribed to determine joints, rock types, any possible change in the rock pressure, location of groundwater table, and so on. In the structural design of concrete lining in rock part, backfill grouting and pressure grouting is prescribed to fill voids and shrinkage gaps between concrete lining and rock. For backfill grouting, time of application is specified as 21 days after the concrete is casted in place, and maximum pressure is specified as 0.5 MPa. For the pressure grouting, recommended magnitude is 1.5 times of the water pressure. As for the structural design of concrete lining in soft strata and soils, designing circular linings with the thick composite cylinder assumption is adopted by considering uncertainties on material properties and external loads, while for the non-circular linings, photo-elastic studies are prescribed to determine the stress pattern (Chapter IV, 7).

When local regulations are studied, documents on the design and construction methodologies that are found were published by DSI (State Hydraulic Works) and Turkish Standards Institute (TSE). Design of pressurized tunnels is not guided properly in any document published by these institutions. All there is on the subject of pressurized tunnels is guidelines for construction methods and technical specifications by DSI. Pressurized tunnels are mentioned at the documents "Dam Projects - Technical Specifications for Construction", "Technical Specifications for Concrete Works", "Technical Specifications for Sewage Works", and "Technical Specifications for Drilling and Grouting Operations". Criteria on design of pressurized tunnels are stated on "Dam Projects - Technical Specifications for Construction". According to that document, 1) "Design, analysis and dimensioning of all tunnels and conduits are required to be done by using 3-D software.", 2) "Economical survey of tunnel's dimensions, shapes and linings are to be done.", 3) "Details of a contact grouting plan and its details are to be presented with the geotechnical report." and 4) "The determination of diameter and type of the derivation (intake) tunnel must be done by using data from field surveys, expected flow rate, and length, slope and working conditions of the tunnel.". These four criteria form the design guidelines that is applied by DSI for all pressurized tunnels.

The document "Technical Specifications for Drilling and Grouting Operations" by DSI, which is very similar to the approach of the Indian Standard, contact grouting on D&B projects, contact grouting on TBM projects, and consolidation grouting are distinctly demonstrated. A total of 7 grout recipes are given in this document, all of which contain bentonite, first four has plasticiser additives, while last three contain hardening accelerators and sand. Grout pressure of contact grouts at all sections of all tunnels is required to be 0.2 MPa, and grout hole must be bored 15 cm past after lining, and auxiliary lining. It is also said that in the event of having a gap larger than one meter between gallery and lining, this gap will be filled with a concrete mixture that is seen fit by the administration. The grouting operation is assumed to be completed when the grout pressure reaches 0.2 MPa, using 7 successive mixes in the designated amount if necessary. If that is not the case after 10 minutes, grouting must be applied a second time, if the required pressure is still not reached after 20 minutes, the hole will be considered as grouted based on the maximum flow rate (0.6 liter/minute).

2.3 Tunnel Construction

Tunnel construction is mainly done by two methods: Drill and Blast (D&B) or Tunnel Boring Machine (TBM). TBMs can be defined as project oriented drilling machines. They are manufactured as job specific devices, i.e. for different types of ground matter different types of TBMs are needed. It is reported that benefits of TBM is lost with increasing cross-sectional area of tunnel size, by Bruland and Rostami (2016). Moreover, arising from high cost and low maneuverability of TBMs, they are being preferred in transportation oriented tunnel projects.

Jodl and Resch (2011), compared D&B (referred to it as New Austrian Tunneling Method) and TBM methods. The main conclusion was that although TBM provides safer working conditions, required alterations on cutterhead and excavation chamber forced by the variance of material type to be excavated render TBM method to be very sensitive and therefore vulnerable. Conclusion was at this point, a balance of benefits exists for two methods, and method selection is to be made based on length and geological properties of the path.

Typical TBM projects are constructed with %3 gradient, for steeper angles special braking systems are required, reported by Brox (2013). There are examples of specialized TBM-driven tunnels with 30 to 45 degrees inclination. The cost-effectiveness of TBMs greatly vary for pressure-shaft-headrace-tunnel and pressure tunnel systems. When all facts are combined, TBM are useful on railroad tunnels, small scaled highway tunnels, and straight headrace tunnels with pressure shafts but to this day, literature points out that cost-benefit curves of TBMs have to be improved to compete with D&B method.

Rabcewicz (1964) offered an extensive summary of available tunneling methods to his date, and provided detailed examples of shotcreted tunnel practices with the New Austrian Tunneling Method (NATM). The importance of integrity between first applied shotcrete and rock surface was emphasized. Key concepts were the support provided by the initial shotcrete application to rock surface (called auxiliary lining or auxiliary arch), effects in delaying the deformation and improving the intactness of the rock medium. Most important change by NATM was the change of perspective towards ground matter, from a burden to the tunnel to the support of the tunnel. Inner lining is prescribed as just a measure of safety, probably by considering dry tunnels solely.

2.4 Experimental Studies on Tunnels

Physical models for the investigation of tunnels are very scarce in the literature. Since the working principle of segmental tunnels (that are mostly bored with TBM) are very different from that of D&B tunnels, some portion of the experimental work was irrelevant to the scope of this study. However, problems encountered at construction stages of dry and pressurized tunnels are similar. Most of experimental studies on tunnels are transportation oriented tunnels, and the number of pressurized tunnel experiments are negligible compared to experiments on dry tunnels. Small-scaled experiments are more common compared to large-scale experiments.

Lee (1974) conducted small scale experiments to clarify circular openings in stratified rock. Several experimental models shaped as 10 to 30 cm-cubes were loaded and strain analysis was conducted using three dimensional photoelasticity, results of his work was on the effects of stratified rock formations on tunnels. Important remarks were 1- support capacity of one rock layers increase while its thickness, hardness or modulus of elasticity increases, 2- the distance between centers of two layers of rock plays a significant role on the stress concentration factor, 3- Shear stresses are more critical for relatively softer or thinner layers.

Haung et al. (2013) have also studied the stratified rock patterns, in particular the weak interlayer phenomenon. Effects of weak layers between relatively rigid rock masses on unlined galleries were investigated in the study with experimental and numerical models. For the rock substitute, a mix of barite, sand, water and detergent was used. With several models and various parameters, the study presents the interlayer (a thin layer with different characteristics, resembling a fault line) with 50-degree dip that passes through the crown area to be most inconvenient, and the effect of symmetry as beneficial.

Li et al. (2014) studied different types of failures during the construction phase with a 20 cm circular railway tunnel model which was designed with 1:80 similarity ratios of geometry, stress, and elastic modulus. A mixture of barite, silica sand and petroleum jelly was used for the weak rock substitute. A circular gallery with 24 cm radius is opened inside rock substitute. For the measurement method of experiments DIC was used: Digital Speckle Correlation Method. As for the results of this study, a method for speckle generation to be used on the particular DIC method is presented, a material routine that reflects the elastic modulus degradation is developed and implemented to the FLAC code, and shear wedge failure mode that was clearly observed during the experimental work was used to calibrate the finite element model.

Li et al. (2015) analyzed transportation oriented tunnels in mines with a large-scale experimental model. Primary goal of investigation was understanding the collapse mechanisms in order to prevent them. After being excavated and mined, mining galleries are being used as roadways. Not only these tunnels have rectangular shapes, most of them are also located in deep soft rocks, which corresponds to an unideal structural system created in an unfavorable site condition. Study was concluded by stating that the failure characteristics of deep roadways with thick top coal can be prevented from collapsing by providing roof supports. Same phenomenon is studied by Yang et al. (2017), in correspondence with the data collected from Xin'an coal mine. A numerical model is investigated and an optimized support system is proposed against heaving, roof subsidence, bolt failure and side shrinking.

Small-scale circular segmental tunnel model was constructed by Standing and Lau (2017). Main focus of the investigation was on segmental integrity. Outer diameter of the model was 50 mm, the load application was done with screws that are fixed to a relatively rigid outer ring. This concluded that deformation in principle directions increase with increasing number of segments and loose bolts. This study also served as a preliminary study for a large-scale (half scale) experiment by Standing et al. (2015), which investigated effects of tunneling on existing tunnels. Although this study was investigating a segmental dry tunnel design that resides in soft soils and clays, an inspiring loading system consisting 18 actuators was used to apply ground action.

Leung and Meguid (2010), worked on ground-lining interaction with a small-scale experimental approach, specifically the backfill erosion that is common on water pipes or tunnels embedded in soft media. This phenomenon is most often observed on sewage systems, failure of tunnels are sometimes related to contact loss on outer boundary of lining. The physical model was constructed by embedding a 114 mm-radius pipe into soil inside a rigid steel tank. The overburden pressure active on the location of pipe was twice the water pressure. Throughout three experimental models, soil was removed from the ground-lining interface and pressure differences were measured. Local contact loss between tunnel and its support affected the stress distribution of lining significantly.

Jin et al. (2015) have studied the deep spillway outlet of Three Gorges Dam with a 1:6 scaled physical model. Importance of this study from our perspective is the method of inner pressure application to the rectangular gallery located in the middle of concrete dam. During the experiment, at 1.2 MPa inner pressure horizontal cracks have initiated and at 1.93 MPa, vertical cracks have initiated, while horizontals were getting larger. Since this is a case study of a specific project, computer models related to the experiment and conclusions that were drawn were focused on the structural health of the specific dam body. Still, the presented application method of in-situ and inner stress fields are exemplary.

Lin et al. (2015) constructed a physical model of a three dimensional pressurized tunnel with barite, sand expansion soil, and water. The model was small-scaled: Similarity ratio of 1:50 for geometry and 1:400 for stress and modulus of elasticity. For the monitoring system, displacement sensors, strain gauges and acoustic emission were used in the experiment. Ground water pressure was an important variable for the actual tunnel, due to its depth and it was implemented. It was concluded that two pressurized tunnels designed 60 m apart from each other does not influence one another.

2.5 Optical Evaluation Methods

A sophisticated method of strain visualization was discovered by Brewster 200 years ago, while he was investigating the effects of compression and dilatation to refraction of light. When pressure is introduced to crystallized plate specimen, the polarizing force of the specimen increases or diminishes, respective to the direction of applied pressure. The method of using reflective media and polarized light to assess strain condition was and still being studied extensively, by many researchers including Mindlin (1939), Timoshenko (1952), Broniewska et al., Ramesh (2011).

Capturing and reporting strain conditions was being made with hand-drawn diagrams, until the 1888 Kodak Camera, which enabled film photography to be used for testing purposes. Popularity of film photography was later replaced by digital cameras, namely CCD type sensor at 1969 which made recording light as digital output possible, followed by CMOS sensor at 1990s, when it was more cost-efficient. Dominance of digital cameras on the market allowed comparison and correlation of sequential frames much easier. Methods of using light to define deformations had also branched out, for example, diffraction grating strain gauge was developed by Bell in (1959), and enhanced by Pryor and North (1971). This strain gauge was using only the diffraction property of light. By fixing two razor blades to a tension specimen and giving monochromatic light from one side, a diffraction diagram which is dependent on length of gap between razors was obtained on the other side.

Peters et al. (1983) used Digital Image Correlation (DIC) for analysis of rigid body mechanics consisting of large deformations. This work is significant since it was recorded with an analog high speed video camera (8 mm film, 100 fps) and the frames were digitized in order to implement DIC method. Results of DIC using least squares method is reported to be highly accurate for the two dimensional deformation. Rand and Grant (1997) used thin film polymers to mark specimens and a CCD camera to capture deformation of random speckle pattern, which later post processed by a computer to reveal strain condition of the specimen.

Feasibility of digital image correlation increased with the exponentially increasing computational power of computers and image quality of digital cameras after 2000. Tung and Sui (2010) have used DIC on images taken with a 3 MP micro-camera to analyze cracked cylindrical pipes, and compared the results of DIC and FEM. DIC method was reported to be efficient and accurate on locating strain distribution and concentrations. Performance of different type of reinforcements on asphalt pavements were assessed by Romeo and Montepara (2012), using DIC method to record strains on flexural tests. For the experiments where the crack pattern is uncertain or unknown, DIC technique is reported to be useful by Bilotta et al. (2017) who investigated repairing methods of masonry structures by FRCM materials. Performance of adhesive joints were investigated by Sun et al.(2018), to clearly observe the strain evolution and flow within different materials/layers, where DIC method was implemented. Most beneficial feature of DIC is the ability to locate crack patterns and strain localizations before crack is visible to eye, reported by Aghlara (2018), who conducted a pull-out experiment, in order to test 2D capabilities of his DIC method using a mid-range and relatively outdated digital camera (Nikon D80). Overall accuracy of the 2D DIC method for displacement fields were more than %93.

DIC application requires a preparation procedure: the sample to be monitored must be properly marked with high contrast random speckle pattern. Contrast and variance of speckle size directly affect the quality of DIC analysis. Pan et al. (2008) have stated that specimens marked by different people lead to different type of random patterns which affect the result of DIC analysis. Aside from the type and contrast of the speckle pattern, the paint thickness is very important. Creating a layer of paint on top of the specimen may alter the results, so it is best to mark the specimen with discontinuous paint speckles.

To sum up, DIC method must be regarded as a computerized visual inspection. Although locations of relative displacements are accurate, the degree of relative displacements are not always precise. It must be implemented very carefully, since there are numerous variable that can affect the reliability of the measurement. For example, the smallest inclination of initial orientation or disturbance of the camera during experiment may change the results, uneven distribution of randomly generated pattern may cause local losses in resolution. Overall, application of DIC in laboratory is proven to be beneficial.

CHAPTER 3

TEST SPECIMENS

3.1 General

The goal of this study is the experimental investigation of tunnel behavior under inner hydrostatic pressure. For this purpose, eight specimens were prepared in the Structural Mechanics Laboratory (Table 3.1). Models were based on the geometry of the Topçam Dam in Ordu, which is a very typical geometry in Turkey for such tunnels. The specimens were built to a scale factor of 0.4. In the considered tunnel, water sealant joints were present between consequently built lining segments. In regard to this information, all laboratory models were constructed assuming that tunnel is acting on plane stress configuration. Thickness of all elements on laboratory model was 200 mm.

There were five main components of laboratory model: loading system, tunnel lining, rock substitute and in-situ overburden and lateral stress with a prestressing mechanism. The loading system was designed to mimic the field scenario, applying inner hydrostatic pressure to the tunnel lining. Six out of eight experiments were constructed to investigate the behavior of lining surrounded by rock. In order to simulate this behavior, a rock substitute was developed. In five of these experiments, overburden and lateral pressure were present on rock, that is why a prestressing mechanism was built to adjust the stress-strain condition of rock substitute.

Geometrical and mechanical properties of laboratory model were selected in accordance with site evaluations and succeeding computer models. A commercial finite element analysis program (Diana FEA 9.5) was used in the numerical modeling. The scale factor (40%), efficiency of loading system and overburden pressure application method were optimized by means of the numerical models.

3.2 Loading System

On their service states, pressurized tunnel linings are subjected to hydrostatic pressure. The magnitude of pressure for the reference tunnel is approximately 0.8 MPa. Therefore, the ultimate pressure capacity of the loading system of the laboratory model was chosen to be 1.28 MPa, corresponding to a 130 meters of hydraulic head. Literature is rich on experiments where pressure is applied to plane surfaces (Huang, 2013; Li, 2015). Even experiments on overburden capacity of circular cross-sections can be found (Li, 2014; Lin, 2015; Yu, 2017). However, this is not the case in horseshoe shaped pressure tunnels. Application of uniformly distributed load on curved faces of lining is quite a challenge due to its non-continuous geometry. Several approaches were possible to emulate on-site behavior. One possibility was using inflated membranes. This option was seen not feasible due to high order of pressure that is required during the experiments. Rational choice for the loading system was using hydraulic jacks with relatively rigid pressure transmitting sections.

Two orthogonal directions (horizontal and vertical) were considered in the design of the loading system. In each direction, there were one pressure applying core and two pressure transmitting sections. In the core, a hydraulic jack was connected to a load cell by a connector with relatively high rigidity. The loading elements had the same ultimate capacity, 300 kN. Connector sections were designed in accordance with Turkish Standard of Building Code for Steel Structures, to endure the maximum possible load without buckling. Pressure transmitting sections on opposite sides of cores (on 3:00 o'clock and 9:00 o'clock at horizontal, 12:00 o'clock and 6:00 o'clock at vertical direction) had the same geometrical shapes as lining part that they were in touch with (on outer sides), and corresponding geometrical shapes with the core parts on their inner sides (Fig. 3.1).

The pressure transmitting sections were made from eight 8 6-mm thick plates. In each section, four plates located radially, two covered top and bottom sides, other two were on contact zones with core and lining. In other words, each of the four pressure

Experiments	No Confinement	No Confinement Fiber	Low Confinement	High Confinement Perfect Contact	High Confinement Imperfect Contact	High Confinement Imperfect Contact Repaired	High Confinement Imperfect Contact Fiber	High Confinement Half Crown Contact
Experiment Codes	NC	NCF	LC	HCP	HCI	HCIR	HCIF	HCH
Photo			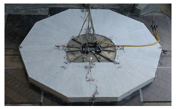		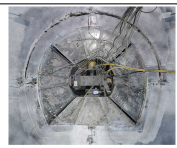	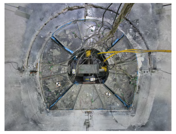		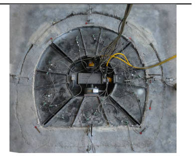
Chronological Order	2	7	1	3	4	5	6	8
Rock-Lining Contact	N/A	N/A	Full	Full	Only Bottom	Only Bottom	Only Bottom	Bottom and Partial Top
Lining	RC	Fiber RC	RC	RC	RC	FRP - RC	Fiber RC	Fiber RC
Overburden	N/A	N/A	Negligible	High	High	High	High	High
Strain Gauges	22	16	32	24	24	24	19	19
LVDTs	12	12	14	18	20	20	20	20
Cameras	2	3	1	3	5	5	6	6

Table 3.1: Properties and instrumentation used in experiments

Figure 3.1: Orthogonal cores of loading system and pressure transmitting sections

transmitting elements resembled an enclosed triple box section. Friction between the laboratory floor and pressure transmitting sections was avoided with four roller ball bearings attached to the bottom of each section. In the contact zone between the tunnel lining and the loading system, two buffer layers were provided. First, due to imperfections on steel surface, 10 mm thick rubber sheets were attached in front of the loading system. Second, on relatively rough and porous surface of concrete, a thin layer of plaster was applied. During the second experiment (Chronologically, first experiment was LC, second was NC), top walls of pressure transmitting sections seemed to deform out of plane. After NC experiment, pressure transmitting sections were examined and no visible plastic deformation were found. Still, since the rigidity of sections was questionable, they were modeled computationally. Results showed that radial plates were affecting load transmission more than anticipated, but not at dangerous levels. In order to ensure a negligibly small deformation in the loading system, its rigidity had to be stiff enough. The hollow inner core of the transmitting sections were filled with C35 grade concrete (Fig. 3.2). Compressive strength of the filling was 35.8 MPa, and the modulus of elasticity was 31500 MPa.

When site conditions are examined, the loading condition of pressurized tunnels can be named as hydrostatic, at any point on a cross-section, the pressure experienced by the lining is almost constant and always perpendicular to the surface. Magnitude of this pressure only depends on the height difference between corresponding location and reservoir. In other words, strain conditions of lining does not influence the

Figure 3.2: Concrete filling process and roller supports of pressure transmitting sections

magnitude or distribution of acting pressure. Also, no directionality is present on this pressure, it always acts perpendicular to the surface. However, the loading system used in laboratory models can not perfectly simulate this phenomenon. The pressure is evenly distributed while the deformations are small. On the other hand, numerical simulations revealed that the damage distribution affects the pressure on lining when deformations get larger. Additionally, since water is absent in the laboratory model, penetration of the pressurized water into the cracks can not be modeled during the tests and may have substantial effect on the behavior of the tunnel. Thus, it can be said that the performance of loading system is decreasing as crack widths are getting larger.

3.3 Tunnel Lining

Horse-shoe shaped tunnel sections are quite popular in Turkey, owing to the advantages at construction stage. However, it is reported that the geometrical nonlinearity of this shape may create stress concentrations at the bottom corners (Tuncay et al. 2016). Horse-shoe shape is symmetric with respect to the vertical axis, and is often mentioned using three segments, the top part is called as the crown, lower arches are referred as bench walls or shoulders, and there is the straight bottom part, named as invert. For the laboratory model, dimensions of reference tunnel were directly scaled down. Crown part was a semicircle with a 720 mm inner radius, bench walls were centered and starting from crown's opposite ends, connecting to the invert of tunnel. Thickness of the tunnel lining was 160 mm (Fig. 3.3-a). Geometrical properties that are introduced here were kept constant through all eight specimens. Rein-

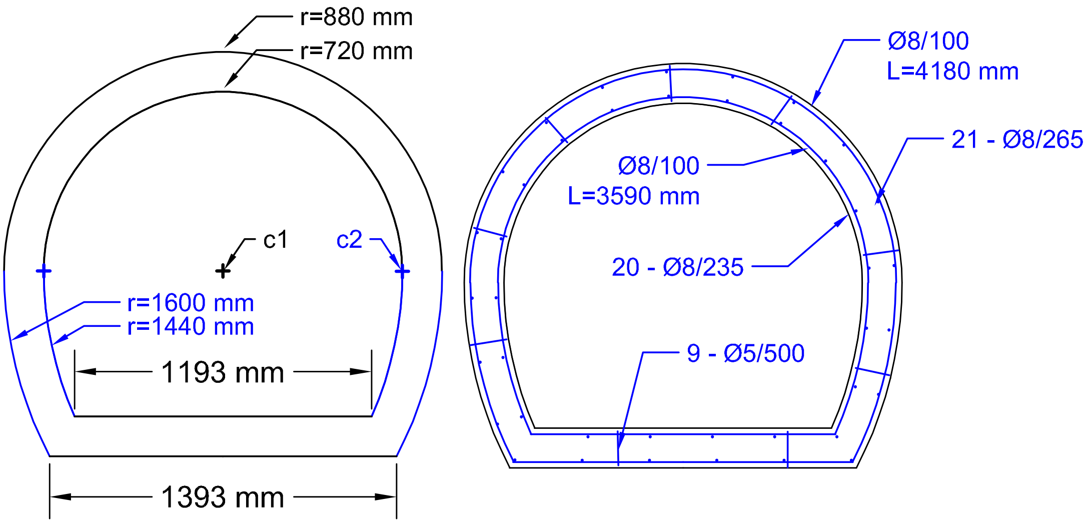

Figure 3.3: Formwork and reinforcement details of lining

forcement of a pressurized tunnel are longitudinal bars, rib reinforcements (one inner and one outer), corner reinforcement bars, and stirrups. For the laboratory model, reinforcement configuration was kept the same as the reference tunnel and rebar diameters were calculated by keeping the steel to concrete ratio constant (equation 3.3). Accordingly, the rib reinforcements and longitudinal bars were selected as $\phi 8$ and stirrups as $\phi 5$ (Fig. 3.3).

$$\rho_{tunnel} = \frac{A_{steel}}{A_{concrete}} = \frac{\pi \times 7^2 \times 1000/300}{1000 \times 400} = 0.00128817 \tag{3.1}$$

$$\rho_{lab} = \frac{A_{steel}}{A_{concrete}} = \frac{\pi \times 4^2 \times 400/250}{400 \times 160} = 0.00128817 \tag{3.2}$$

Two sets of rib reinforcement were placed to the inside and outside with 50 mm concrete cover. Longitudinal bars were placed between inner and outer ribs, providing a concrete cover of 50 mm. Although longitudinal bars did not play a crucial role for this experiment, they were implemented to laboratory model. Standard construction steel was used for all reinforcement bars, which are classified as S420, and should have a yield strength of 420 MPa and an ultimate strength of 500 MPa according to TS708. Rebars have been tested according to the Turkish standard of reinforcement bars (TS708) and Turkish Standard for metallic materials-tensile testing (TS 138 EN

Table 3.2: Tensile strength results of reinforcement bar samples

Sample	Yield Strength (MPa)	Ultimate Strength (MPa)
1	386.8	555.0
2	384.8	550.9
3	358.5	522.5
Mean	376.7	542.8
Target	420 MPa	500 MPa

10002-1). Three 400 mm long coupons were taken from the same batch, and then their nominal diameter were calculated with equation 3.3. This calculation was made to correct the ribbed dimensions. G represents the weight of sample, ℓ is the precise sample length. Then each sample was subjected to tensile strength test. Yield and ultimate stresses are given in Table 3.2.

$$d_s = 12.74\sqrt{\frac{G}{\ell}} = 12.74\sqrt{\frac{160}{42.13}} = 7.929 \tag{3.3}$$

Since the steel to concrete ratio was kept constant through all experiments, the same detailing was used (Fig. 3.3-b). They were shaped and placed in the same manner in all eight specimens. Concrete properties were varied on purpose: four boundary conditions (NC, LC, HCP, HCI) were first tested with conventional reinforced concrete. Two of them were repeated with fiber reinforced concrete (NCF, HCIF) later. One repairing technique was tested on imperfect contact condition (after HCI experiment: HCIR). Lastly, a partially faulty contact condition was assessed using only fiber reinforced concrete (HCH).

It must be noted that mechanical properties of concrete varied through the tests. For example, preparation phase of HCP experiment took longer than anticipated due to complex assembly of prestressing mechanism. In order to get experimental schedule back on track, the experiment was to be done earlier than 28 days. Therefore, some changes had been made from the original concrete recipe in order to get 25 MPa earlier than 28 days (Table 3.3). As testing had to be delayed due to laboratory conditions, the experiment was not conducted before 28^{th} day, resulting in an increased

Table 3.3: Concrete mix designs used on linings

Components	NC	LC	HCP*	NCF	HCIF**
CEM II	420	420	0	0	0
CEM IV	0	0	420	300	300
Water	220	220	220	165	165
Aggregate (0-3 mm)	775	775	775	1253	1253
Aggregate (3-12 mm)	900	900	900	692	692
Fiber	0	0	0	14	14
ACE450	0.75	0.75	0.75	1	1
Sum	2316	2316	2316	2425	2425
Target f_c	25	25	40	35	35

* On HCI and HCIR experiments, the lining casted for HCP was used

** On HCH and HCIF experiments, the same lining is used

compressive strength of lining (at HCP). Same lining specimen was used in HCI and HCIR experiments too, since lining response was within elastic limits at the HCP experiment and the focus of HCIR experiment was on the behavior of damaged linings after being repaired.

Three of total eight experiments were conducted with on fiber reinforced concrete linings. Fibers help preserving the structural integrity of concrete element. When a microcrack is developing, tensile stresses become localized on crack tip, forcing the defect to propagate. But, with the presence of close to uniform fiber distribution, some fibers are activated by the opening of microcrack, bridging the stress from one side of the crack surface to the other, thus relatively relaxing the stress concentration on crack tip. Prevention of crack propagation provides more frequent and thinner cracks along lining, meaning more energy absorption. Therefore, presence of fibers in concrete improves the behavior of the structural system. It is known that addition of fiber decreases the workability and flowability of concrete. In order to compensate the adverse effects of fibers, a 300-dosage new mix design with finer aggregate profile was adopted. 1.3 percent by volume of fiber addition was within the limits of manufacturer (forta-ferro).

All concrete elements of tests were cast in the laboratory. Tunnel lining was approximately 0.22 m^3 corresponding to 530 kg which exceeds the capacity of the concrete mixer of the laboratory. That is why lining concrete was prepared in 2 batches of approximately 270 kg. Nine cylinder samples ($150mm \times 300mm$) were taken from every concrete mix; three for compressive strength tests (ASTM C39), three for split tensile tests (ASTM C496), and three for determining modulus of elasticity (ASTM C469). Also, for third point bending tests (ASTM C78), three rectangular prism samples (75 mm x 75 mm x 325 mm) were taken. First samples of each test was taken from first batch in the mixer, other two was taken from the second batch. Samples were kept close to experimental model with the same curing condition. Curing was achieved with wet burlap. Mechanical properties of lining (Table 3.4) are more or less as expected and comparable. Even though grade of lining concrete were different in experiments NC-LC, HCP-HCI-HCIR and NCF-HCIF; these three groups are comparable within themselves and relatable with each other.

3.4 Rock Substitute

This section introduces the surrounding layers of pressurized tunnels, and the material that represents it on the laboratory model. Overlying strata solely provide support boundary conditions of tunnel lining. More importantly, when tunnel lining is in perfect contact condition with intact rock with high stiffness, 30-100% of the load is carried by rock mass. Therefore, their mechanical properties are of the utmost importance. Improving the conditions of rock may be crucial for the proper support mechanism of linings. Some enhancement methods have been presented by Lunardi (2008), Singh (2006), and Palmstrom (2009). Reported experience show that extensive geological surveys and designs made in accordance with current terms of rock is beneficial, but corrections due to unforeseen events on construction stage are unavoidable.

The reference tunnel of this study was surrounded by weak rock. More importantly, broken contact zones between lining-rock interfaces were observed during core

Table 3.4: Mechanical properties of lining sections

Material Parameters	Sample number	NC	LC	HCP	NCF	HCIF**
Compressive Strength (MPa)	1	27.67	23.01	38.84	27.85	37.39
	2	24.73	28.70	42.15	32.50	36.95
	3	21.79	23.14	37.31	-	37.43
	Mean	**24.73**	**24.95**	**39.43**	**29.68**	**37.26**
Split Tensile Strength (MPa)	1	-	2.19	3.20	2.27	2.40
	2	-	1.97	2.89	3.07	2.34
	3	-	1.41	-	-	2.60
	Mean	**-**	**1.86**	**3.05**	**2.67**	**2.45**
Flexural Strength (MPa)	1	3.38	3.73	5.05	-	6.31
	2	3.72	3.72	4.83	-	6.07
	3	1.30	-	-	-	6.84
	Mean	**2.80**	**3.73**	**4.94**	**-**	**6.41**
Modulus of Elasticity (GPa)	1	24.63	24.83	34.36	32.12	31.96
	2	24.61	24.88	34.43	41.55	31.97
	3	24.04	21.56	33.26	-	31.64
	4	24.03	21.81	33.18	-	31.71
	Mean	**24.33**	**23.27**	**33.81**	**36.84**	**31.82**
Target f_c		25	25	40	35	35

* On HCI and HCIR experiments, the lining cast for HCP was used

** On HCH and HCIF experiments, the same lining is used drilling investigations. GSI value of the rock (fractured andesite) was identified between 20-40, which expresses low surface quality and disintegrated rock structure. For a more objective reference, elastic modulus and compressive strength of rock were taken as 8 GPa and 4 MPa, respectively. These were the key properties that define the general behavior of overlying stratum, together with the overburden pressure.

Using a bulk rock mass on laboratory model was inconvenient due to logistic problems. Even the scaled down dimensions of tunnel were too large. Transportation of fractured rock body without disturbing it was not feasible. That is why the overlying stratum had to be simulated with another material. Development of a substitute for rock layer was necessary. Several important qualities were expected from the material, first, it had to mimic the on-site behavior, low elasticity modulus and compressive strength, brittleness. Also, the material had to be produced in the laboratory environment. For this purpose, concrete with a weak filler material was thought to be fit. Two approaches were taken into account: first one is to replace aggregate with different materials in order to get a uniform material (Appendix A), other was to use a layered structure, since the laboratory setup was already considered in two dimensional setting.

The laboratory model with 200 mm height was considered to deform in plane stress. Thus, a composite structure might be implemented as rock substitute layer in the laboratory model. In other words, a filler material with very low modulus of elasticity covered by low grade concrete on the top and bottom would be acceptable as the rock substitute. As long as symmetry of three layers with respect to the mid height of the specimen and reaction in elastic range were assured, combined response of three layers would successfully represent the rock mass. When the elastic modulus of concrete with 10 MPa compressive strength is examined, autoclaved aerated concrete (AAC) blocks were seen fit in order to get the total elastic modulus as low as 8 GPa.

Two failure types were anticipated for the three layered rock substitute, in plane and out of plane. Expected final behavior of rock substitute models were radial failure planes, whereas tangential failures, which are pretty unlikely to occur, would indicate problems exist related with preparation phase. Out of plane failures modes on the other hand, signal that the plane stress assumption is violated and results of experi-

Table 3.5: Mix recipe for rock substitute concrete

Components	Top and bottom layers of rock substitute (kg/m^3)
Cement CEM II/B-M (P-L 32.5R)	240
Water	240
Aggregate (0-3 mm)	760
Aggregate (3-12 mm)	1075
Sum	2315
Target Young's Modulus (GPa)	**15**
Target f_c (MPa)	10

ments are compromised. De-lamination of layers and failure of a single layer were possible out of plane failure modes that were considered. Reasons of such failure may be due to the presence of gaps between layers, imperfect shear flow and different boundary conditions of concrete covers. Perfect contact between AAC and cover concrete layers was provided by using a flowable concrete recipe (Table 3.5), since only 10 MPa compressive strength was planned of cover layers. So, AAC blocks were placed while the bottom concrete layer was being casted. Shear connectivity between layers was ensured by shear keys. 8 and 6 cm long screws were applied to bottom and top face of AAC blocks, which not only acted as shear keys but also helped to the placement operations and kept the intended orientations of AAC blocks until the concrete cover has set. Last potential cause of single-layer-failure was the different boundary condition of two cover concrete layers. Outer boundary of top cover was exposed to air, whereas the bottom cover was laying on top of leveled plywood plates. While deforming, the bottom cover was prone to act stiffer than top layers, due to friction, and this is why two layers of nylon sheets with oil were put on the interface between outer boundary of cover concrete and plywood.

Aim of the rock substitute was to obtain an average elastic modulus as 8 GPa. The height of the laboratory model and AAC blocks were 200 mm and 100 mm respectively. Elastic modulus of commercially available AAC blocks were reported and tested to be 2.10 GPa. In order to achieve the target, two symmetrical 50 mm-thick

Figure 3.4: Construction stages of three layered rock substitute

low grade concrete covers with 13-15 GPa elastic modulus were required (Table 3.6).

At the construction stage of rock sandwich, first the AAC blocks were placed and if needed cut to fill the formwork. After they were removed from the formwork, screws were applied to the bottom faces of AAC blocks. Then the formwork was prepared for the casting of bottom cover concrete with grease, nylon sheets and silicon. While one team was pouring the bottom cover concrete, another was carefully placing AAC blocks and ensuring no gap was allowed between AAC blocks and concrete. Concrete cubes were placed on the top of the AAC blocks as weights to prevent floating of AAc blocks. After bottom concrete set, these weights were removed, and screws were evenly applied to the top face of AAC blocks. Afterwards, top cover concrete was cast (Fig. 3.4).

Table 3.6: Mechanical Properties of rock substitute layers

Material Parameters	Sample number	LC-Bottom	LC-Top	AAC	HCP*-Bottom	HCP*-Top
Compressive Strength (MPa)	1	8.47	8.53	-	8.06	7.46
	2	6.13	7.28	-	8.19	7.91
	3	5.32	6.72	-	-	-
	Mean	**6.64**	**7.51**	**4.9****	**8.13**	**7.68**
Split Tensile Strength (MPa)	1	0.76	0.62	-	0.83	0.71
	2	0.81	0.56	-	0.86	0.75
	3	0.66	-	-	0.84	0.73
	Mean	**0.74**	**0.59**	**0****	**0.84**	**0.73**
Modulus of Elasticity (GPa)	1	-	-	-	12.64	14.72
	2	-	-	-	12.69	14.73
	3	-	-	-	13.61	16.38
	4	-	-	-	13.59	16.34
	Mean	**-**	**-**	**2.10****	**13.13**	**15.54**
Target f_c		25	25	40	35	35

* On HCI,HCIR, HCIF and HCH experiments, same rock substitute specimen was used

** Manufacturers values are used

3.5 Confinement due to In-Situ Stress

Pressurized tunnels are mainly located underground, below several layers of rock strata. Critical rock thickness around tunnel lining is affected by layers of rock above itself. Rock body is under natural compressive stresses. This effect was simulated by a prestressing mechanism in the laboratory models with high confinement (HCP, HCI, HCIR, HCIF and HCH).

Prestressing mechanism was designed to represent a maximum overburden pressure caused by 60 to 100 meters of rock, depending on rock density. Moreover, the horizontal to vertical pressure ratio (k_0) was adjustable, since mechanism was consisting of two independent components in principal directions. In this study, k_0 was kept as 1 during all tests. Working principle of the prestressing mechanism in one direction is as follows: rigid steel sections at opposite sides were pulled to each other using prestress steel tendons, which caused compression on the outer rock substitute (Fig. 3.5).

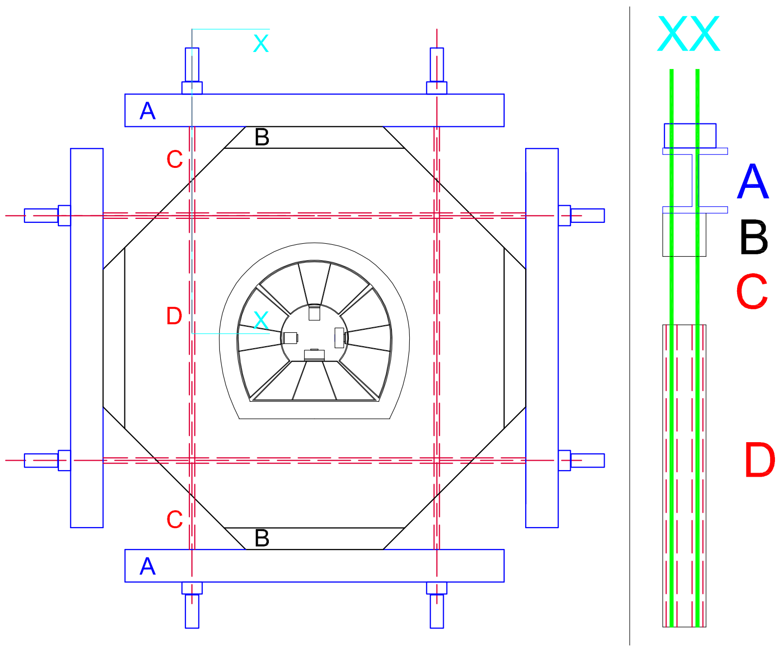

Figure 3.5: Plan and section of prestressing mechanism parts: A) Steel beam, B) Buffer RC beam, C) Exposed tendon, D) Embedded Tendon

High rigidity of the steel sections was essential for the proper distribution of stress through the rock substitute. Tendons that link opposite steel beams had to be placed 0.5 m away from the corner of rock substitute (Fig. 3.5). Possible loss of contact of the middle of steel section to concrete due to bending had to be prevented. Therefore, HEA360 steel section was chosen as supporting beams.

Beams were dimensioned properly for the experimental setup and holes were drilled on both top and bottom flanges of the sections in order to provide a path for tendons. Entrance zones and configurations of tendons can be seen from Fig. 3.6, at the inner faces of unmarked beams. For safety measures, steel beams were reinforced near drilling locations. At vertical axis, centers of holes were 12 cm apart from each other, near to the ends of flanges, therefore reinforcements were applied to prevent flange buckling by usig $100mm \times 60mm$ U sections (A in Fig. 3.6). At the perpendicular axis, on the other hand, holes were closer to each other (40 mm between centers) so the web had to be cut out. Therefore the reinforcements in horizontal directions were to applied to provide shear flow and to enhance web area (C in Fig. 3.6).

Another safety measure for the pressure mechanism was the gap between lining and rock substitute. Lining concrete was already cast before the prestressing mechanism was activated. But to properly apply overburden pressure on the rock substitute, lining needed to be separate with rock substitute. This is why a 10 mm gap on their interface was left at the preparation phase of HCP laboratory model, using styrofoam. This space was preventing any additional stress on the lining during post-tensioning the tendons. After the compressive loading of rock substitute, the gap was filled with high strength grout.

Even though a relatively rigid section was chosen as steel beams, rest of the stress flow had to be checked. Numerical studies showed that at the interface of rock substitute and steel beams, corners of concrete layers were prone to crushing. In order to prevent this, $200mm \times 200mm$ buffer reinforced concrete beams were implemented to the laboratory model prior to rock substitute application. For this purpose, minimum rebar requirements were calculated in accordance with TS500, and C30 grade concrete was cast (Fig. 3.7).

Tendons that link opposing steel beams were crossing the rock substitute in both

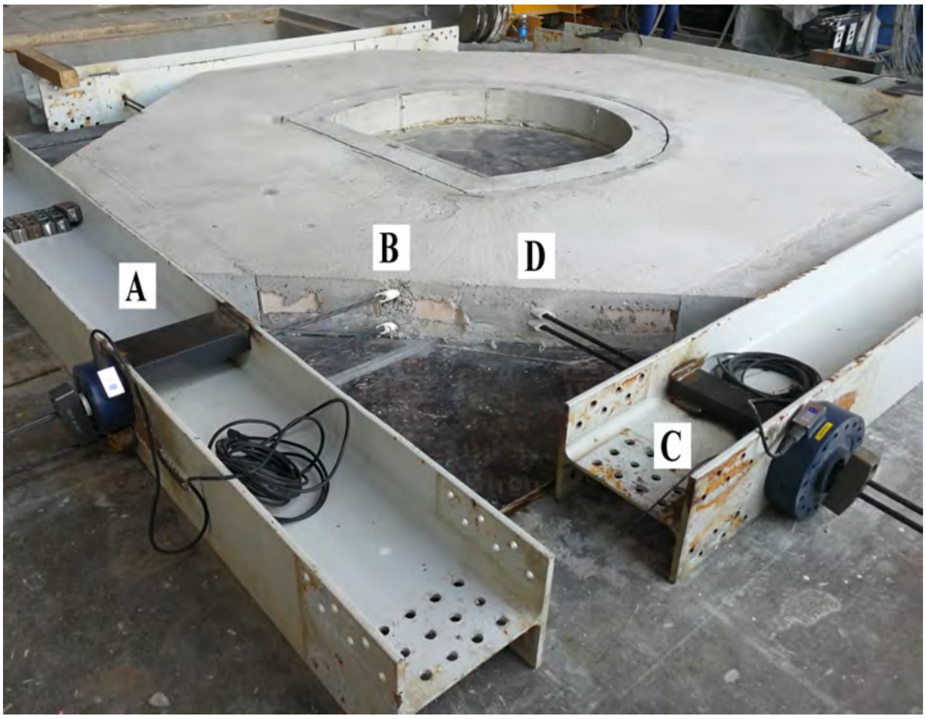

Figure 3.6: Steel beams before prestressing application on laboratory model HCP: A) Typical beam reinforcement on vertical system, B) Entrance area of vertical tendons to rock substitute, C) Typical beam reinforcement on horizontal system, D) Entrance area of horizontal tendons to rock substitute

Figure 3.7: Photograph of laboratory model after casting of Buffer RC Beam and before application of rock substitute

horizontal and vertical axes. In order to prevent intersection or out-of-plane forces and moments, they were located at different levels. In both directions, there were two axes and two cables in one direction. Tendons in the same direction were placed symmetrical with respect to mid-height of the laboratory model, to comply with two dimensional assumptions. In horizontal axis, centers of tendons were spaced 40 mm apart and in the vertical axis, the spacing was 120 mm (Fig. 3.6). Each tendon was planned to carry approximately 130 kN. With their nominal diameter of 15.2 mm the stress per tendon was 717 MPa and their ultimate capacity was supposed to be 1860 MPa. To ensure this safety factor (2.6), two coupons were prepared and were subjected to tensile strength test (Fig. 3.8). Test results showed that their ultimate strength were 275 kN corresponding to 1516 MPa. This unexpected result was not important since the applied force was far below the ultimate.

Confinement procedure was conducted 28 days after the concrete layers of rock substitute on HCP specimens were cast. In order to avoid bending of steel beams around concrete corners or create out of plane moments on laboratory model, tendons were planned to be loaded incrementally. Since, there were only two prestressing appara-

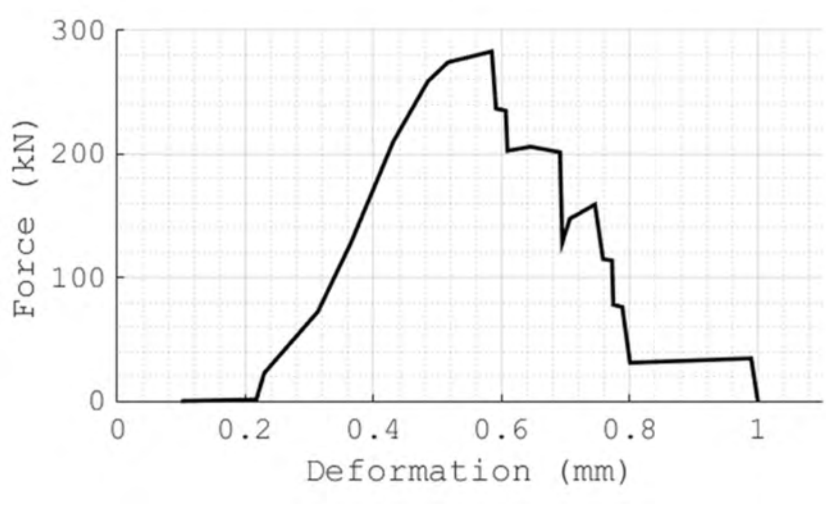

Figure 3.8: Result of tensile strength test and appearance of failed sample

tus available, the loading was starting from two bottom tendons of vertical direction, proceeding to top tendons at same axes, than the same procedure was applied to horizontal direction. Each load step was 30 kN, with 16 steps in total. During the first prestressing step, tensile stresses caused four cracks in top concrete cover. However, these tension cracks have closed with the application of stress on the orthogonal direction, at the third and fourth load steps. Rest of the confinement procedure passed uneventful, without any errors. All procedure was observed closely using strain gauges and LVDTs. Absolute and relative displacements of laboratory model, as well as tangential strains on lining and rock substitute were recorded (Fig. 3.9). Moreover, load cells were attached to horizontal and vertical tendons in order to control application of overburden pressure.

Loading sequence and intensity are presented on horizontal and vertical tendon force plots (Fig. 3.10 and 3.11). The pullbacks after every load step originate from the working manner of loading apparatus. First, the tendon to be prestressed was pulled with the hose-head, then the jack was hammered. While the jack slots into place, a slight force release occurred on tendon. Another noticeable point on these two plots is the measurement method on different axes. In the horizontal axis, the close distance between top and bottom tendons did not allow two different load cells to be used, therefore their sum was measured. Loading of top tendons can be differentiated using the hammering pullbacks on the middle part of horizontal plateaus (Fig. 3.10).

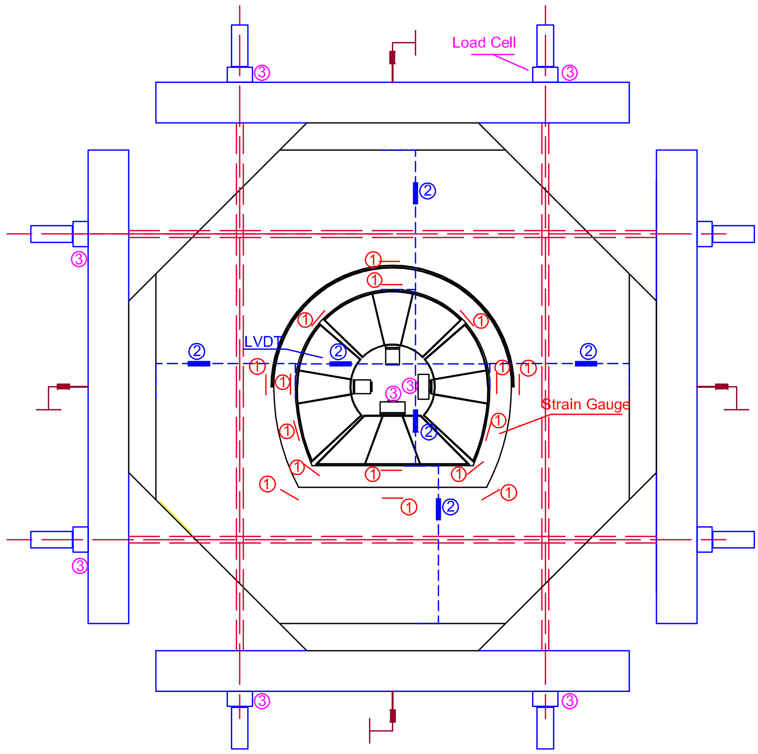

Figure 3.9: Instrumentation used on confinement procedure 1: Strain gauges, 2: LVDTs, 3: Load cells

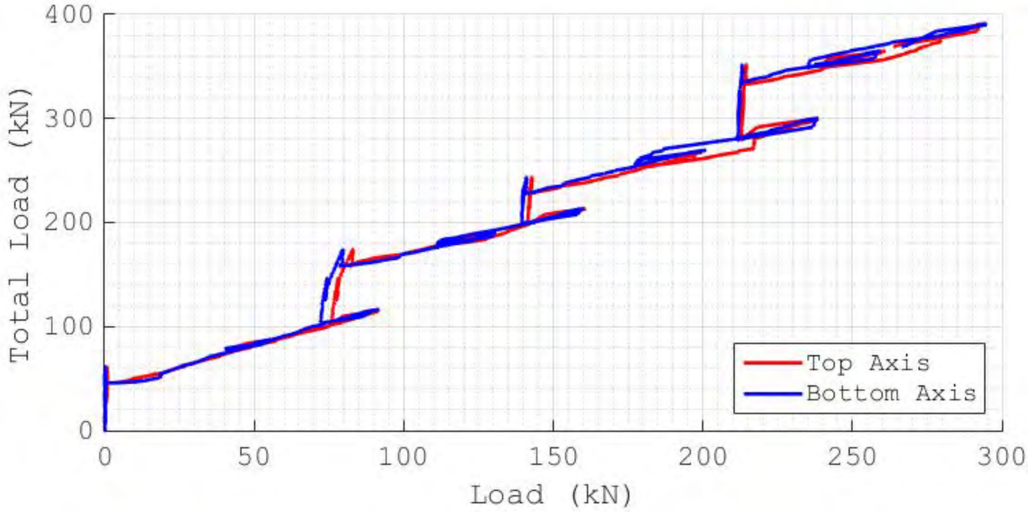

Figure 3.10: Resultant force vs. horizontal tendon forces

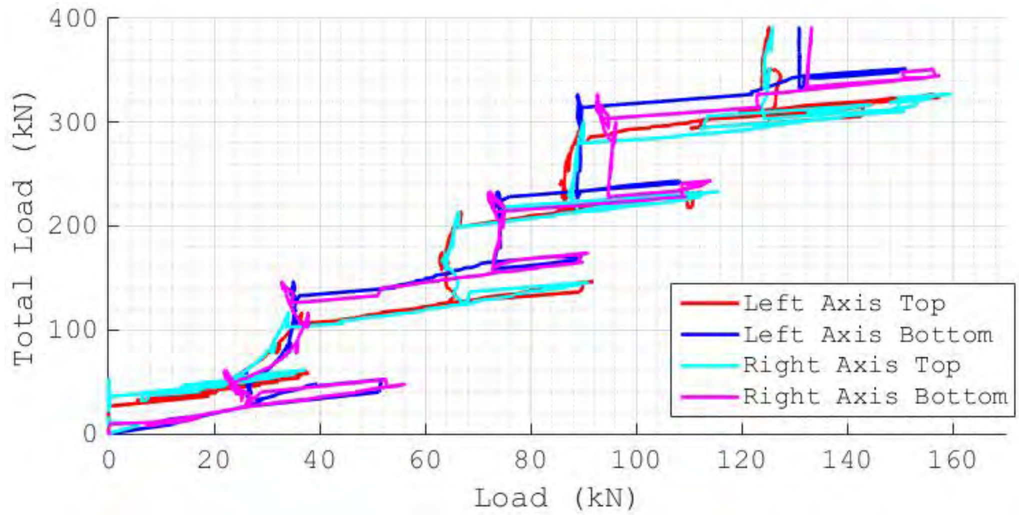

Figure 3.11: Resultant force vs. vertical tendon forces

During the prestressing procedure, the gap between lining and rock substitute was proven to be useful, as negligibly small strain recordings were taken from lining (Fig, 3.12). Although their magnitudes were small, and no contact was observed between rock substitute and lining, but the directionality of readings on lining were relatable to the loading sequence. This implies a small interaction still exists between rock substitute and lining, probably through plywood plates which they both lay upon. Readings on rock substitute, on the other hand, were rather large (Fig. 3.13). At the first two loading steps (vertical 40 kN), gauges on 3:00 and 9:00 o'clock recorded large compressive strains, with the counterbalancing third and fourth steps, strain state has been normalized, this flow was repeated three more times until the end of the procedure. On the orthogonal directions, 12:00 and 6:00 o'clock gauges did not record any meaningful strains, due to the location of initial tension crack. The strain gauges on corners, however, (4:30 and 7:30) were already positioned close to principal stress direction, therefore almost uniform increase was observed in these directions, compared to back-and-forth behavior of others.

Absolute movement of specimen was observed from four ends of two principle directions (Fig. 3.14). First, two loading steps were applied to the specimen vertically, which caused contraction in vertical direction and expansion in horizontal direction. Convergence of final values of orthogonal directions, on the other hand, had to be reported as coincidental. Top and left contractions were 6.5 mm, while measurements

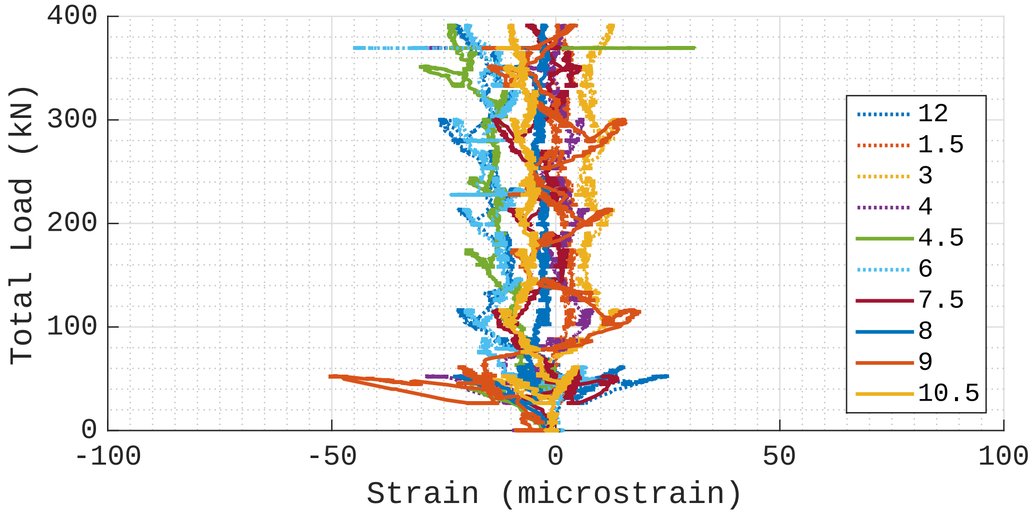

Figure 3.12: Strain gauge readings on lining

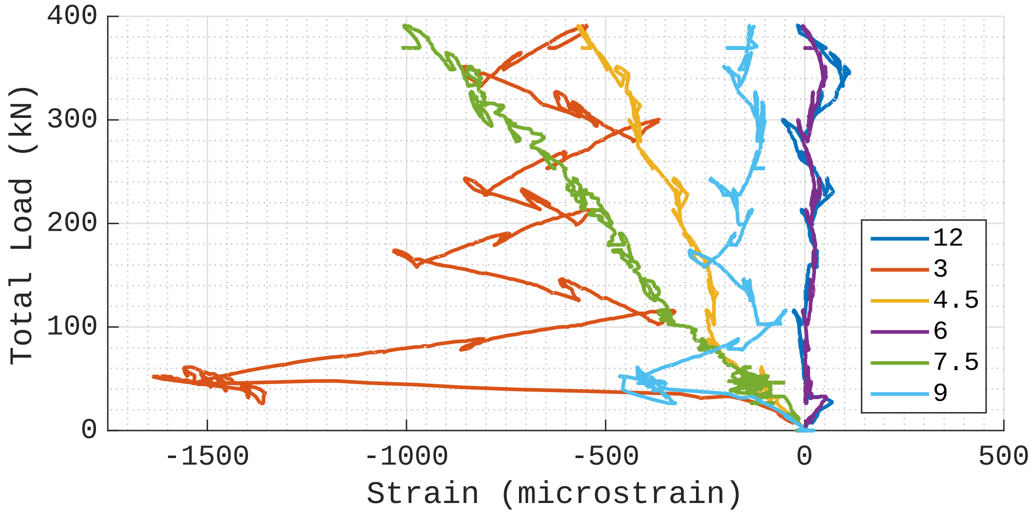

Figure 3.13: Strain gauge readings on rock substitute

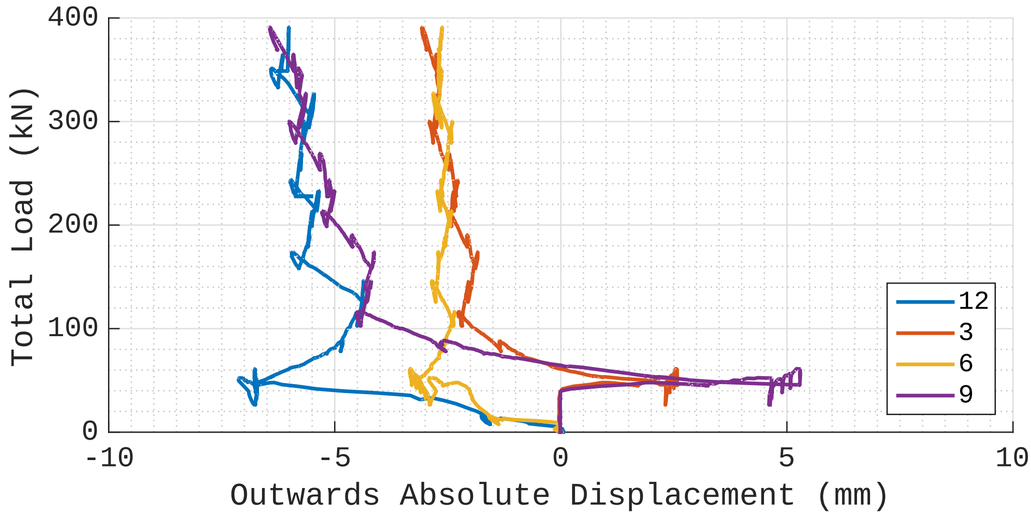

Figure 3.14: Absolute movement of laboratory model

on bottom and right ends were not more than 3 mm. Loading apparatus was applied from bottom and left steel beams, which does not account for the difference in opposite directions. Only possible cause of the phenomenon here is frictional forces varied from one side to another. Total contraction of rock substitute shows a more symmetric behavior on the vertical direction up to 100 kN total force (Fig. 3.14). LVDT that measures relative displacement on 9 o'clock direction had some problems related with connectivity issues, therefore jammed readings were erased (Fig. 3.15).

After rock pressure loading, the specimen was monitored to check the degree of relaxation of post-tensioning for 40 hours, until HCP experiment. Forces on tendons decreased just 2 kN in the first two hours (Fig. 3.16 and 3.17). Another sudden change was observed in the 14^{th} hour, which corresponds to the application of repair mortar. Overall force that was relaxed from the tendons at the end of control period was 1.7 kN, 2.9 kN, 2.2 kN, 2.6 kN from right bottom tendon, right top tendon, left bottom tendon and left top tendon at vertical axes, respectively. Same value was 3.7 and 5 kN for top and bottom axes in horizontal direction.

At the 14^{th} hour, the gap between lining and rock substitute was filled with repair mortar (Sika Monotop 612). This new connection between two layers changed the state of stress on them, especially after the mortar set at 18^{th} hour. Initially unstressed lining was observed to experienced tensile forces, caused by the shrinkage of repair

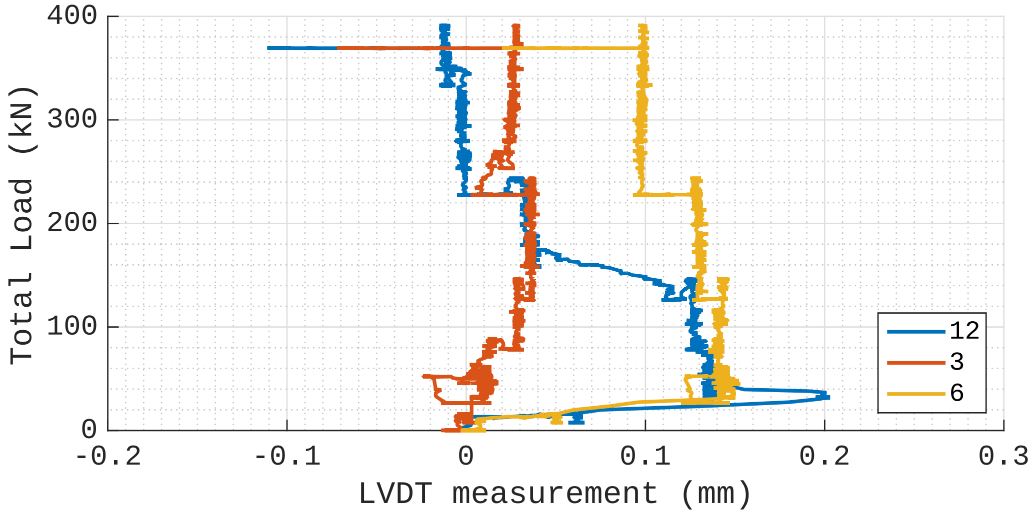

Figure 3.15: LVDT measurements on rock substitute

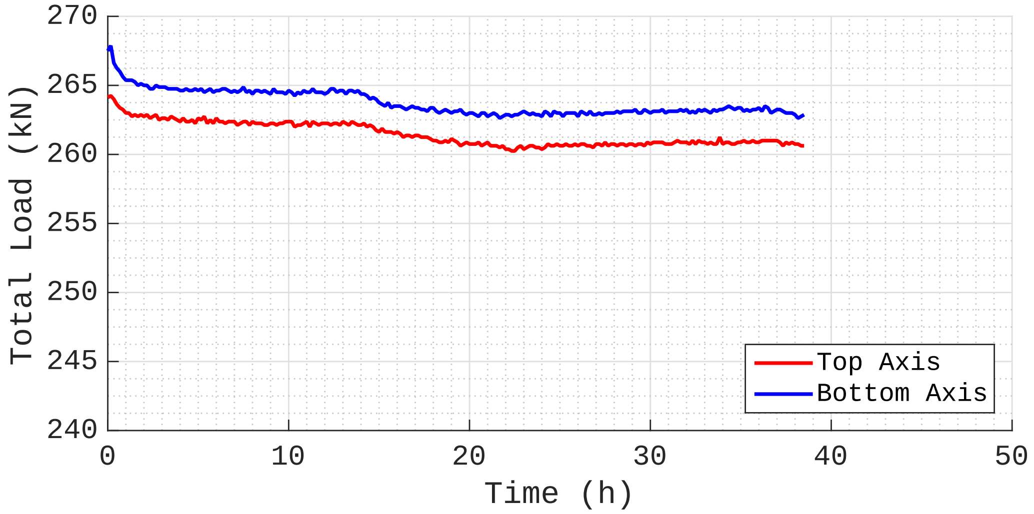

Figure 3.16: Relaxation of horizontal axes

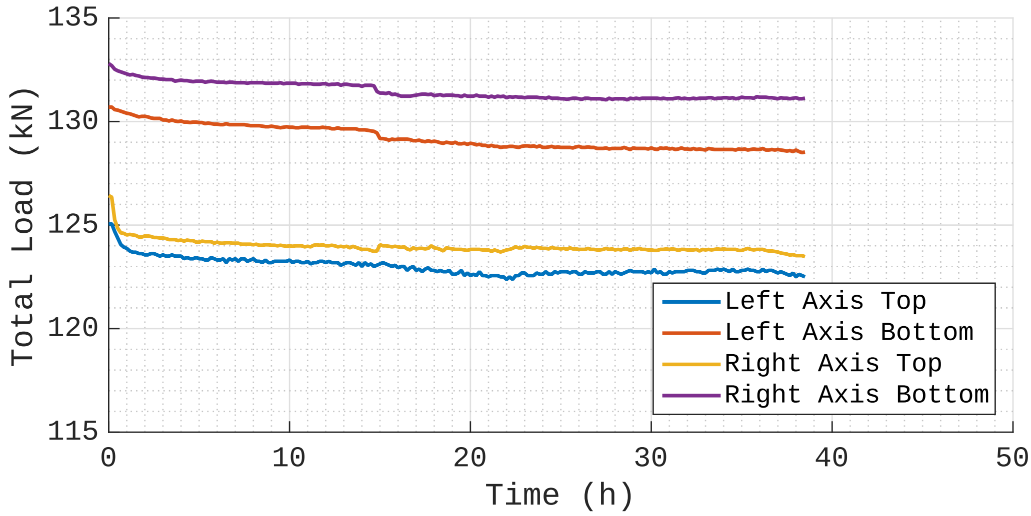

Figure 3.17: Relaxation of vertical tendons

mortar (Fig. 3.18). Rock substitute layer on the other hand, was located outside this gap. The shrinkage of repair mortar caused initial compressive readings, which have been recovered in 2 hours (Fig. 3.19). This may be caused by the partial splitting between repair mortar and rock substitute.

LVDT and strain gauge readings were not zeroed after the post-tensioning procedure, just like strain gauge readings. Slight changes were observed at the vertical direction corresponding to the setting of repair mortar (6 and 12 o'clock directions at Fig. 3.20). Relative LVDT readings also recorded the influence of filled gap on rock substitute (Fig. 3.21). 0.04 to 0.06 mm of contraction was observed along principle directions at 14^{th} hour, which was recovered after 4 hours. These readings support the separation of mortar and rock substitute layers.

At the experiments, LVDT and strain gauge readings represent the behavior of tunnel, but load cells were applied for controlling purposes. The experiments that prestressing mechanism was active (HCP, HCI, HCIR, HCIF, HCH), tension forces on tendons were checked using these load cells. Tensile forces on tendons were not checked between experiments, and although they were not zeroed, difference of a few kilonewtons were expected due to reseting of the data acquisition system. However, the fact that all changes being negative when they are chronologically ordered implies relaxation of the laboratory model was continuing.

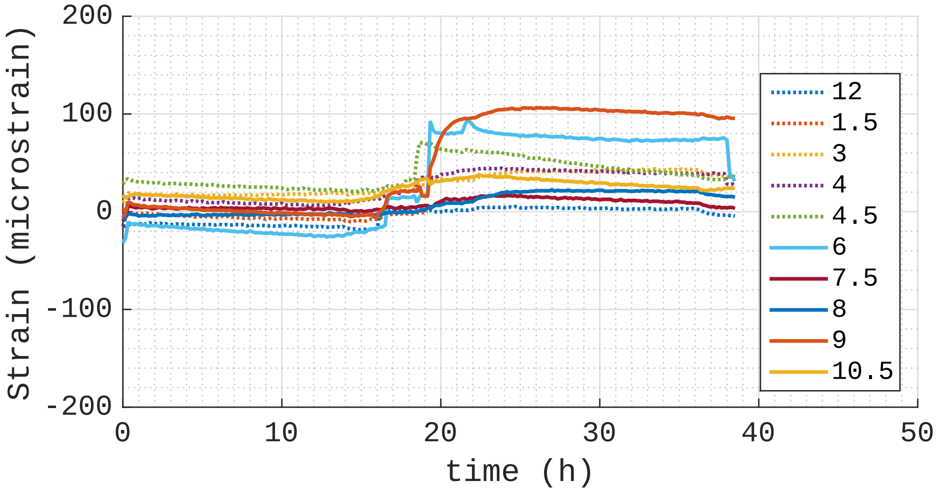

Figure 3.18: Strain development on lining

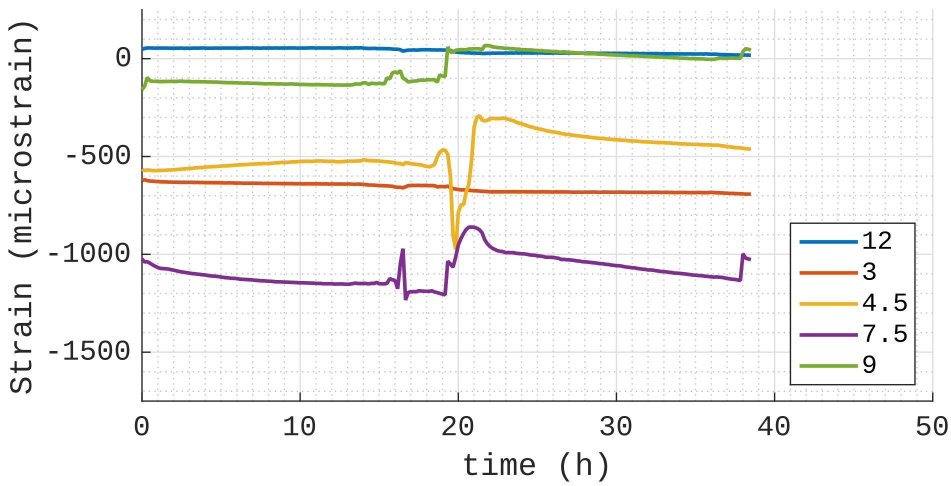

Figure 3.19: Strain relaxation on lining

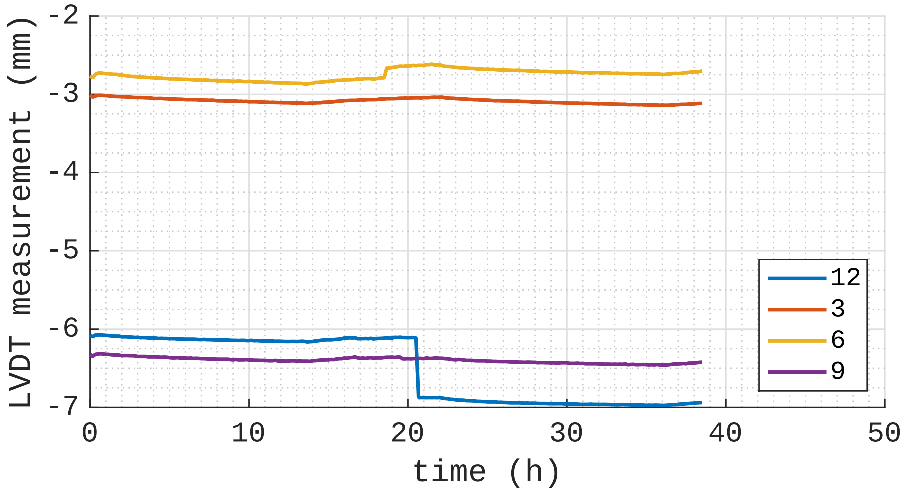

Figure 3.20: Absolute movement of laboratory model during control period

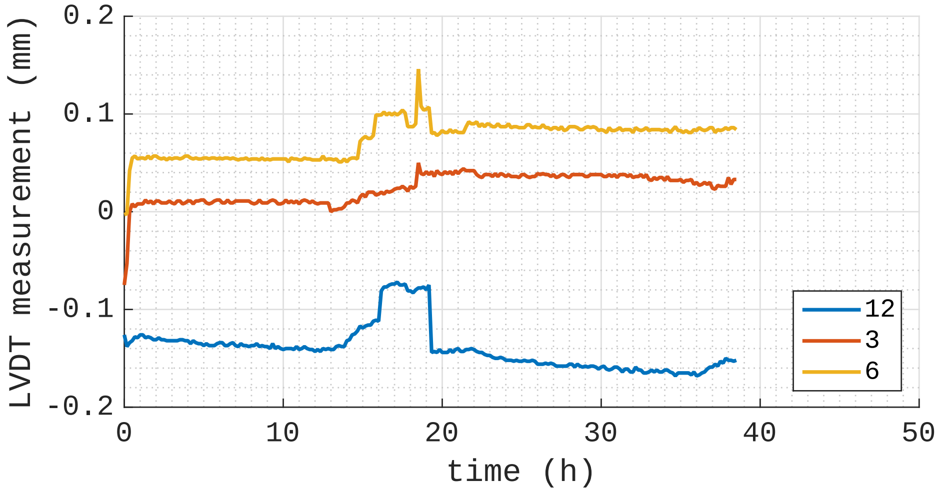

Figure 3.21: Relative displacement on rock substitute during control period

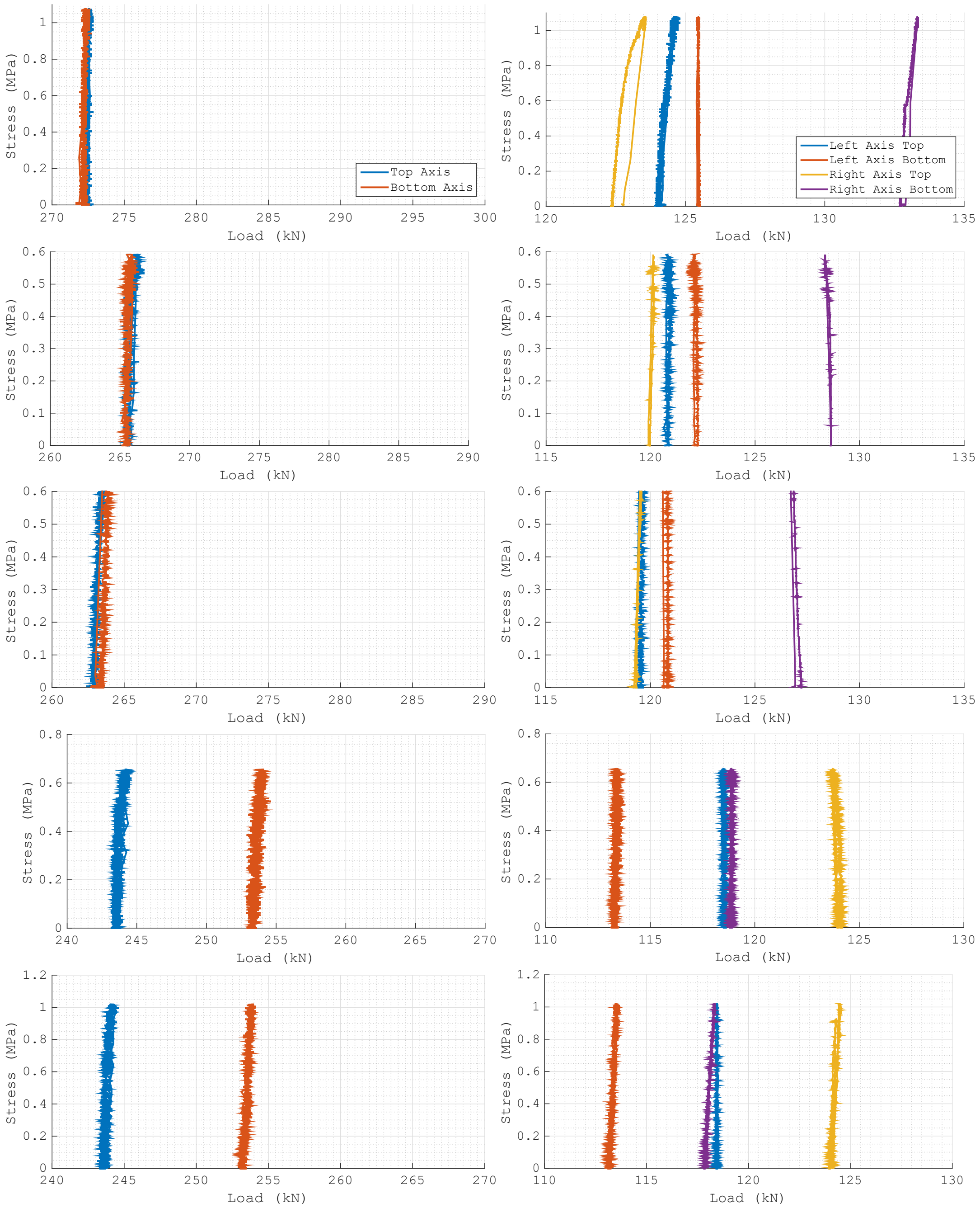

Figure 3.22: Fluctuations of tendon and axis forces during HCP, HCI, HCIR, HCIF, HCH experiments

3.6 Instrumentation

All data during experiments were recorded with a data acquisition system. Essential outcomes of experiments were stiffness of tunnel, stress condition of lining, crack initiation pressure, and crack distribution map. Therefore, LVDTs, strain gauges, load cells and several cameras were used to record crack propagation and strains on rock substitute and lining. Due to changing boundary conditions, different type of devices were used in the experiments, but their purpose were the same.

Behavior of tunnel under inner hydrostatic pressure were basically defined by the deformation of tunnel opening. Expansion of tunnel was examined in two main degrees of freedom, horizontal and vertical directions. Expansion in one direction was measured with two LVDTs of different strokes: 10 mm and 50 mm. Small stroke was essential for capturing initial stiffness. They have to be cut off when they reach their capacity, in order to prevent damage on the device. Second LVDT with larger stroke keeps the track after smaller LVDT stops recording. In each direction, two LVDTs with different precision and stroke capacities were mounted to steel rods that were anchored to lining concrete, and connected to rods that were on the opposite side of the lining with piano wires. At the specimens with rock substitute, same method of LVDT connection was used to measure relative deformation of the lining and rock substitute. In other words, rods were anchored to all boundaries of laboratory models in principal directions and deformation of each element was analyzed separately.

Absolute displacements of four ends in two principal directions were recorded. Different from other experiments, at NC and NCF experiments, absolute displacements of laboratory model were also corresponding to tunnel expansion due to absence of rock substitute. In these experiments, absolute displacements were measured at eight 45 degree divided regions.

Strain states of elements were monitored with two methods: with strain gauges and optical system. Strain gauges were applied to the critical regions in every experiment. Six critical regions were identified as center of crown, center of invert, two corners and 3 and 9 o'clock directions. Rock substitute and lining were observed in these areas with tangentially oriented strain gauges, at the top face of lining, four interim gauges were applied on the crown and bench walls (1:30, 4:00, 8:00, 10:30 o'clock directions). Although conventional strain gauges were sufficient to observe the behavior of tunnel, a secondary state of the art method of monitoring was implemented to the laboratory model: Optical system.

Optical measurement system used in the experiments had three main periods, the preparation phase to make differentiation between captured images possible, the recording phase during the experiment and processing after the experiment. At the preparation phase, specimens were first painted white and a speckle pattern was created on the white background with black spray paint. Cameras were applied above their interest areas rigidly. Orientation of the cameras had great impact on the accuracy of results, so all cameras were applied very carefully, one day before the tests. During all tests, cameras autonomously captured images every five seconds. The processing of sequential images were made with the computer program "GOM Correlate".

CHAPTER 4

RESULTS

4.1 Overview of Experiments

Presence of negligible overburden pressure could be observed on entrance zones of tunnels. First two experiments presented here, NC and NCF, were conducted to study one of two extreme boundary conditions: Absence of rock substitute around the tunnel lining. They also construct a characteristic behavior for the horseshoe-shaped reinforced concrete lining. Following them, LC experiment demonstrated the behavior of tunnel built in rock with the negligible overburden pressure.

If the contact between lining and rock is continuous, adequate overburden pressure increases the load capacity. HCP experiment constituted the second extreme boundary condition, where rock mass was subjected to sufficient overburden pressure and interface between rock and lining is ideal. The effect of partially and fully faulty interface was examined on HCH, HCI and HCIF specimens. On HCH specimen, a discontinuous interface was present above the crown. Other two specimens' crown, however, had no contact with the rock mass at all. Finally, performance of FRP-wrap repairing method for damaged tunnel linings was assessed during HCIR experiment.

Components of laboratory models and their preparation phases has been introduced in the previous chapter. Different circumstances and irregularities in experiments are mentioned at their descriptor paragraph in this chapter, where results of eight experiments has been presented in detail. It should be noted that the results are not in chronological order, but in a logical one.

The eight experiments cover different site conditions and possible material properties of lining material. They are named as follows:

- No Rock Lining **NC** `https://youtu.be/pCgY792XY3Q`
- No Rock Fiber Reinforced Lining **NCF**`https://youtu.be/hQKsRTRMaCA`
- Lining with Rock Body **LC** urlhttps://youtu.be/MMoLnc66fXs
- Lining with Stressed Rock Body (Perfect Contact) **HCP** `https://youtu.be/RCTvMfCrX0U`
- Lining with Stressed Rock Body (Imperfect Contact) **HCI** `https://youtu.be/qG-8T42BFcU`
- FRP-Repaired Lining with Stressed Rock Body (Imperfect Contact) **HCIR** `https://youtu.be/mXyiL3bQmsM`
- Fiber Reinforced Lining with Stressed Rock Body (Imperfect Contact) **HCIF** `https://youtu.be/eE-ENOeUiWk`
- Fiber Reinforced Lining with Stressed Rock Body (Improved Imperfect Contact) **HCH** `https://youtu.be/aLrLdwu-haM`

4.2 Tunnel Test without Confinement (NC)

In this test, an extreme boundary condition of the tunnel lining was investigated under flexure. The lining of the model was not confined by a rock substitute. This experiment forms a lower limit to the initial stiffness of the laboratory models. This case corresponds to a stable soft ground around lining or lack of any overlaying stratum. Manufacturing procedures introduced in Section 3.3 (Laboratory models: Tunnel lining) were followed in the preparation phase, since no rock substitute was needed for this experiment (Fig. 4.1).

Following the preparation phase, measurement devices were set up. Critical sections were decided to be monitored using 10 mm strain gauges. On the top face of the lining, ten tangential strain gauges were placed (1 and 2 in Fig.4.2), six of which

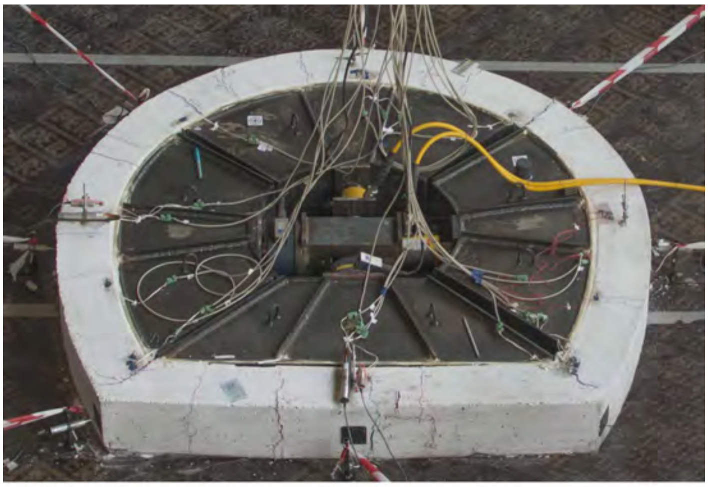

Figure 4.1: General view of laboratory model at NC experiment

were supplemented with two additional strain gauges so that they build up to 45-degree rosettes (1 in Fig.4.2). Also, making use of eight LVDTs, absolute movement of lining was measured from outside of the lining (3 in Fig. 4.2). Finally, two degrees of freedom that define the expansion of tunnel opening is monitored with two LVDTs in each direction, one with 10 mm capacity, and the other with 50 mm (4 in Fig.4.2).

The experiment was conducted on 10 June 2017 and it lasted approximately 70 minutes. Data was collected 2 times per second, each containing 36 different measurements. The pressure was incrementally applied to the setup with 21 kPa steps in order to clearly observe and note crack patterns (Fig. 4.3). Visible crack initiation started after 90 kPa inner pressure, and an evenly distributed crack map (Fig. 4.8) developed until 274 kPa. After initiation, the widening of cracks were closely tracked. First crack initiated on the right corner, second was on the second stress localization area, left corner. Following that, the straight bottom part experienced a crack pattern similar to a beam under bending. When the inner pressure reached 190 kPa, four other cracks occurred on the crown part. From 190 to 274 kPa, crack count was 16 at total, and the largest crack width was 0.6 mm on the invert and 0.4 mm at the crown. It should be noted that after 300 kPa, the center area of the bottom part of lining had taken a curved shape, thus lost contact with the loading system. Therefore, conclusions should be drawn considering bottom part was not under hydrostatic pressure after 300 kPa. At this point of experiment, crack widths were examined and noted as

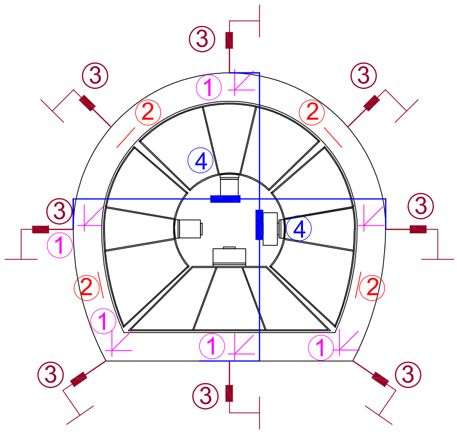

Figure 4.2: Instrumentation used at NC experiment 1: Strain rosettes 2: Tangential strain gauges 3: Absolute LVDTs, 4: Relative LVDTs

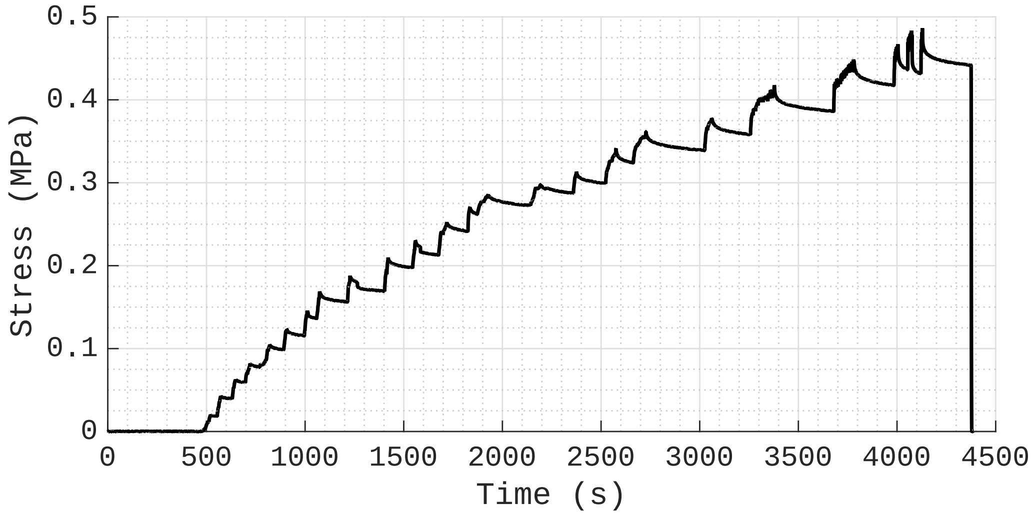

Figure 4.3: Load steps used at NC experiment

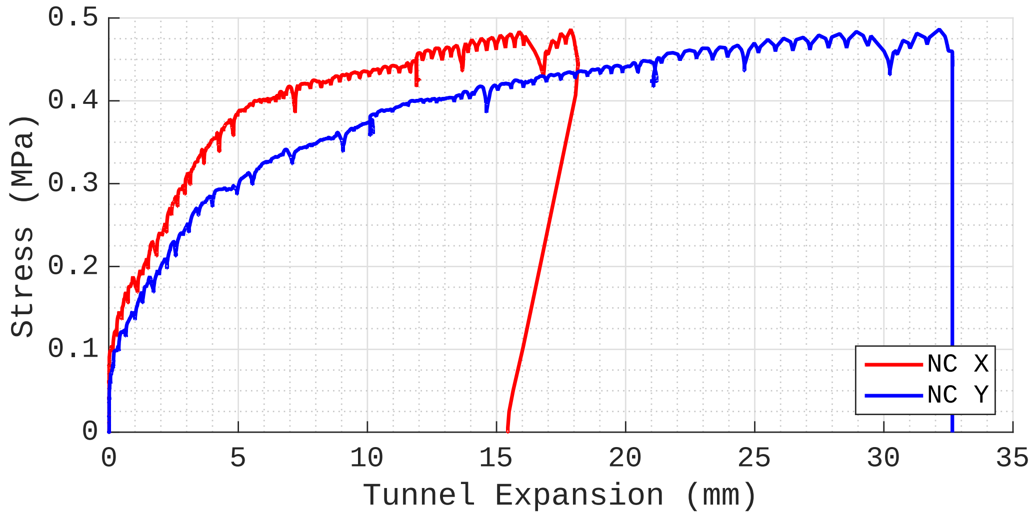

Figure 4.4: Expansion of tunnel opening at NC experiment

0.8 mm and 2.5 mm for the crown and invert, respectively. After observing mentioned behavior, largest openings were on different locations, 2.4 mm and 3.2 mm.

Most ductile behavior was captured in this most unfavorable boundary condition (Fig. 4.4). After 420 kPa, capacity reached and pressure level flattened, instead, large displacements took place. Large displacement indicated cracks that have initiated from the inner face of the lining reached to the outer face of section, damaging the integrity of concrete and leaving rebars open to air. Second important remark on large displacements is about functionality of loading system. As mentioned, the uniformity of pressure decreases abruptly when deformations become very large. Therefore, the experiment was concluded before the reinforcement bars reach to their capacity. Absolute LVDT readings were compatible with tunnel expansion. In the vertical direction, outwards displacement measured in the invert (denoted as 6 in Fig. 4.5) was rather larger than that of the crown (12 in Fig. 4.5). As expected, the behavior of straight bottom part is different than the crown and shoulders. On the other hand, outwards displacements on horizontal direction were very close to each other up to 400 kPa inner pressure. After that point, the symmetry of loading was lost, resulting with slightly larger displacement steps on the right-hand end (3 in Fig. 4.5).

Strain readings of tangential gauges are presented in Fig. 4.6. Even though most strain gauges represented significant instances of the experiment (1, 4.5, 6, 9), some

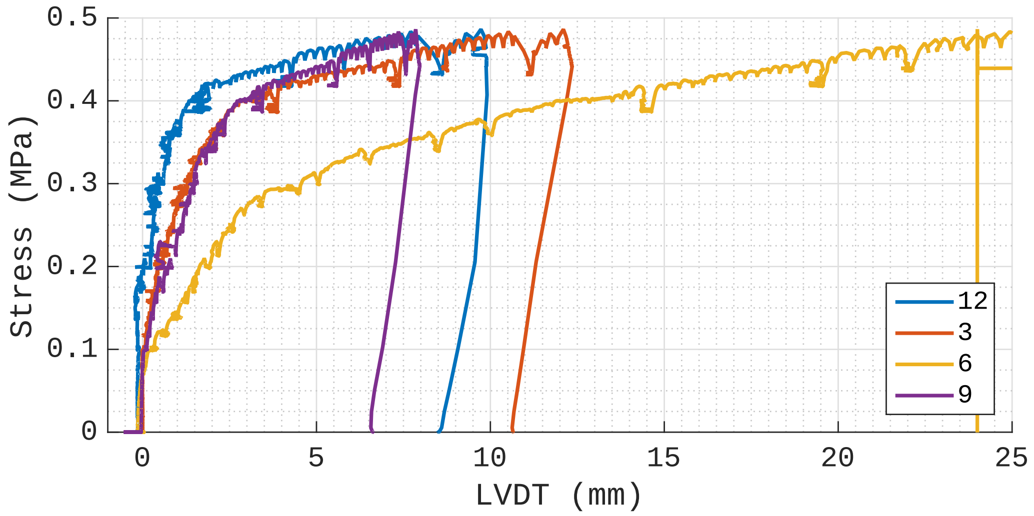

Figure 4.5: Absolute outwards displacements of specimen at NC experiment

readings were problematic or not reliable. This was caused by incompatible choice of strain gauge lengths. Three strain gauges (on directions 3, 7.5, 8) were unable to capture the cracks in their applied areas. Rest of them experienced some jumps due to maximum aggregate size. (Fig. 4.7).

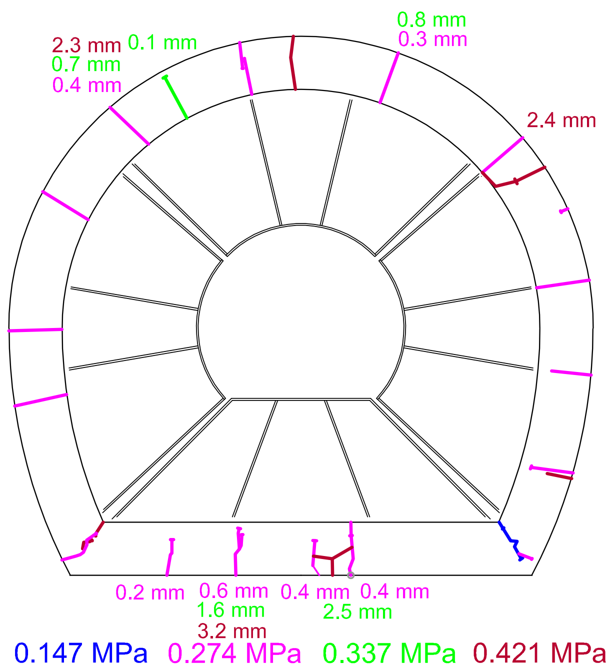

Figure 4.8: Crack map after NC experiment

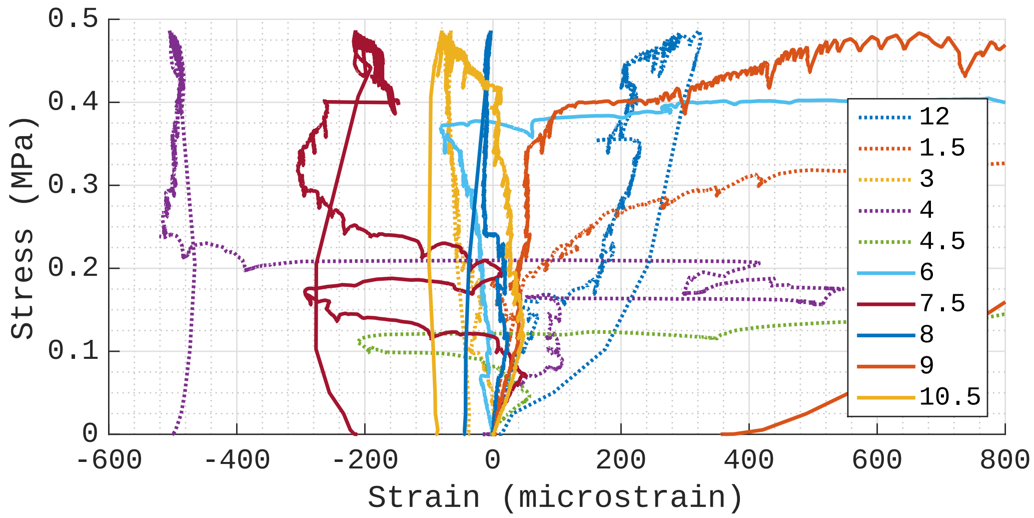

Figure 4.6: Strain readings on lining at NC experiment

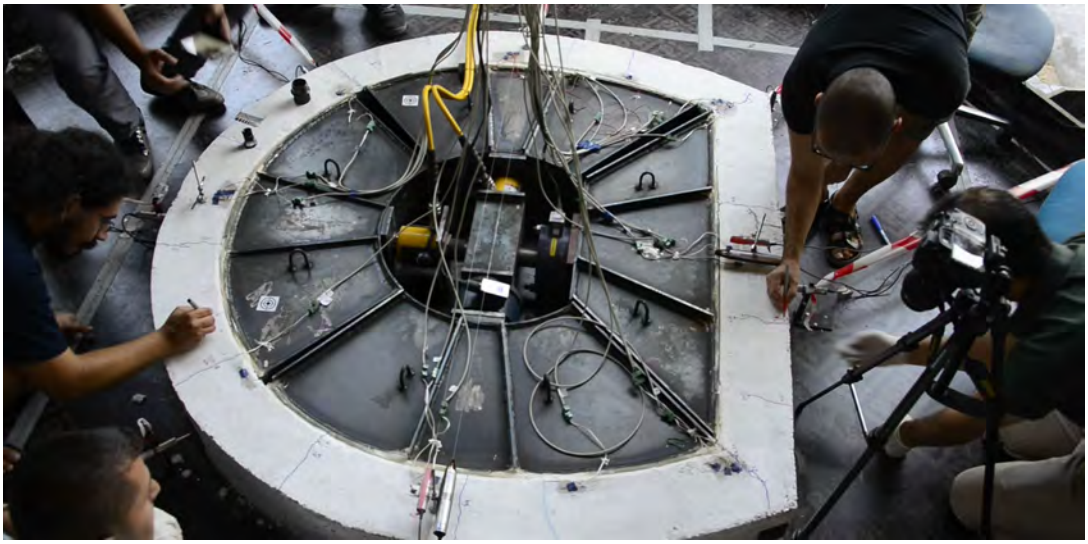

Figure 4.7: Photograph during the execution of NC experiment

Figure 4.9: Appearance of laboratory model at NCF experiment

4.3 Fiber Reinforced Tunnel Test without Confinement (NCF)

This section covers the second experiment on the most flexible boundary condition (NC, NCF). Key differences between the two were mix design recipe of concrete and instrumentation used to collect data. Synthetic fibers were used in the mix design of lining concrete in NCF experiment. There are several reasons to use fiber reinforced concrete for tunnel linings: protection against spalling, increased tensile strength and most importantly crack width control. The reason of using synthetic fibers was the fact that steel fibers being prone to corrosion once they are activated by a crack and lost their passivating covers. The other difference of mix design was the addition of superplasticizer, which was required because fibers reduce the workability of concrete abruptly. Rest of the preparation phase was identical to NC test (reinforcement bars, formwork, loading system). For the monitoring system, 60 mm strain gauges were applied to ten critical locations on the surface of lining (2 in Fig. 4.10). In this experiment, none of them were converted to strain rosettes. Similar to NC experiment, the absolute movement of experimental setup was monitored with 8 LVDTs. Expan-

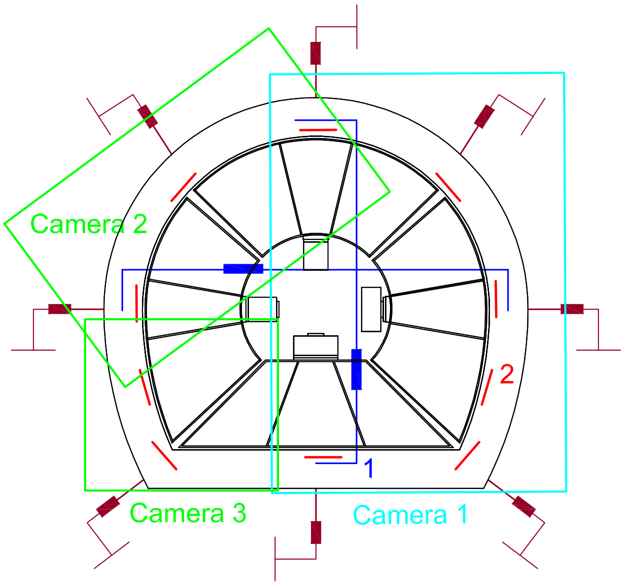

Figure 4.10: Instrumentation used at NCF experiment

sion of tunnel was monitored with two LVDTs in each direction (1 in Fig. 4.10). Additionally, an image capturing system was set up one meter above the laboratory model. Three cameras and two led spotlights were fixed to a steel frame (Fig. 4.9). In this system, one camera was designated to cover right half of the setup (from 12 o'clock to 6 o'clock direction). On the other side of the setup, 2 close-up cameras were recording the experiment (from 6 to 9 o'clock and 9 to 12 o'clock directions).

Experiment took place on 6 May 2017 and was completed within 20 minutes. Hydrostatic pressure was applied by 21 kPa load steps (Fig. 4.11). Vertical expansion of tunnel was again greater than horizontal, due to geometry of the laboratory model. A stiffer response was observed in the tunnel expansion compared to reinforced concrete experiment (Fig. 4.12). Cracks initiated after a pressure level of 120 kPa, at stress concentration areas (4:30 and 7:30 o'clock directions). Up to 280 kPa, no new visible cracks were present at crown or shoulders of the lining. This indicates that fibers were effective, preventing cracks to propagate. Starting from 360 kPa, tunnel expansion at every load step increased, indicating widening of cracks. Failure of the fiber reinforced lining section was caused by geometrical nonlinearity of the section.

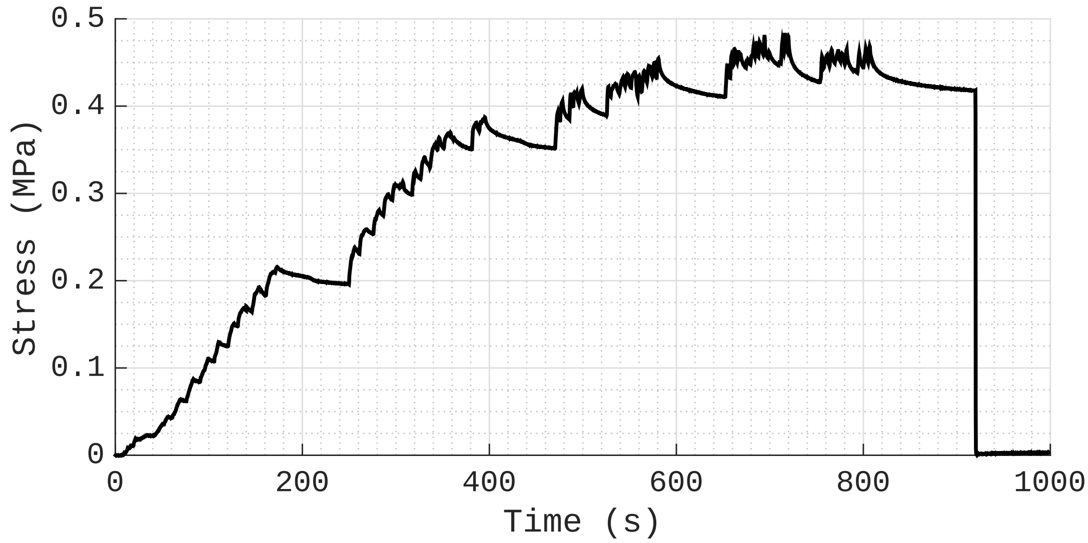

Figure 4.11: Load steps used at NCF experiment

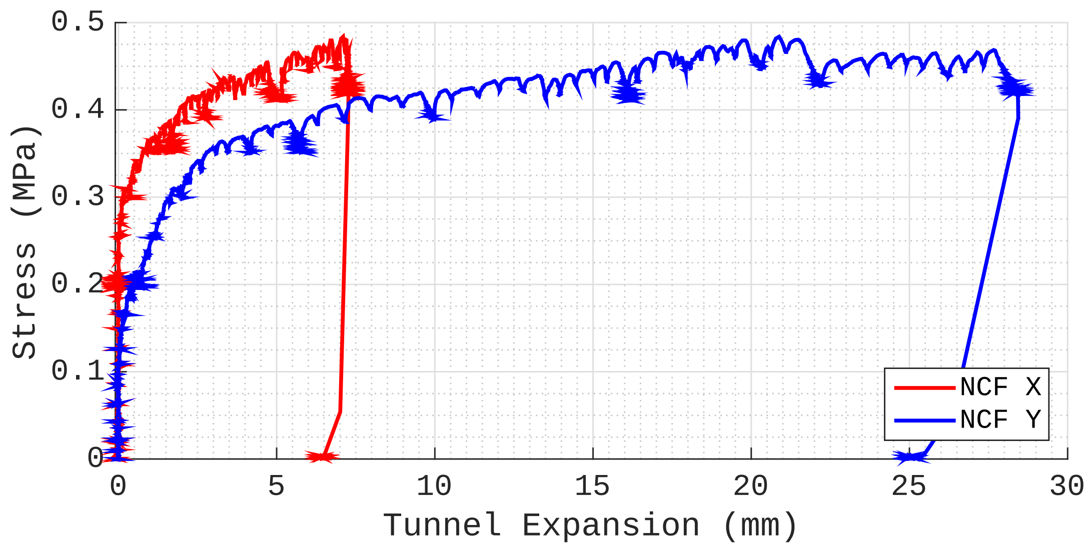

Figure 4.12: Expansion of tunnel opening at NCF experiment

Figure 4.13: Crack map after NCF experiment

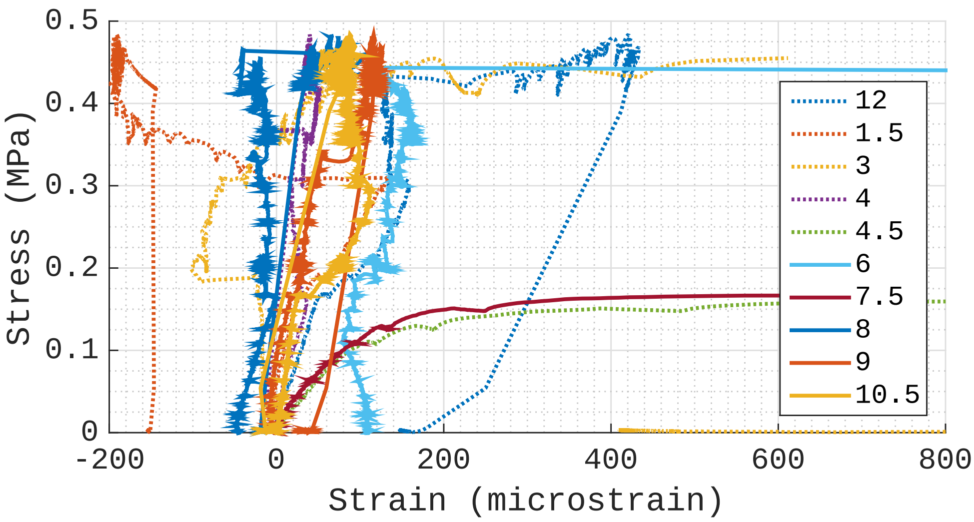

Figure 4.14: Lining strains measured at NCF experiment

4.4 Tunnel Test with Low Confinement (LC)

The experiment where the lining was confined by unstressed rock substitute layer is presented in this section. This case represents the tunnel being surrounded by a rock with negligible overburden pressure, which is a crucial parameter for pressurized tunnels. Low tensile strength of weak rock body is compensated by the shift of stress condition caused by the overburden pressure. It also defines the safety factor introduced in section 2.2 which is the ratio of overburden pressure to inner hydrostatic pressure. LC specimen was chronologically the first test, therefore some key variables were different compared to the other tests. Outer formwork of the rock substitute was in the form of a decagon in order to get its shape close to a circle (Fig. 4.15). Concrete of lining was casted one week after the implementation of three-layered rock substitute. There were perfect contact between rock substitute and lining.

Figure 4.15: Appearance of laboratory model at LC experiment

The stress-strain condition of rock substitute was very critical in this test, therefore strain rosettes were attached to the top face of rock layer in several places. On the rock body, tangential tensile stresses decrease while the distance from center increases. In order to see this behavior clearly, strain gauges were attached on three different radii

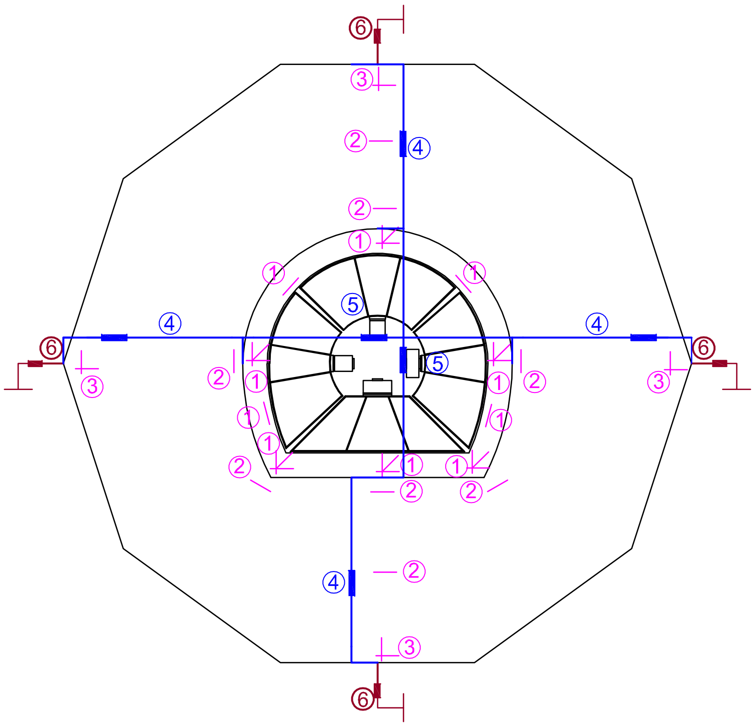

Figure 4.16: Instrumentation used at LC experiment

of the rock substitute; first batch of strain gauges was placed 2 cm away from the lining-rock substitute interface (0.9 m from center), intermediate batch was applied on the middle of rock substitute (1.4 m from center point) with tangential strain gauges only and last batch was close to outer edges (1.9 m from center) (Fig. 4.16). All strain gauges on the surface of rock substitute had 60 mm gage length. On tunnel lining, six 10 mm 45-degree strain rosettes were applied along with four tangential strain gauges. Ten LVDTs measured absolute displacements, contraction of rock thickness around lining and expansion of tunnel opening on horizontal and vertical directions.

Experiment was conducted on 5 May 2017 and lasted approximately 45 minutes. Data was recorded twice every second on 52 channels. Unit load step of hydrostatic pressure used in this experiment was approximately 800 kPa. Between each load step, crack patterns were drawn and widths were recorded. Magnitude of load steps were decreased to 21 kPa after this experiment, in order to enable coordination between load steps and optical system, also to clearly observe crack widths.

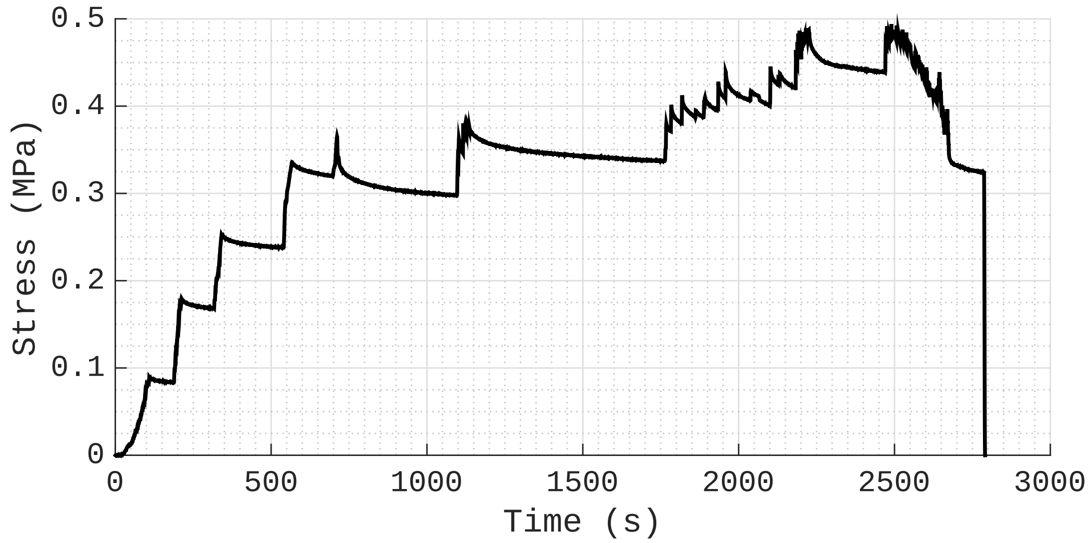

Figure 4.17: Load steps used at LC experiment

Up to 320 kPa, the response of laboratory model was very stiff; all strain gauge readings remained within the elastic limits. Nonlinearity started after 340 kPa, when the rock substitute cracked from the outermost edge, at 4:30 o'clock direction, propagating towards right corner of the lining (Fig. 4.18).

Most important outcome of this experiment was location of the crack initialization. The intactness of rock substitute was lost, after its brittle failure. Moreover, rock substitute partially detached along bottom lining border. Hence, the boundary condition of lining suddenly changed. In the right corner, rock substitute was not contributing to total stiffness anymore, therefore stress on lining rose abruptly. One load step later, at 360 kPa, a hairline crack was observed on the second stress concentration area (left corner) as well as two continuous cracks starting from inner boundary of lining to the mid depth of rock substitute. After 360 kPa, concrete on the right corner was fully cracked and only reinforcement bars were active. Rebars were able to sustain some more damage due to strain hardening. Their contribution to tunnel behavior was visible on horizontal tunnel expansion curve after 400 kPa (Fig. 4.19).

Strain gauge readings on the first crack zone (4:30 o'clock direction) showed that the plastic deformation of rock substitute started after 180 kPa, whereas this value was 250 kPa for the lining. Similar to the tests with no rock (NC and NCF), compression was observed on center of the invert (6 o'clock on Fig. 4.20). Other readings on rock

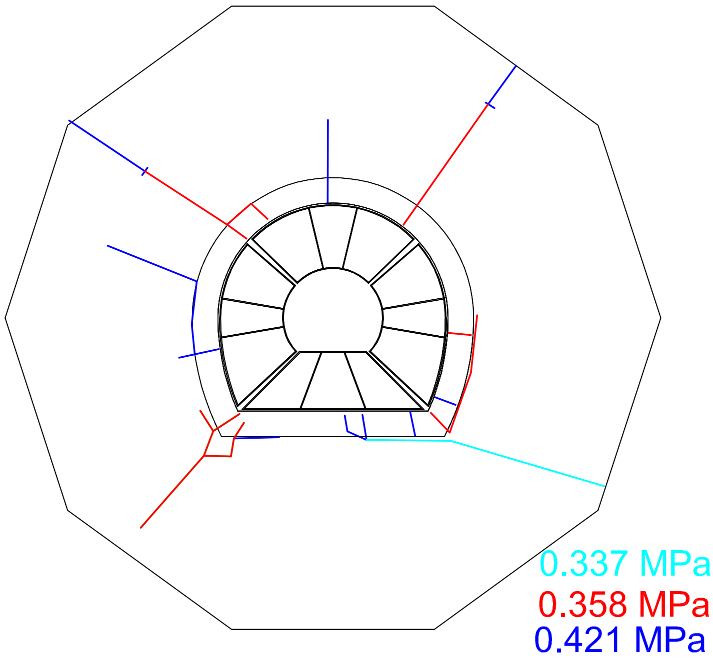

Figure 4.18: Crack map after LC experiment

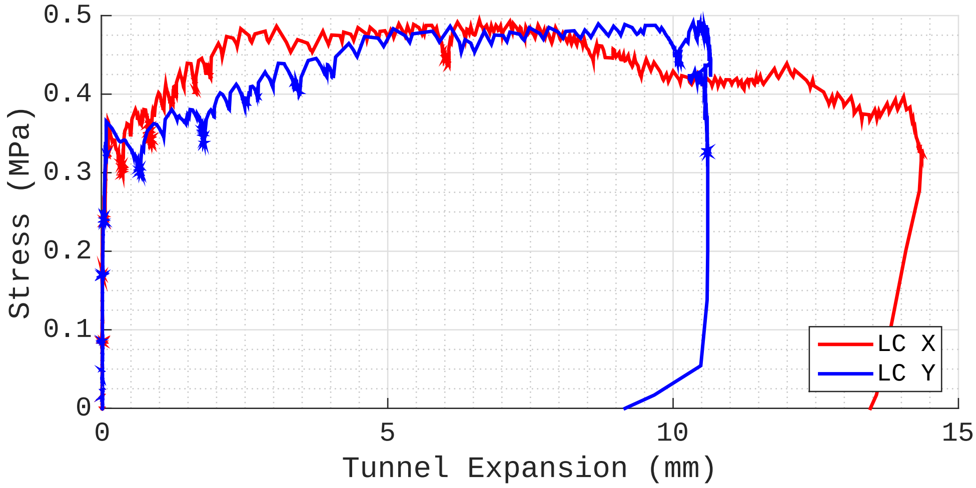

Figure 4.19: Expansion of tunnel opening at LC experiment

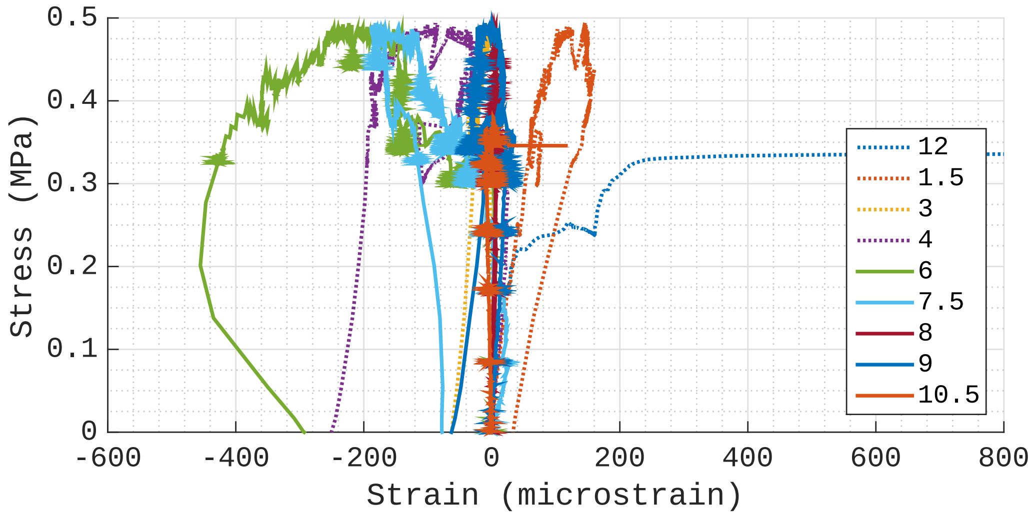

Figure 4.20: Strain readings on lining at LC experiment

substitute remained on elastic limits (Fig. 4.21). Absolute displacements measured from four ends of the laboratory model (Fig. 4.22) showed that two horizontal outwards movements were almost identical up to 480 kPa, after the separation of rock substitute, displacement on 3 o'clock was slightly larger. However, along vertical axis, outwards movement on 12 o'clock direction was much smaller than that of 6 o'clock. This behavior was caused by the irregular geometry of lining.

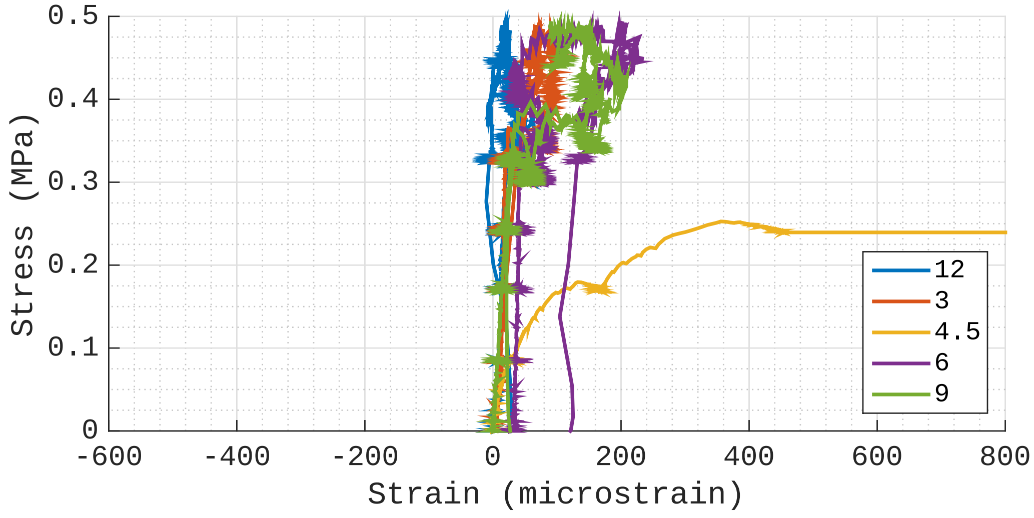

Figure 4.21: Strain readings on rock substitute at LC experiment

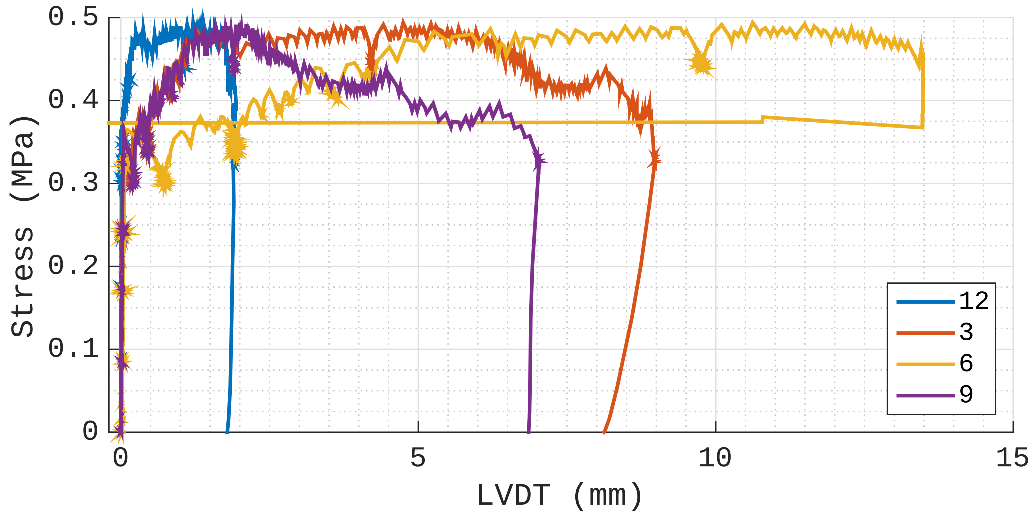

Figure 4.22: Absolute LVDT readings at LC experiment

Figure 4.23: Photograph during the execution of LC experiment

4.5 Tunnel Test with High Confinement in Perfect Contact Condition (HCP)

This section covers the test where the lining was confined by the rock substitute, and the interface between them was ideal. HCP experiment provided an upper limit to tunnel's initial stiffness and capacity under hydrostatic pressure. Tunnel lining was not only surrounded by intact rock mass, but in-situ overburden pressure was implemented on rock substitute as well. Applied confining force represented a tunnel under 60-100 meters below rock body, which is a high confinement level. Compressive stress was implemented to rock substitute with a prestressing mechanism as explained in Section 3.5. The prestressing mechanism required rock substitute to have straight edges at quadrants. Therefore, outer shape of rock substitute was converted to an octagon. The shortest rock depth from lining was kept the same with LC test which was 820 mm.

Preparation phase started with the implementation of rock substitute. Then, reinforced concrete lining was casted with one centimeter gap along rock substitute interface (Fig. 4.24). Loading system and prestressing mechanism were placed, and all measuring devices were set up respectively. When the concrete layers of rock substi-

Figure 4.24: Appearance of laboratory model at HCP experiment

tute gained their 28^{th} day strength, prestressing was applied. The lateral to vertical pressure ratio k_0 was selected as 1 and mean horizontal and vertical pressure were 1.33 MPa. These three values indicate that the principal stress was also 1.33 MPa. After the rock substitute reached its in-situ stress strain state, the gap at lining-rock interface was filled with a repair mortar (Sika Monotop 612) to provide perfect contact between lining and rock substitute. This construction order ensured a stress free lining prior to test.

Instrumentation used in this experiment consisted of 10 strain gauges on lining, 6 strain gauges on rock substitute which were 20 millimeters apart from lining-rock interface, 4 LVDTs on outer rim measuring absolute displacement of laboratory setup, 4 LVDTs recording response of rock substitute and 2 LVDTs monitoring the expansion of tunnel opening. Response of prestressing mechanism during the experiment was controlled by means of 6 load cells. Apart from the classical measurement system, DIC was implemented during this experiment. Two cameras were set up above stress concentration areas of lining (two bottom corners). After the test, the laboratory model was tested again, this time with two more cameras to observe the crown area of the lining (Fig. 4.25).

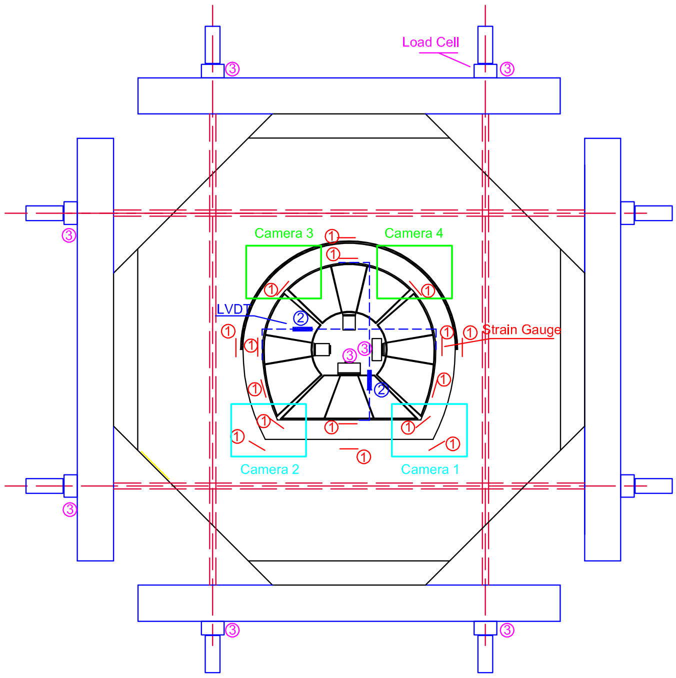

Figure 4.25: Instrumentation used at HCP experiment

HCP experiment was conducted on 1 November 2017, within 55 minutes. Two data set per second was recorded by the data acquisition system and cameras captured one shot per 5 seconds. Unit load step was 21 kPa in order to have a smooth coordination between loading system and optical system (Fig. 4.26). Inner hydrostatic pressure reached almost to the capacity of the loading system (1.2 MPa) in this experiment. No visible cracks were present throughout the HCP experiment. However, plastic deformations, had occurred according to strain gauge readings (Fig. 4.27). On the bottom corners, cracks developed after 580 kPa which were not visible to naked eye. However, crack patterns were easily differentiable to the optical measurement system (Fig. 4.28). Also the existence of a crack on the proximity of 10:30 o'clock direction was deductible. The sudden change in readings of strain gauge on 10:30 o'clock direction from compression to tension was indicating a change in the stress flow. But the crack on this region was also not visible to naked eye, and would be missed if the region was not being monitored with cameras (Fig. 4.29). Similar to crack on 1:30 o'clock direction, it did not affect strain gauges close to it. Some disturbances

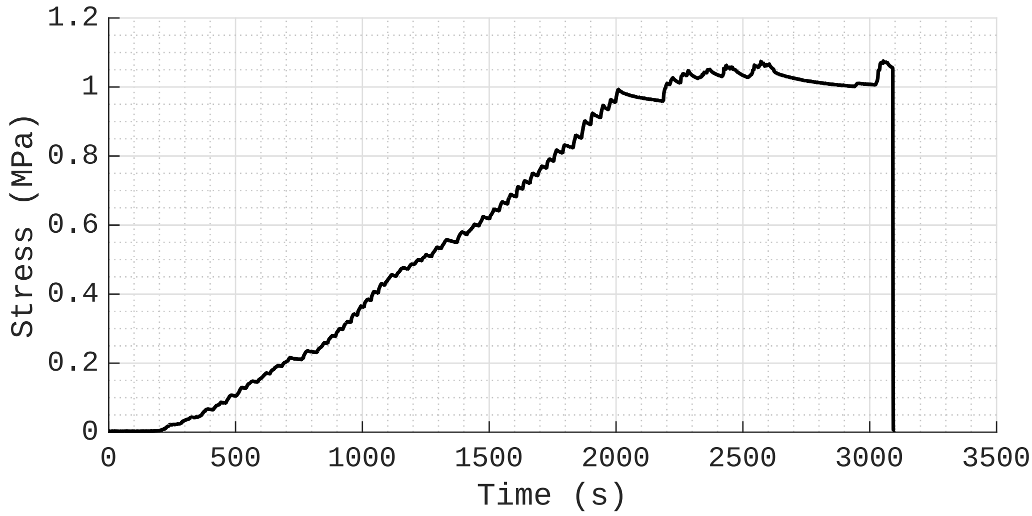

Figure 4.26: Load steps used at HCP experiment

were present on camera 4 (top right camera), nonetheless a distinguishable pattern was captured.

In this most favorable boundary condition, factor of safety was above one, the overburden pressure on rock substitute was 1.33 MPa and inner hydrostatic pressure was increased up to 1.1 MPa. Overall behavior of tunnel was very close to elastic (Fig. 4.30), and measured deformations were very small, relative to other experiments. At full capacity of other experiments, 600 kPa, horizontal and vertical tunnel expansions were almost 0.05 and 0.1 mm, respectively.

The day after HCP experiment, laboratory model was reloaded up to 1.1 MPa again (Fig. 4.32). Aim was to check the linearity of its behavior, and to identify the third non-visible crack on the left side of crown. Therefore, two more cameras were set up above the interested area. Equal load steps were not used in this part of the experiment. Behavior of tunnel was considered to be linear, strain gauge readings on lining (Fig. 4.33) and rock (Fig. 4.34) were within 100 and 150 microstrain respectively and were indicating elastic response. This check revealed two more cracks on the crown area, also enabled the specimen to be used with another boundary condition, HCI.

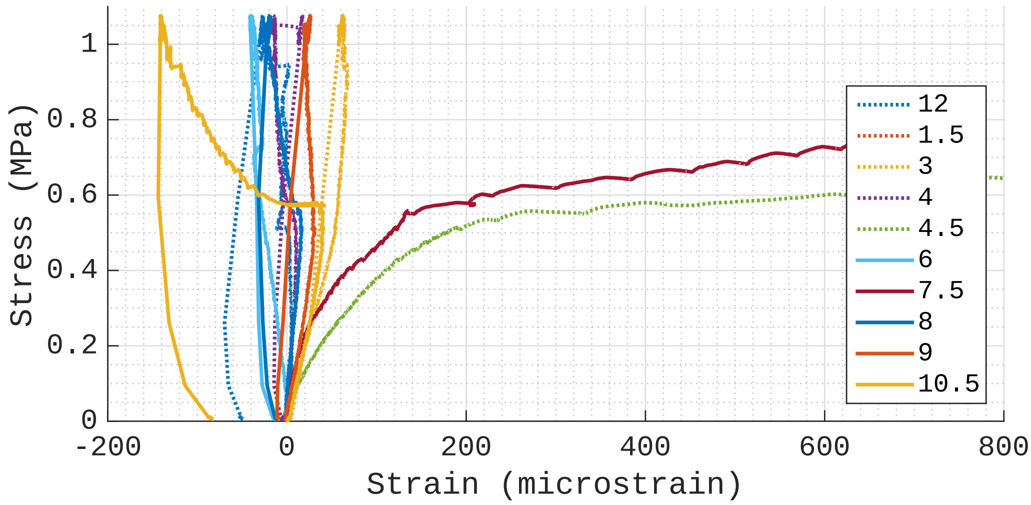

Figure 4.27: Strain readings on lining at HCP experiment

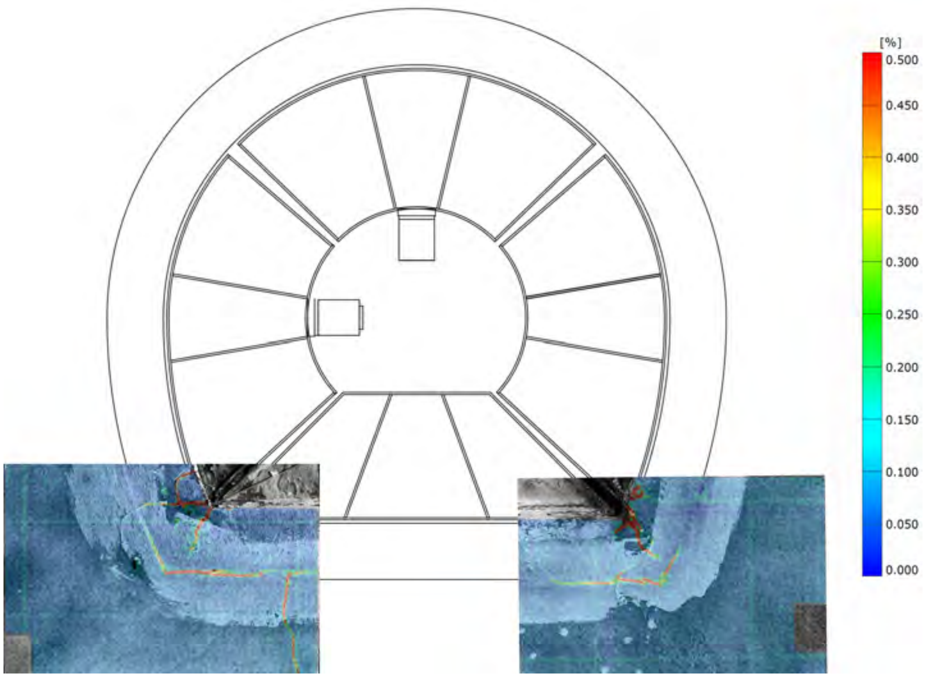

Figure 4.28: DIC results from HCP experiment

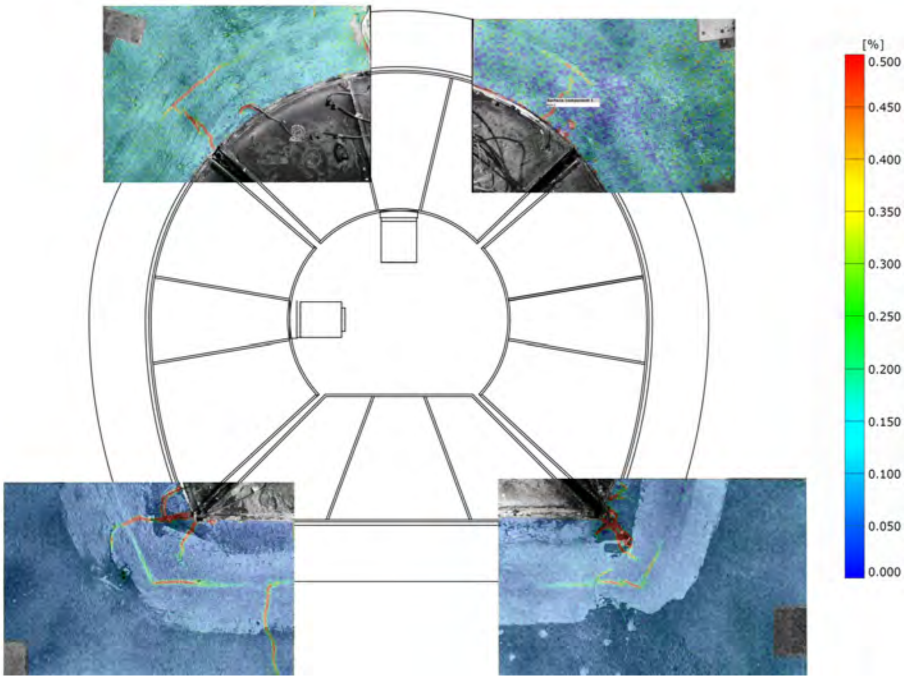

Figure 4.29: DIC results from HCP experiment (2^{nd} run)

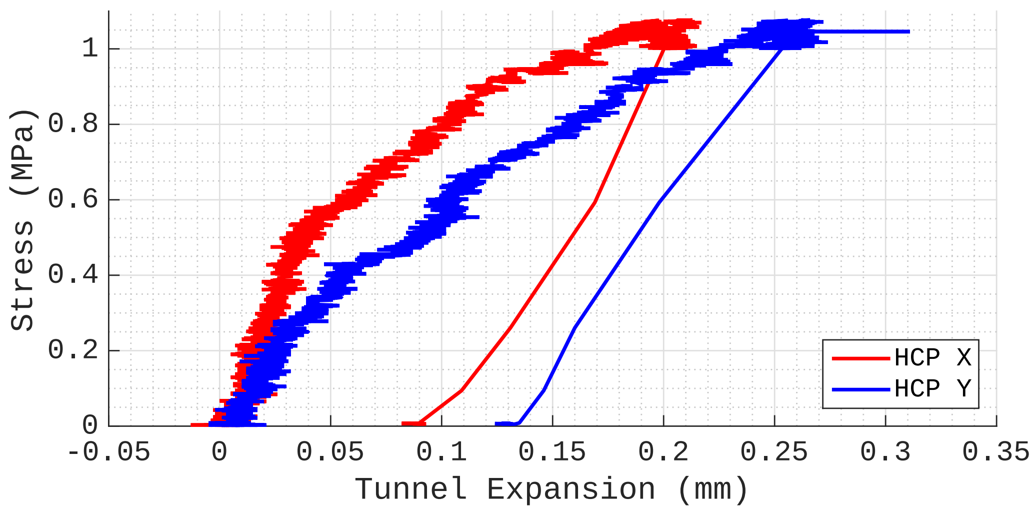

Figure 4.30: Expansion of tunnel opening at HCP experiment

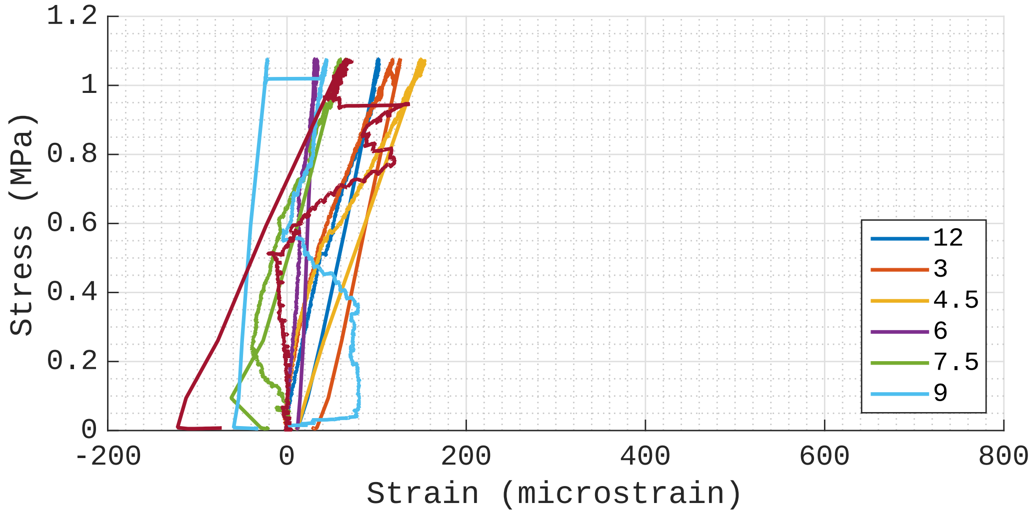

Figure 4.31: Strain readings on rock substitute at HCP experiment

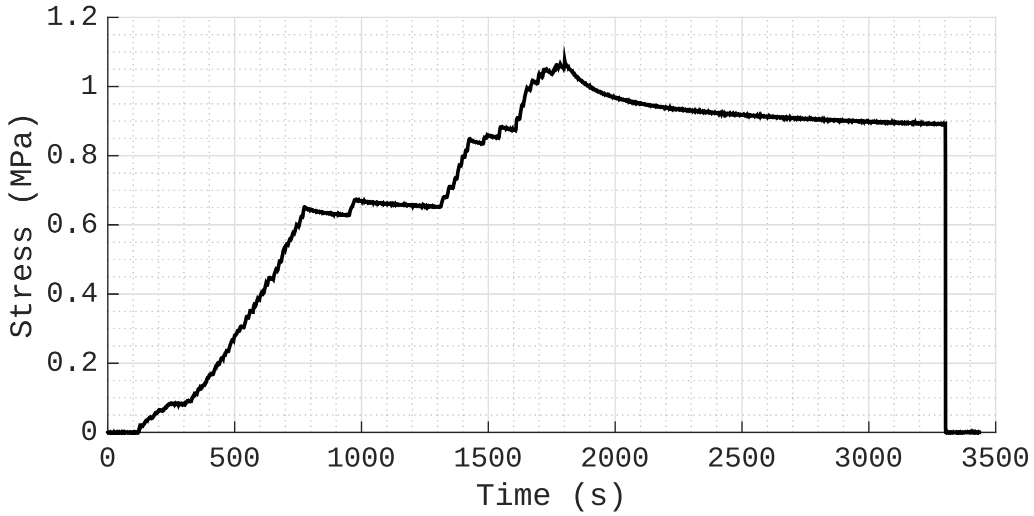

Figure 4.32: Load steps used at reloading of HCP experiment

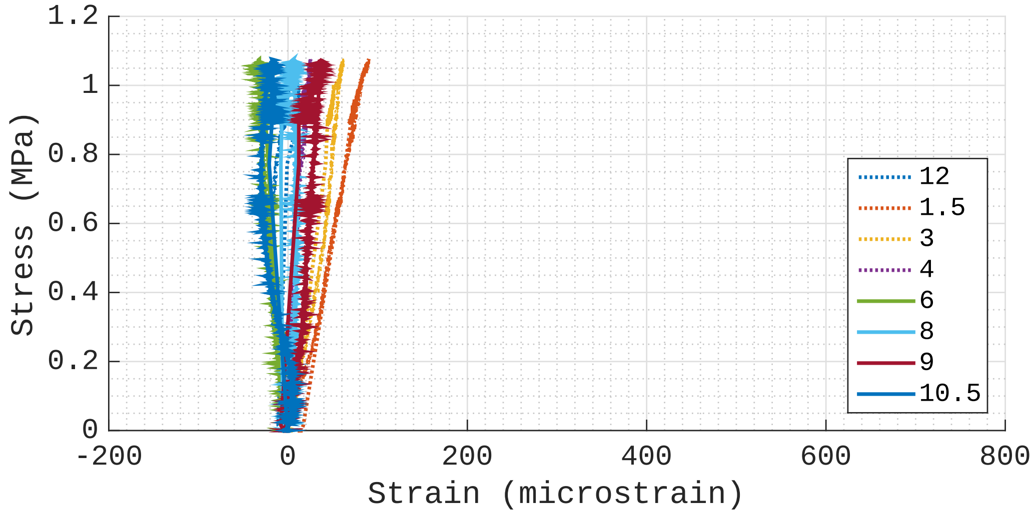

Figure 4.33: Strain readings on lining at reloading of HCP experiment

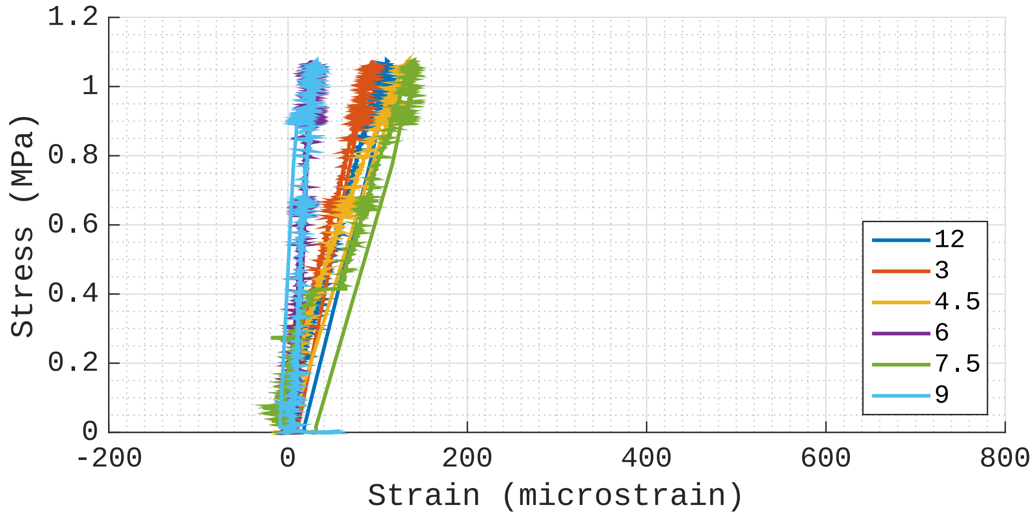

Figure 4.34: Strain readings on rock substitute at reloading of HCP experiment

4.6 Tunnel Test with High Confinement in Imperfect Contact Condition (HCI)

The experiment which investigated deficient contact condition between tunnel lining and rock body is presented in this section (Fig. 4.35). The importance of faulty interface comes from the design assumption that states perfect contact condition is required to distribute pressure to lining and overlying stratum proportional to their elasticity moduli. When this requirement is not met, due to size of the gallery, incorrect casting or shrinkage of concrete, the load capacity of tunnel decreases significantly. To create this boundary condition, laboratory model used on HCP experiment was modified. Tunnel lining and rock substitute were not replaced, but a gap was created at their interface. Discontinuity was planned on the crown part of the lining, so first the interface was marked carefully using a hammer drill. In order to separate two layers, a jackhammer was used to connect drill marks. After separating tunnel lining from rock substitute, monitoring tools were applied to the specimen. Instrumentation used on HCI experiment was similar to HCP, i.e. same classical measurement equipment was used, optical system consisted of five cameras, four of them focused on critical areas and one observing general behavior (Fig. 4.36).

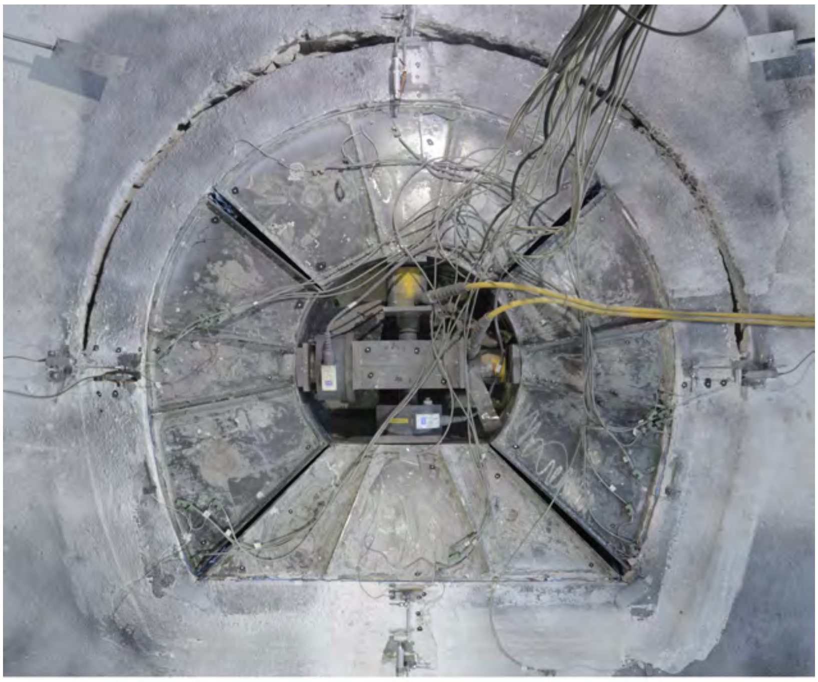

Figure 4.35: Appearance of laboratory model at HCI experiment

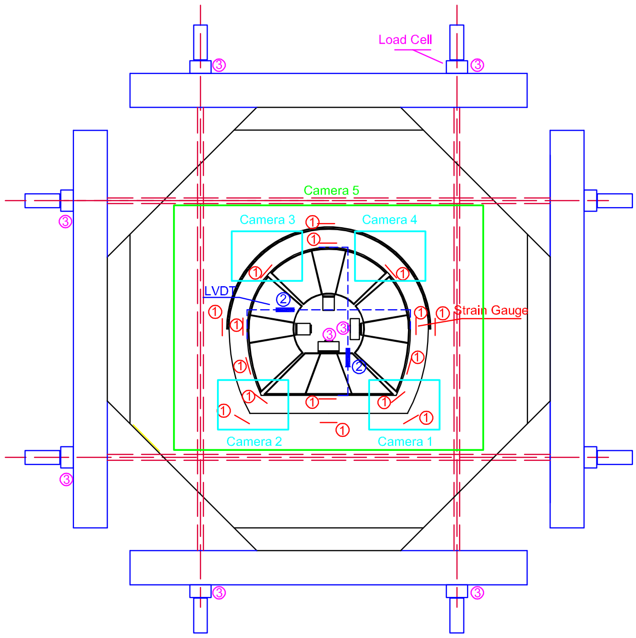

Figure 4.36: Instrumentation used at HCI experiment

HCI experiment was conducted on 30 November 2017, and lasted 35 minutes. Data acquisition systems worked with two data set per second, and four cameras recorded images with one shot per 7 seconds. The change of frequency on optical system was due the fact that data transmission speed of usb cables were not capable to meet requirements by increased number of cameras. Unit load step was 21 kPa for HCI experiment (Fig. 4.37). Behavior of tunnel opening was already prone to show larger deformations along vertical axis due to its geometry. This new boundary condition of lining amplified the ratio of vertical to horizontal deformation (Fig. 4.38).

Four micro-cracks were already present on lining from the HCP experiment. These cracks were at the stress concentration areas (bottom corners) and at the left and right shoulders of the lining. When the applied load passed hydrostatic pressure equivalent to 110 kPa, one of the existing cracks (right corner) started to widen, according to strain gauge readings on lining (Fig. 4.39). Other pre-existing cracks however, did not show such a behavior up to 420 kPa (Fig. 4.41). From 420 to 500 kPa, rest of the existing cracks reached to a strain value of 0.01. A new crack occurred on right shoulder, at 500 kPa, and penetrated through the strain gauge at 1.5 o'clock direction. Following that, a total of 8 observable cracks occurred until the end of the experiment. Just like bottom corners, a crack that was not noticed during experiment on the crown was traced by DIC program (topmost crack on left crown camera, Fig. 4.42). When the input files of DIC were checked, the crack was still not visible to naked eye.

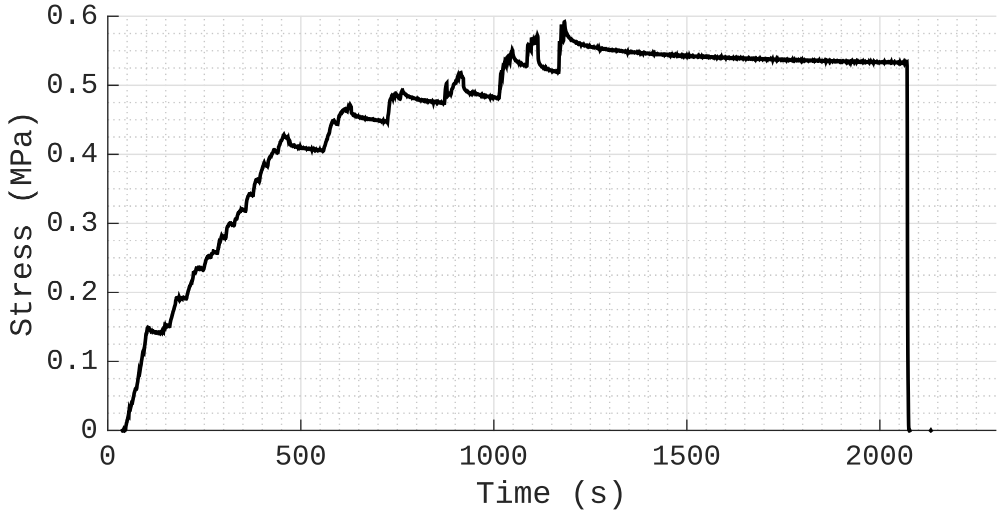

Figure 4.37: Load steps used at HCI experiment

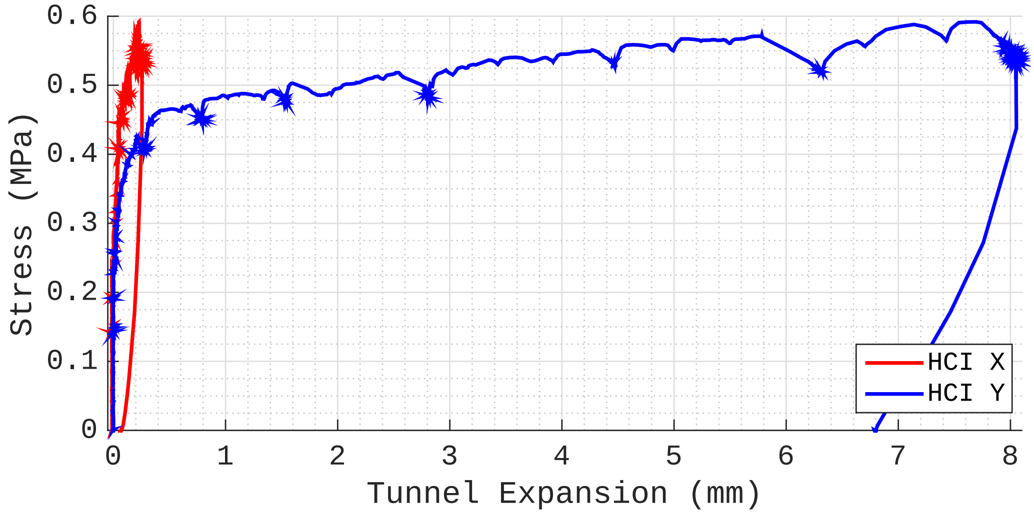

Figure 4.38: Strain readings on lining at HCI experiment

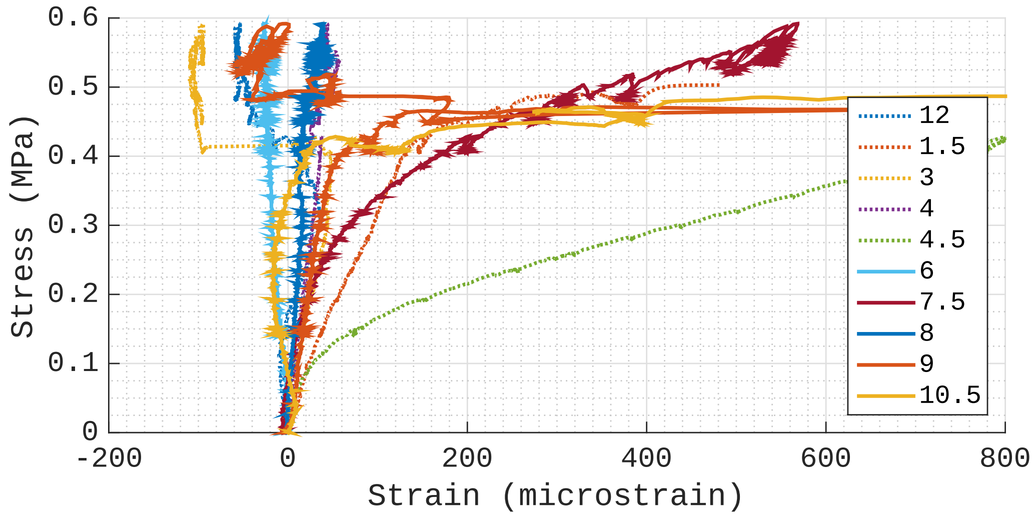

Figure 4.39: Strain readings on lining at HCI experiment

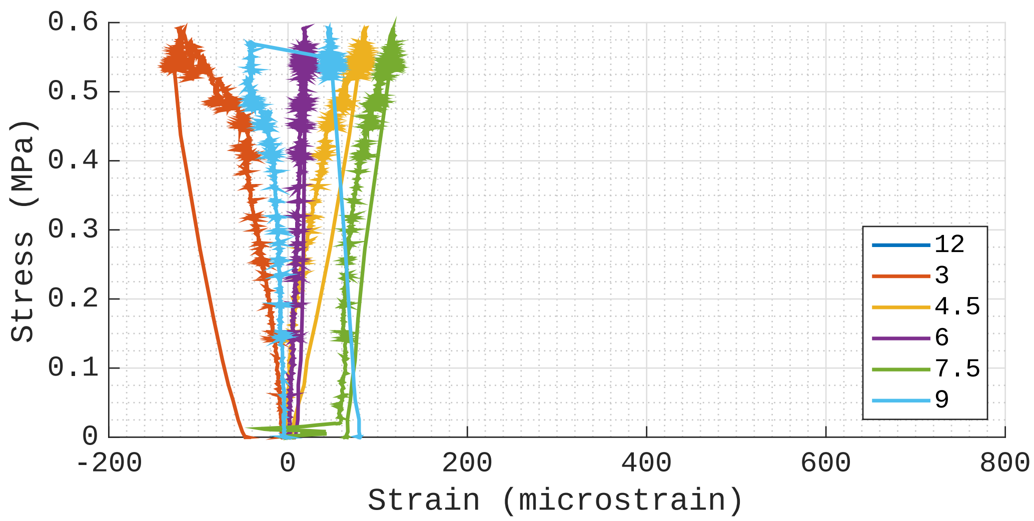

Figure 4.40: Strain readings on rock substitute at HCI experiment

Although the specimen could be tested up to 20 mm vertical displacement, HCI test was conducted within the serviceability limits, because the same specimen was tested after repairing as HCIR.

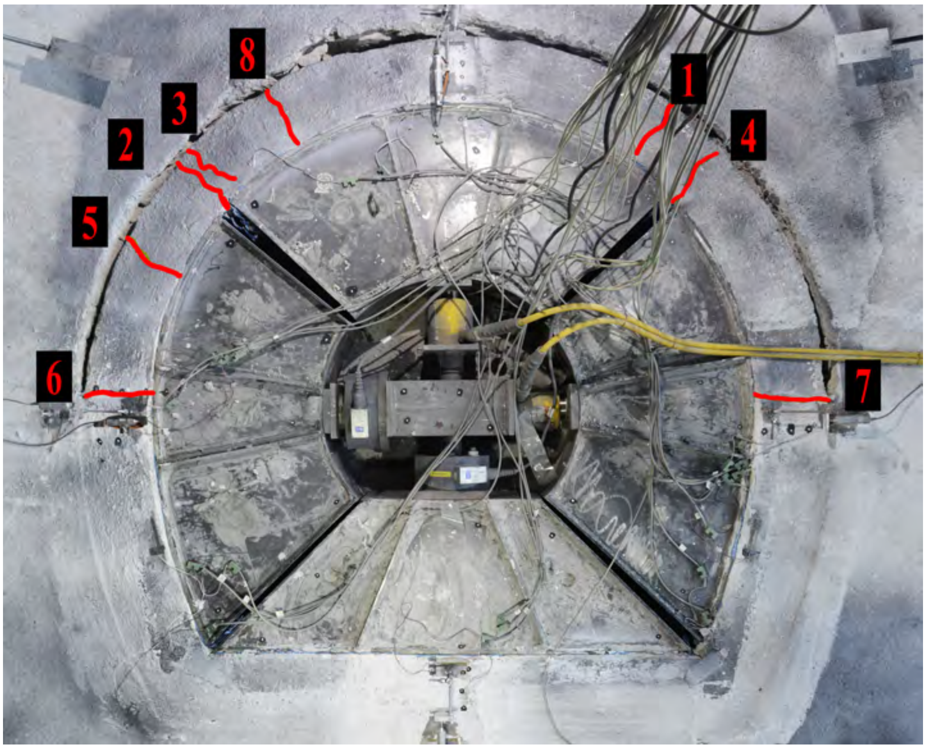

Figure 4.41: Crack map observed during HCI experiment

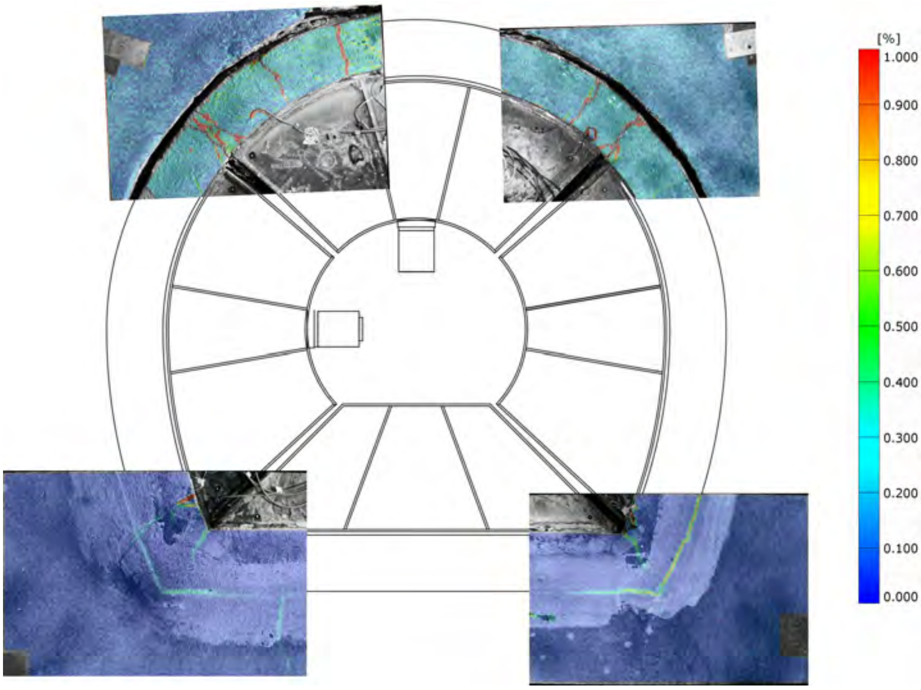

Figure 4.42: DIC results of HCI experiment

4.7 FRP-Repaired Tunnel Test with High Confinement in Deficient Contact Condition (HCIR)

This section covers the experiment that investigates the behavior of repaired lining. HCI specimen which was carefully tested within serviceability limits was repaired with fiber reinforced polymer fabric (FRP). The investigation of performance of repaired specimens is very important, since re-construction of energy tunnels are financially not possible.The repair was done by first applying Sikadur-30 to tunnel face, then cutting and placing 14-cm wide SikaWrap 300 C/60, and finally brushing the FRP fabric to embed it inside Sikadur-330.

Figure 4.43: FRP application

Following HCI experiment, LVDTs and loading system were removed, and plastering on the inner facade of the lining was removed. Concrete to be repaired has to be intact, and its surface needs to be rough. Therefore, an epoxy based repair mortar was used to create an approximately 2 mm thick cover on top of the surface. Cracks were not filled with repair mortar, but just covered. 24 hours later, 200 mm thick lining was ready to be repaired. Only 140 mm of the lining center was decided to be repaired, from one corner to the other along the arch (Fig. 4.43). FRP application sheet needs to be embedded into epoxy based resin, therefore, inner facade of the lining was marked, then a very thin layer of resin was applied in between marks. Properly cut FRP sheet was placed on top of first layer of resin, then a second layer

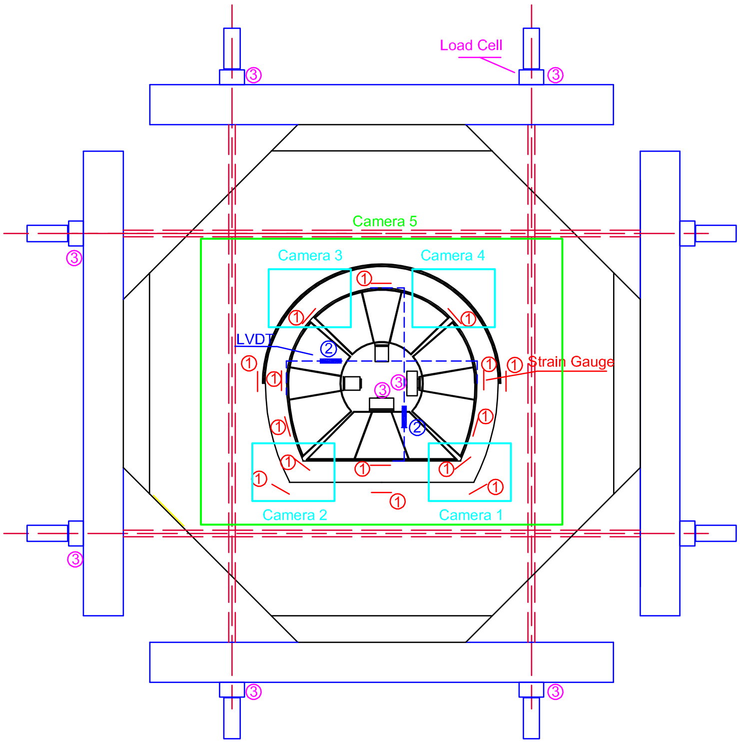

Figure 4.44: Instrumentation used at HCI experiment

was applied, which encased the FRP sheet in 1-mm thick resin. Strength of FRP layers was fully developed after 7 days. Instrumentation that was used on HCIR experiment was similar to HCP and HCI experiments. One important difference was the absence of strain gauges along crown part of the rock (Fig. 4.44).

HCIR experiment was conducted 7 days after FRP application, on 3 January 2018. It was concluded within 45 minutes (Fig. 4.45). Laboratory model was loaded using unit hydrostatic pressure steps of 21 kPa. FRP application increased the capacity of lining, the repaired cross section was able to reach approximately 1 MPa (Fig. 4.46). Similar to HCI experiment, the boundary condition or gap in crown interface, amplified the geometry driven bias in deformation direction (Fig. 4.47). Initialization of readable expansion on tunnel opening started after approximately 110 kPa, similar to NC and NCF experiments. This behavior can be related to existing cracks. This stiffness is preserved until magnitude of pressure reached maximum of HCI experiment. When 600 kPa was reached, a yield-like behavior was observed: larger deformations

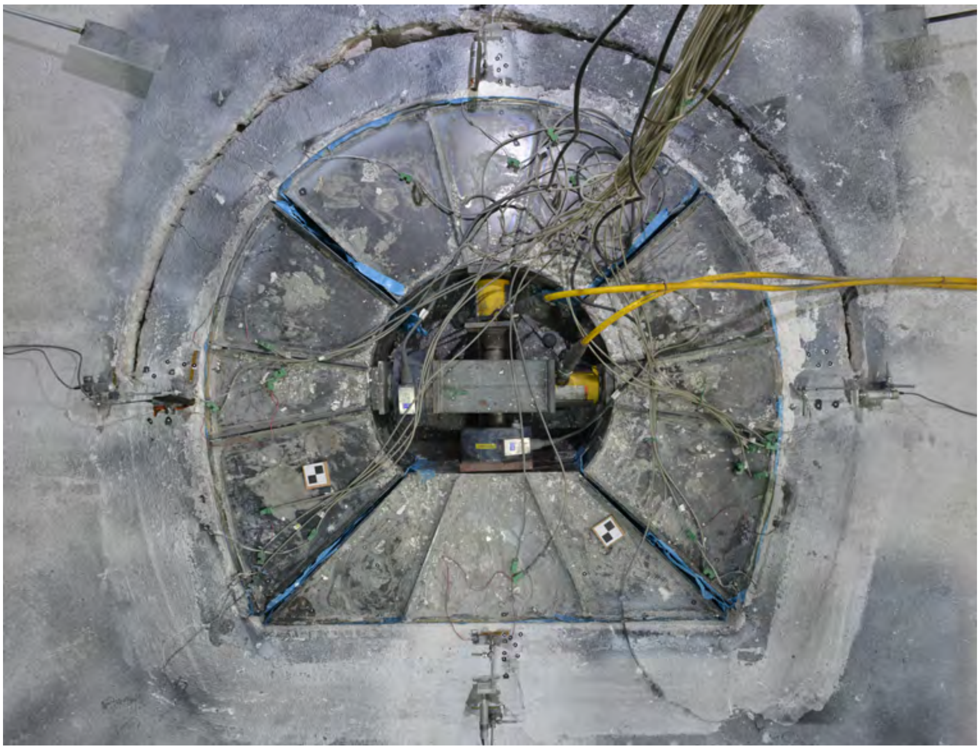

Figure 4.45: Appearance of laboratory model at HCIR experiment

were experienced with a relatively small stiffness until 750 kPa. Following this yield-like behavior, slope of expansion of tunnel opening- hydrostatic equivalent pressure graph increased until 0.95 MPa, which was the ultimate strength. Tangential strain gauges on surface of the lining measured similar behavior. Strain gauges that were replaced due to cracks on former experiments measured high strains at early stages (1:30, 4:30, 9:00, 10:30 o'clock directions in Fig. 4.48). Center of the straight bottom portion experienced compression, similar to other experiments. The stress concentration zone on the left (7:30 o'clock direction) cracked in the previous experiments, but unlike its symmetrical counterpart (4:30x' o'clock direction) it did not experience high strains at early stage. This result makes sense, since the initial perfect symmetry has been lost after plastic deformations.

Totally, 4 cracks formed on HCP test, prior to HCI. Two of which on the shoulders have already widened at HCI test, along with new cracks. On the other hand, no crack formation or widening were observed below the centerline of the specimen. From HCI test, 6 new cracks were known to be present on lining, above centerline (existing cracks are marked with green in Fig. 4.50). The crack map of HCIR experiment is

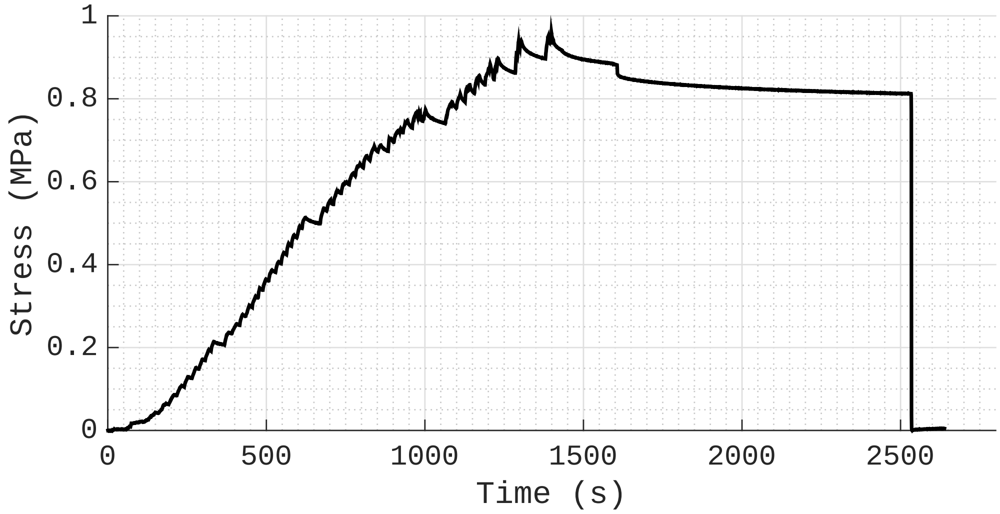

Figure 4.46: Loading steps used at HCIR experiment

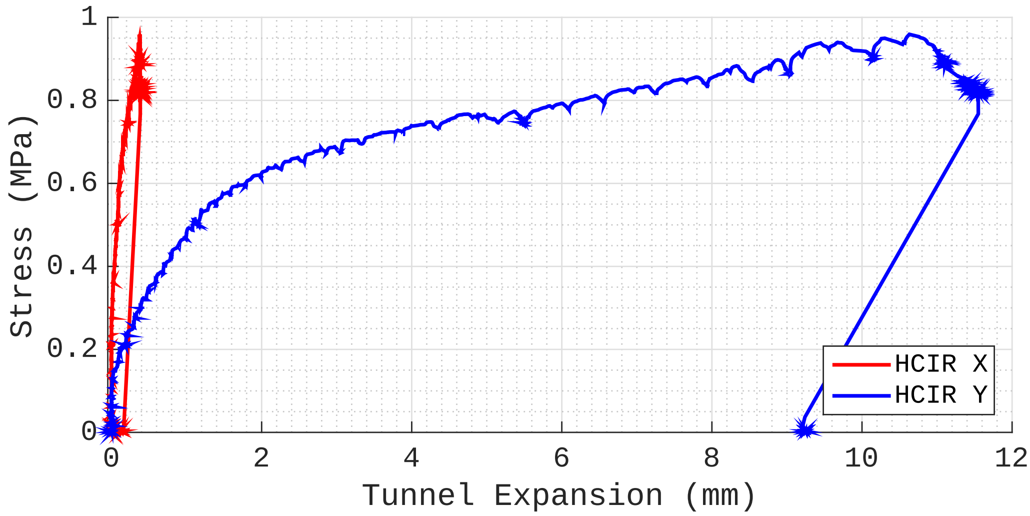

Figure 4.47: Expansion of tunnel opening at HCIR experiment

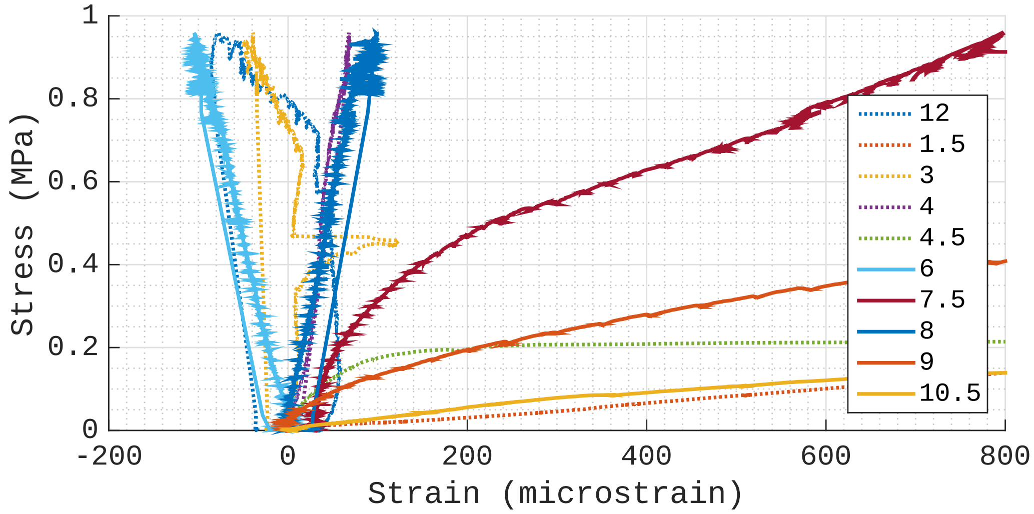

Figure 4.48: Strain readings on lining at HCIR experiment

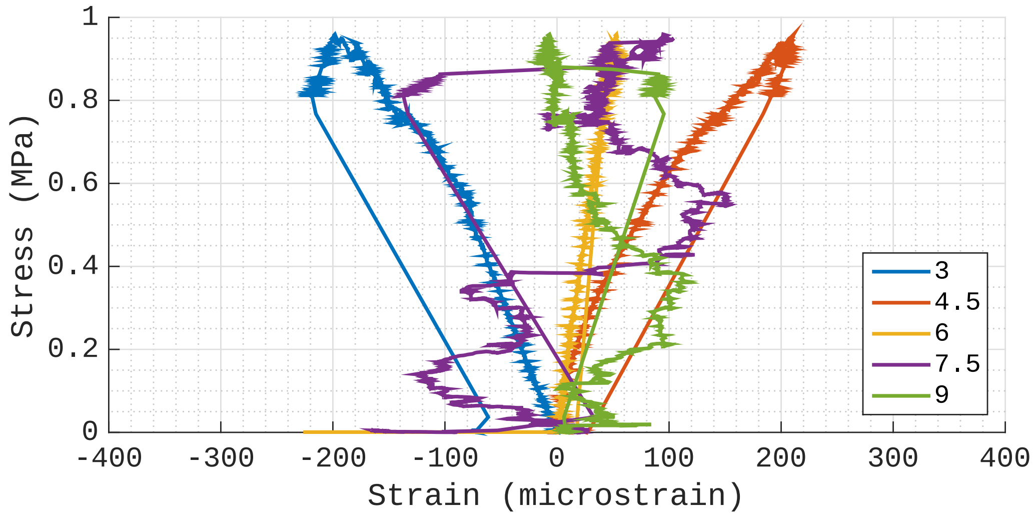

Figure 4.49: Strain readings on rock substitute at HCIR experiment

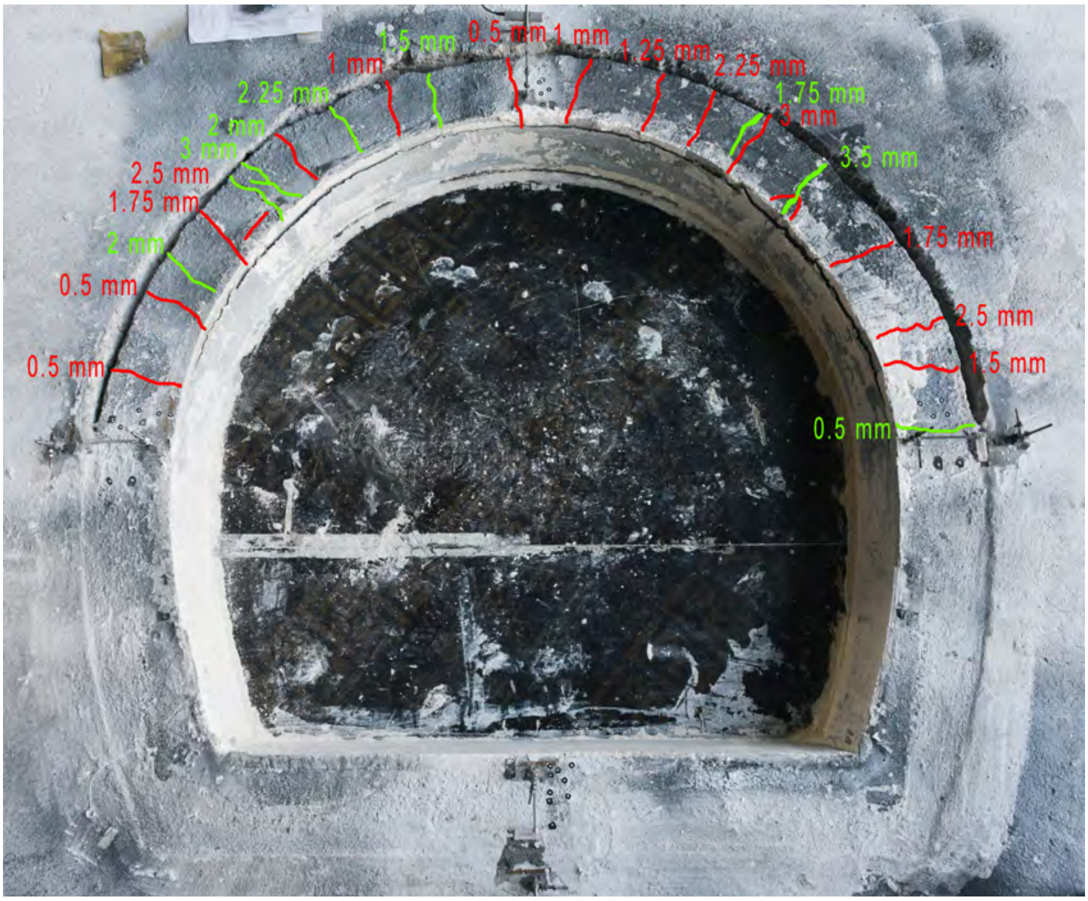

Figure 4.50: Crack map after HCIR experiment (cracks from previous experiment are marked with green)

much more condensed and equally spaced, relative to the other experiments. At the end of the HCIR test, total number of fully developed cracks spanning through lining cross section reached to 24 from 10 at HCI test (including 2 cracks on the bottom corners). All of these cracks were on the crown part of lining.

It must be stated that HCIR experiment was noisy compared to other experiments. That is to say at certain points, especially after 850 kPa, crushing sounds were audible, instead of clicks and crackle sounds that were present during other experiments, although no visible large cracks were present. The cause of these sounds was discovered after the removal of loading system and plastering around lining which was splitting of FRP from lining.

Figure 4.51: Appearance of laboratory model at HCIF experiment

4.8 Fiber Reinforced Tunnel Test with High Confinement in Imperfect Contact Condition (HCIF)

Performance of fiber reinforced concrete lining was investigated at the boundary of HCI (poor contact between tunnel lining and rock under high overburden pressure). Mechanical properties of fiber reinforced concrete were presented in Chapter 3.3. Lining belonging to HCIR experiment was carefully removed from rock substitute, rebars were prepared the same as other experiments, and concrete with new mixture recipe was casted (Fig. 4.51). One important difference on the preparation phase was the use of styrofoam as the outer formwork of the lining, to create a gap at the interface. The planned gap on the rock-lining interface was from one end of semicircle to the other end. Therefore, the inner facade of the rock substitute was coated with a 10 mm thick foam sheet. This foam coating was detached during formwork removal. The rock substitute was not changed and prestressing mechanism was not altered in the preparation phase of HCIF.

Two main measurement methods were used on HCIF experiment: traditional and

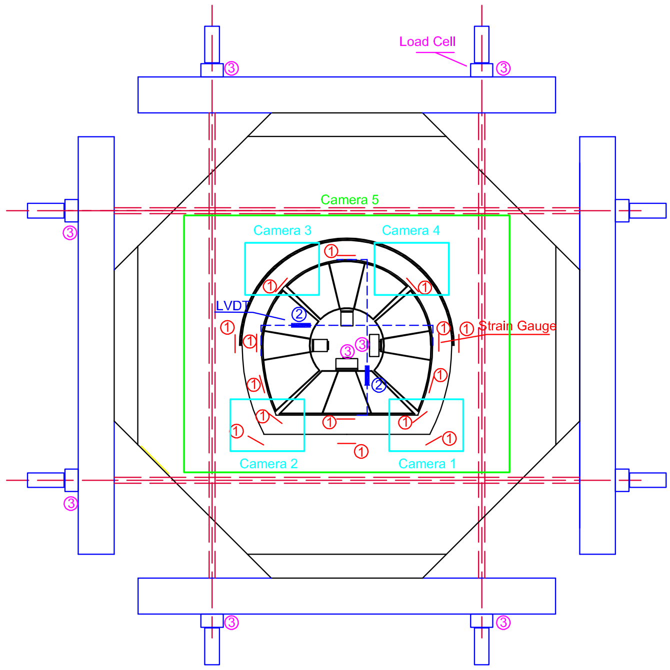

Figure 4.52: Instrumentation used on HCIF experiment

optical (Fig. 4.52) . First one consists of ten tangential strain gauges on the top face of the lining, and three on the rock substitute (4.5, 6, 7.5 o'clock directions), along with twenty LVDTs: four of them recording absolute movement of laboratory model, four on the steel sections, four on the rock substitute, four along the lining concrete and four on the tunnel opening. Visual monitoring system consisted of 2 LED spotlights and 5 local cameras: Four of them focused on the stress concentration regions and one on general movement .

HCIF experiment was conducted after the lining concrete gained 28^{th} day strength, on 28 March 2018. Whole experiment lasted about 40 minutes. Five data sets were recorded per second, a data set consisting of 49 channels. Unit hydrostatic pressure steps was selected as 21 kPa. After the section was fully unloaded, laboratory model was reloaded up to maximum load level, to check the linearity of and differentiate plastic deformations (Fig. 4.53). According to LVDT readings from tunnel opening, measurable deformation started after 300 kPa. This pressure value is higher compared to other experiments, which can be explained by prevention of micro-crack propaga-

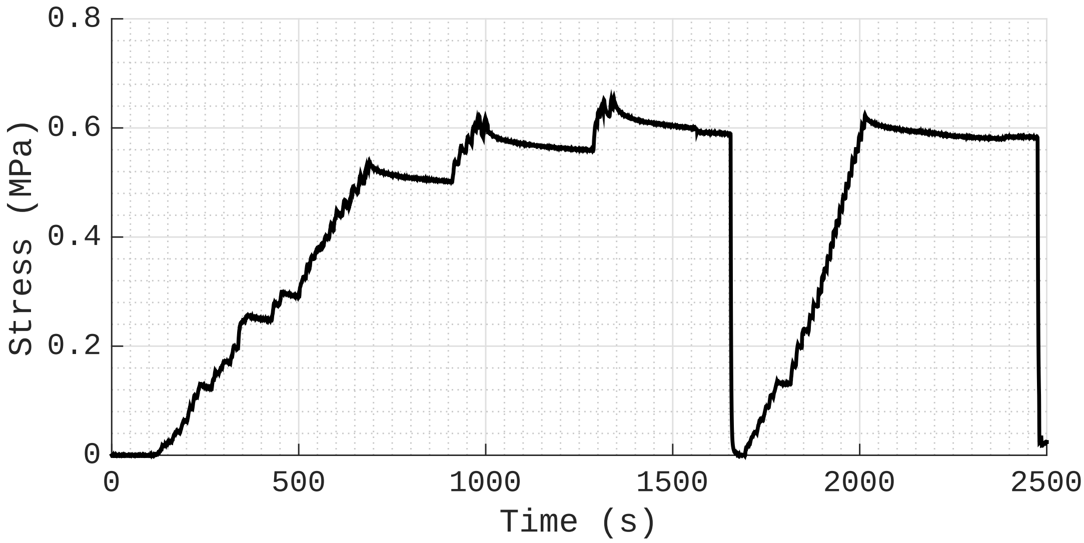

Figure 4.53: Load steps used at HCIF experiment

tion due to activated fibers. After this cracking point, deformations in unit load step have increased with a steady slope until 630 kPa. Starting from 630 kPa to the ultimate capacity of the section, 660 kPa, large deformations were observed with almost uniform crack width distribution along crown of lining, and with very little increase in hydrostatic pressure (Fig. 4.54). The first observed crack was on the middle of the crown, passing through 12 o'clock strain gauge (Fig. 4.55). Other plastic deformations captured by strain gauges were on two bottom stress concentration areas and 10.5 o'clock direction. Rest of the strain gauge readings on lining and rock substitute remained within elastic limits, invert of lining acted like a beam, rock substitute did suffer plastic deformations, similar to other experiments (Fig. 4.56).

First observed crack during the HCIF experiment was on 10.5 o'clock direction, at 520 kPa. When it was noticed, laboratory model was closely examined and another hairline crack was found at 12 o'clock direction (Fig. 4.57). Following the initial cracks at 520 kPa, crack widths were closely examined at hydrostatic pressures of 560 and 640 kPa, and 600 kPa at the reloading curve (Fig. 4.53). A total of 12 distinct crack patterns were present on lining, all but one on the crown of the section.

For retesting purpose, experiment was stopped after 660 kPa. Furthermore, the laboratory model was checked for linearity and magnitude of plastic deformations at the end of the experiment by loading up to 600 kPa hydrostatic pressure.

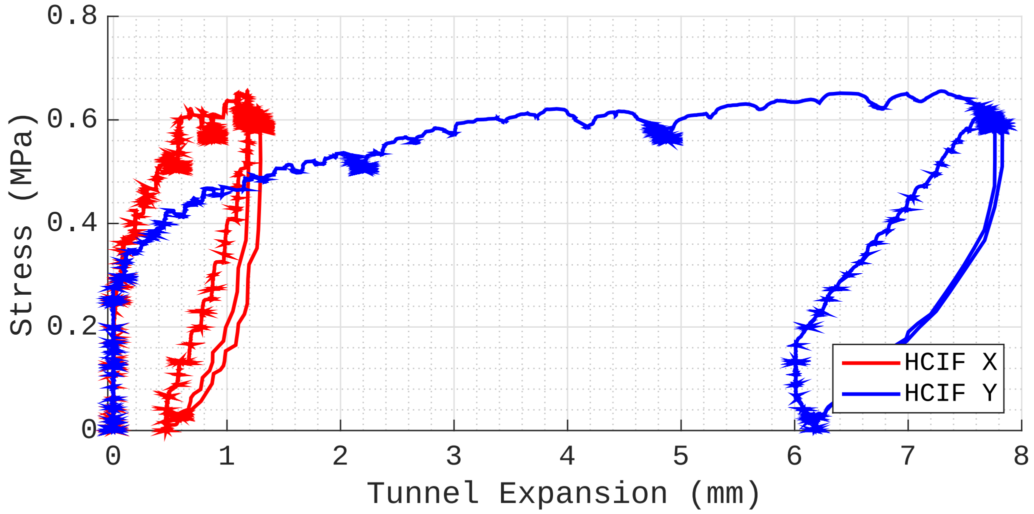

Figure 4.54: Strain readings on lining at HCIF experiment

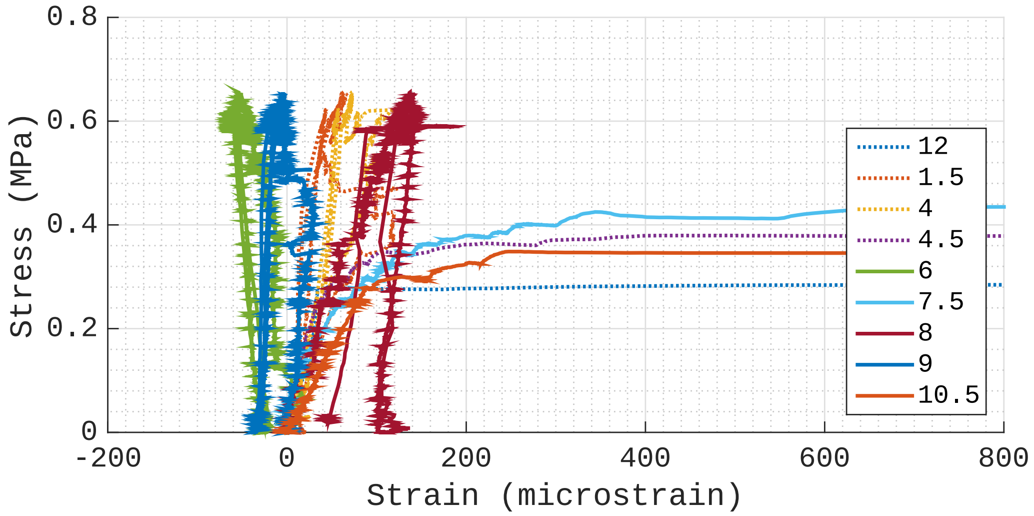

Figure 4.55: Strain readings on lining at HCIF experiment

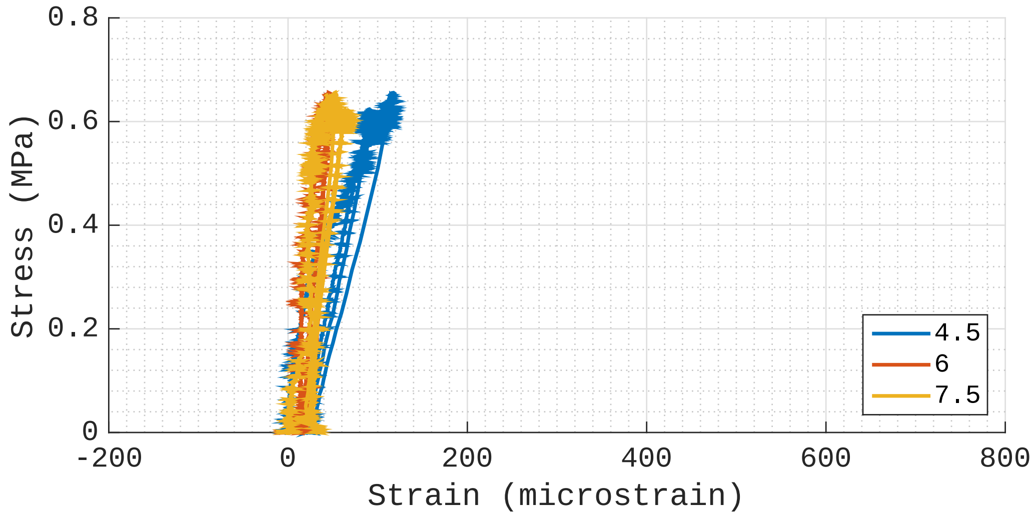

Figure 4.56: Strain readings on rock substitute at HCIF experiment

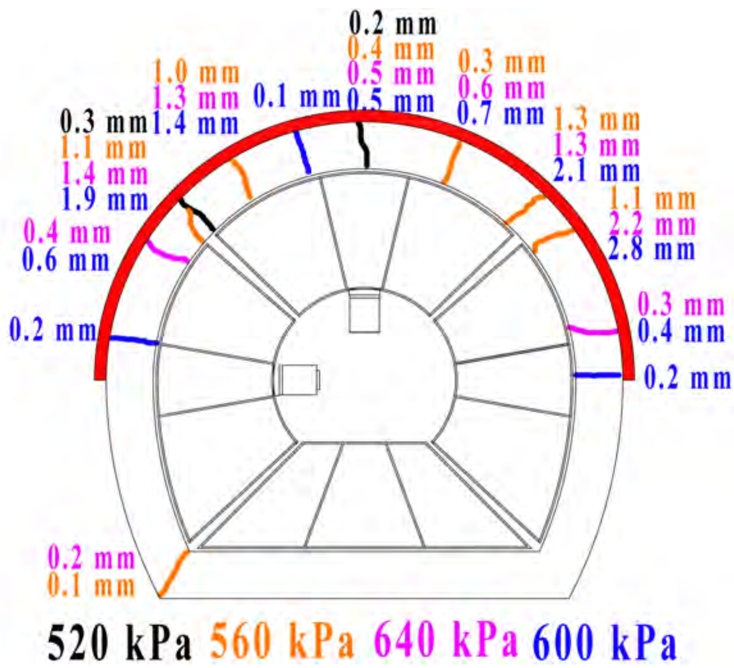

Figure 4.57: Crack map after HCIF experiment

4.9 Fiber Reinforced Tunnel Test with High Confinement in Improved Deficient Contact Condition (HCH)

An improved boundary condition compared to HCI, HCIR and HCIF experiments was investigated in the HCH experiment. All parts of the laboratory model that was used on HCIF were preserved, but the gap along crown of the rock-lining interface was partially filled. Two 400 mm long fillings were centered around 10:30 o'clock and 1:30 o'clock directions (Fig. 4.58). Filling material was the same repair mortar (Sika Monotop 612) as the HCP experiment. Instrumentation used on HCH was identical to HCIF; functional measurement equipments were kept, and damaged strain gauges were replaced. Since the lining was not changed from HCIF setting, HCH experiment was also assessing fiber reinforced concrete lining, similar to experiments NCF and HCIF.

Figure 4.58: Appearance of laboratory model at HCH experiment

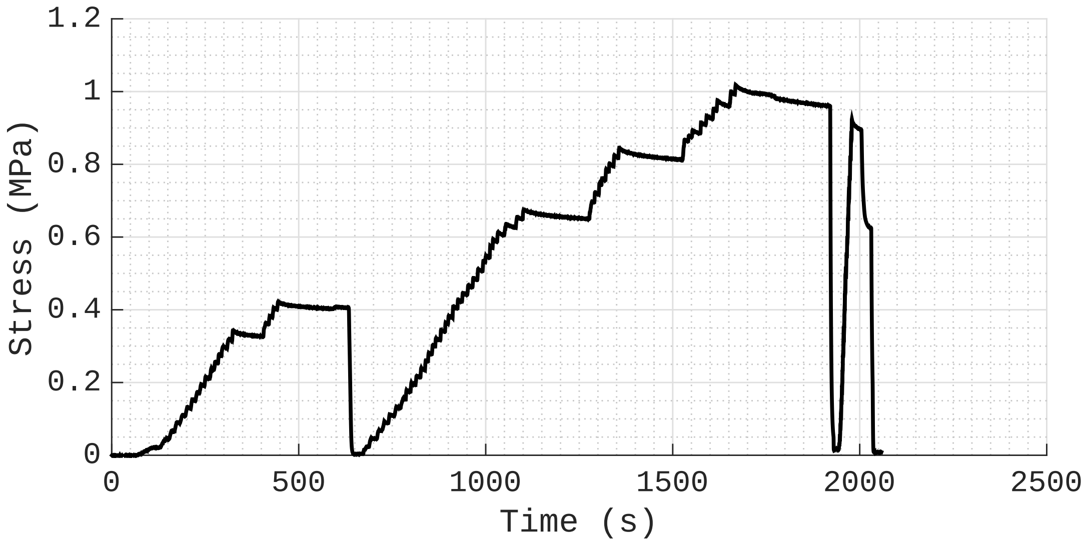

Figure 4.59: Load steps used at HCH experiment

Experiment took place on 04 April 2018, 24 hours after casting repair mortar. Hydrostatic pressure was applied to laboratory model with 21 kPa unit load steps (Fig. 4.59). Loading of the section was done in three cycles: hydrostatic pressure equivalent of load was increased to 0.4 MPa, unloaded, then loaded again up to 1.05 MPa, unloaded, then a third increase up to 0.9 MPa. Last cycle was applied rapidly, with no load steps, in order to check the linearity of behavior and magnitude of plastic deformations.

There were 12 residual cracks present at the lining concrete from HCIF experiment (Fig. 4.57). On lining, strain gauges at directions 4, 6, and 9 o'clock remained linear through the experiment (Fig. 4.61). All other readings indicated plastic behavior before 400 kPa. This experiment was investigating behavior of fiber reinforced concrete. Furthermore, the lining suffered large cracks in HCIF experiment. Therefore, readings on lining were not as significant as readings taken from surface of rock substitute. Assessment of lining's performance must be based on DIC results. Rock substitute, on the other hand, remained on linear elastic range and suffered rather small deformations (Fig. 4.62).

Crack widths were measured manually at hydrostatic pressure values of 400, 650, 850, and 1000 kPa (Fig. 4.63). These crack patterns are in perfect correspondence with DIC results.

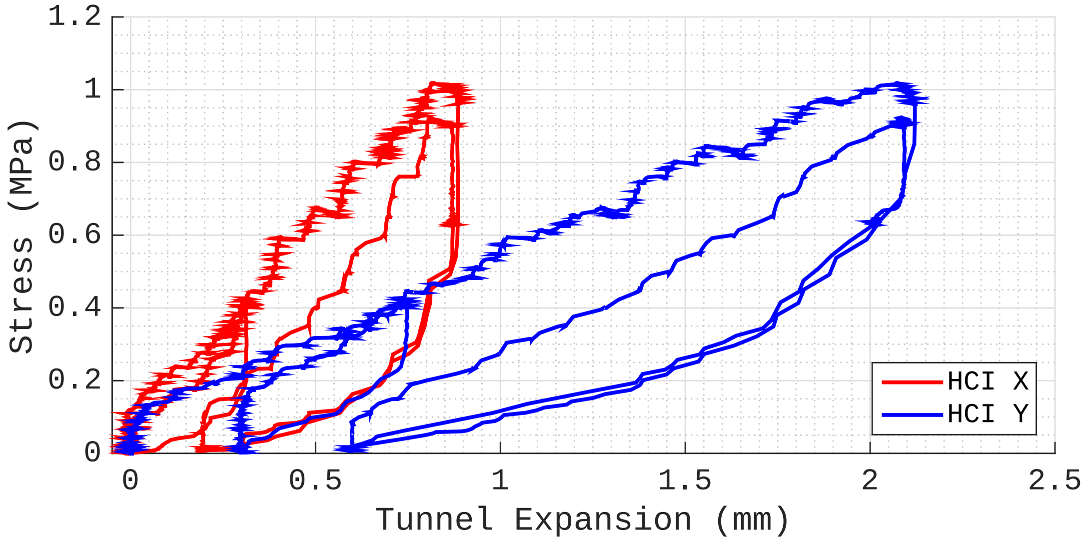

Figure 4.60: Expansion of tunnel opening at HCH experiment

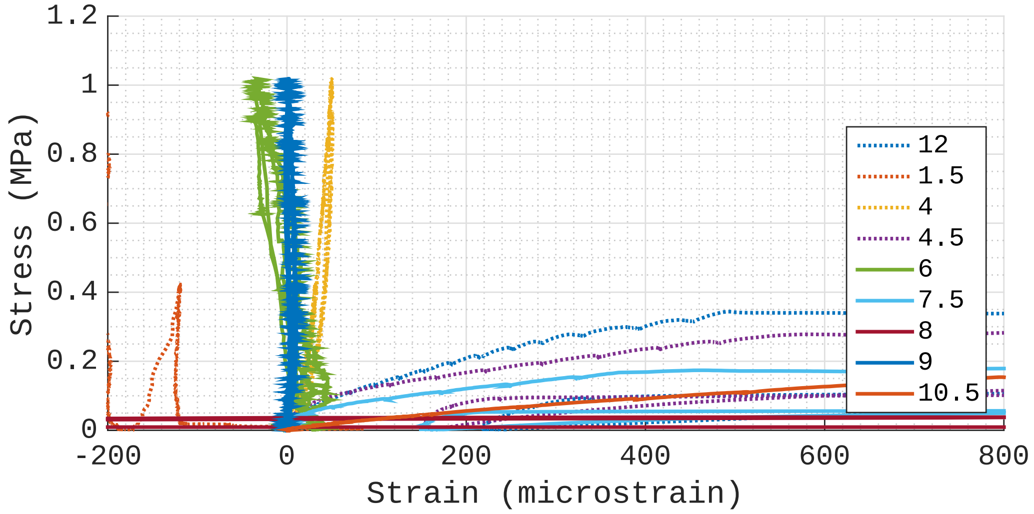

Figure 4.61: Strain readings on lining at HCH experiment

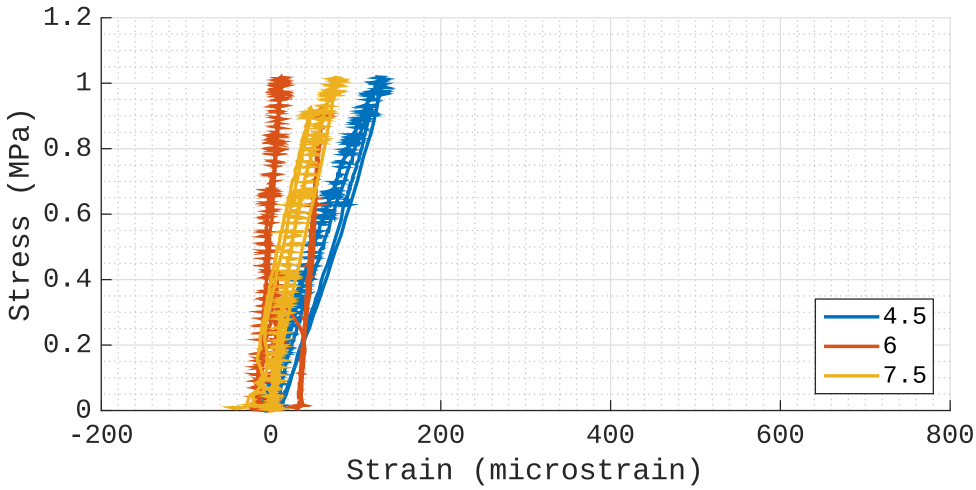

Figure 4.62: Strain readings on rock substitute at HCH experiment

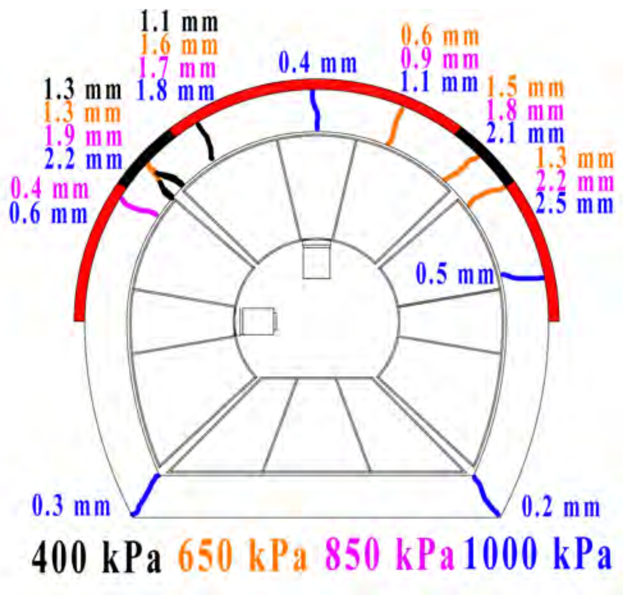

Figure 4.63: Crack map and width measurements at different pressure values during HCH experiment

CHAPTER 5

DISCUSSION OF RESULTS

5.1 Overview

Key variables in seven experiments were the boundary conditions and the material properties of tunnel lining. One experiment was different in that sense; experiment HCIR was conducted to assess performance of FRP-fabric wrap repairing method. Processed data of experiments were the deformations of tunnel opening (Horizontal expansion dotted and vertical expansion as continuous lines), strain states of lining and rock substitute, and resultant crack maps.

Expansion of tunnel opening in principle directions define the stiffness of tunnel behavior. Vertical expansion was almost always greater than horizontal, due to asymmetric geometry of horseshoe shape with respect to x axis. When looked at together, effects of boundary conditions are clearly differentiable on the expansion curves (Fig. 5.1). Largest displacements were seen at NC and NCF experiments without rock substitute, and similar to them, relatively large displacements were observable at LC experiment with rock substitute but without post-tension. Behavior of HCI and HCIF experiments were parallel, ultimate capacities of both laboratory models reached 600 kPa as a result of high level of confinement on the bottom half of interface (Fig. 5.2). At HCH experiment, inwhich the crown of lining was partially in contact with rock substitute, capacity increased to 1 MPa, and also deformation was much smaller (Fig. 5.3). Similar level of pressure was carried by HCP specimen, which has ideal boundary condition. In this experiment, maximum deformation on tunnel opening was smaller than 0.3 mm.

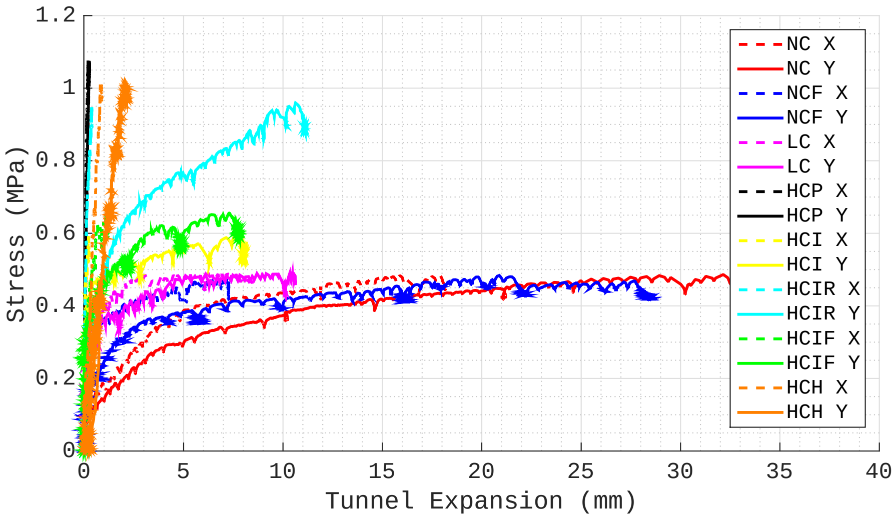

Figure 5.1: Expansion of tunnel openings

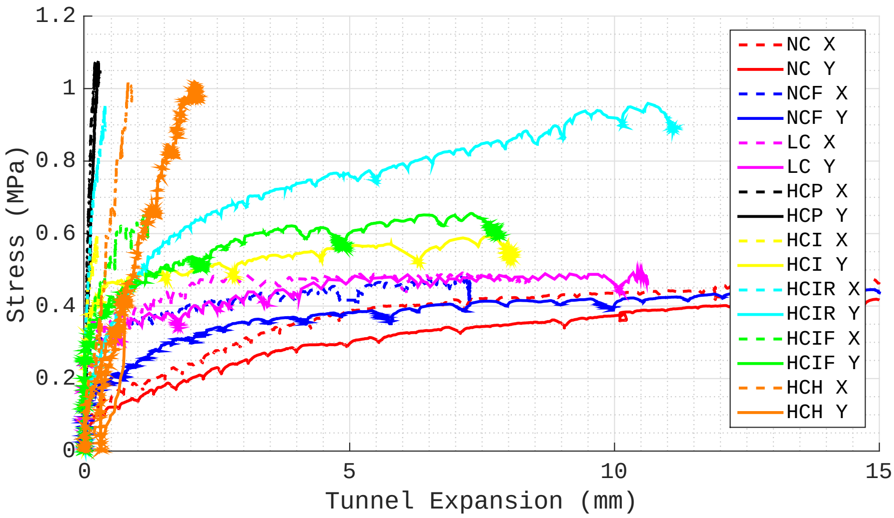

Figure 5.2: Expansion of tunnel openings

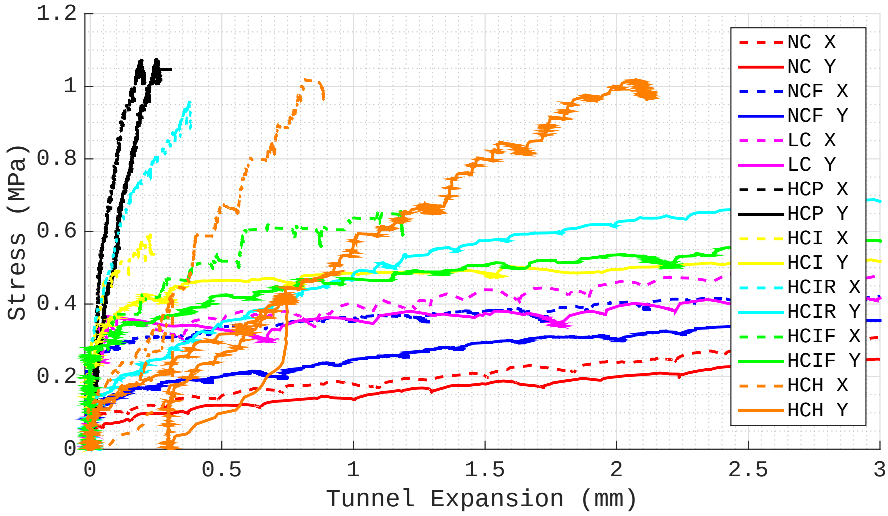

Figure 5.3: Expansion of tunnel openings

5.2 In-Situ Stress Conditions

In-situ stress of tunnel elements depend on the mechanical properties and thickness of outlying stratum. The effect of overburden pressure on tunnel linings become clearly apparent when expansion of tunnel opening in NC, LC and HCP experiments are compared (Fig. 5.4,5.5). Characteristic behavior of the lining is captured with unconfined laboratory model, NC. Expansion that is observable by laboratory equipment starts at 90 kPa inner pressure, and a relatively ductile behavior is maintained until failure at 450 kPa. Resulting crack map is evenly distributed and expansion of cracks are close to uniform. Low level of confinement provided by unstressed intact rock body around lining on LC experiment shifts the deformation initiation instance above 300 kPa, and stiffens the behavior at early stage response. Low elastic modulus of rock caused the substitute layer share relatively low amount of the total load, but this did not help compensating its low tensile capacity. Support of intact rock substitute around lining preserved it from hairline cracks at low levels of inner pressure, until when it failed instantaneously, leading to a large crack at one of the stress concentration areas of lining. Effects of low confinement level are rather drastic: The energy accumulation and its sudden release caused a brittle behavior of the lining, compromising the structural integrity of the system, decreasing the deformability of the lining while not increasing the load capacity notably, relative to NC experiment. As

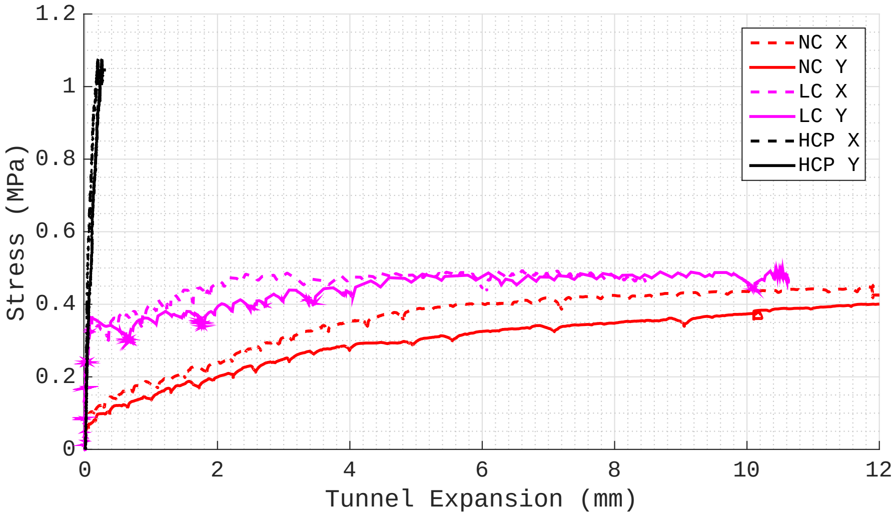

Figure 5.4: Effect of in-situ stress conditions

the level of confinement due to in-situ stress increases, support capacity and stiffness of structural system increase as well: when the overburden pressure is high as inner hydrostatic pressure, four cracks have occurred within tolerable limits. In fact, these cracks were undetectable to naked eye even at 1100 kPa water pressure. Moreover, response of tunnel was very close to linear elastic at reloading scenarios.

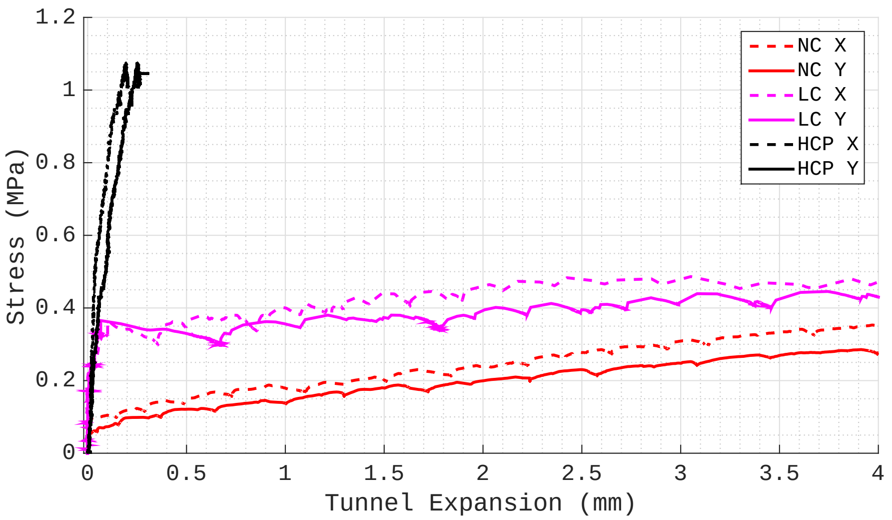

Figure 5.5: Effect of in-situ stress conditions

5.3 Contact Conditions

Effects of contact between outer face of concrete lining and rock layer was investigated in the high in-situ stress condition of weak rock with three experiments: HCP, HCH and HCI. Anticipated zone for the contact loss was selected as the crown of the lining. HCP experimental results shown in Fig. 5.6 with full contact presents an ideal condition. HCH specimen with three separate non-conduct zone shows a decline in stiffness. Although the capacity of this specimen was as high as to that of HCH, the deformation at maximum load was folded 20 times. Furthermore, several deep cracks formed evenly on the crown of the lining. There were no cracks on the bench walls and oncert. It should be noted that tests were conducted under no waer pressure but with mechanically applied pressure. Water can, in reality, penetrate inside the cracks, and may change stress distribution. Soffit voids created between the rock substitute and lining in the crown of HCH specimen caused low stiff response with plastic deformations. The continuous soffit void in the crown of the HCI specimen caused a sharp decline in the load capacity as shown in Fig. 5.6. The load capacity of HCI specimen decreased to as low as NC and LC specimens. The main reason was the loss of contact between the rock substitute and the lining in the vertical direction. The lack of supporting effect of rock caused large vertical deformation and plastic behavior. Consequently, the stiffness and load carrying capacity decreased drastically.

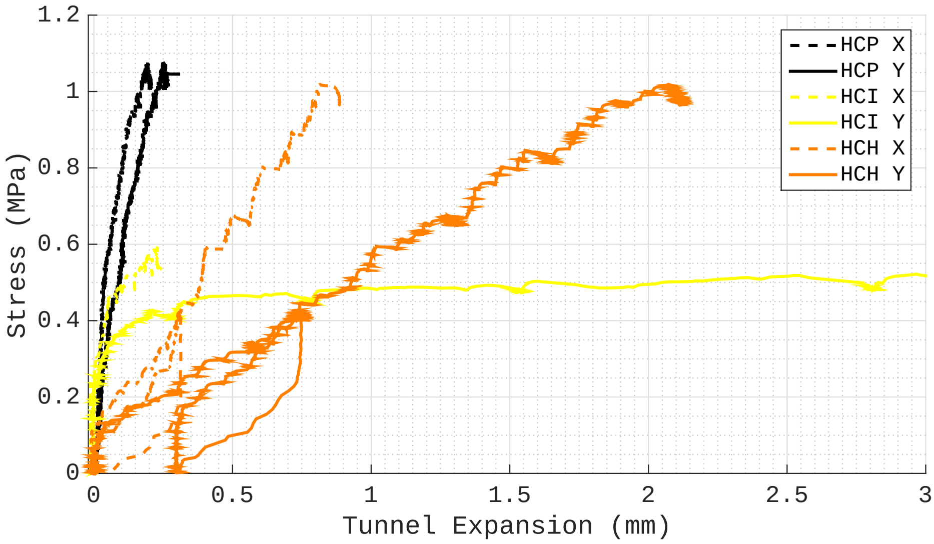

Figure 5.6: Effect of contact conditions

5.4 Performance of Repaired Lining

The efficiency of FRP repairing method was investigated on the damaged laboratory model HCI specimen. The type of loading of the HCI and HCIR experiments were very similar. Evaluation of these two experiments should be made by joining the unloading and loading instances of successive runs (Fig. 5.8 and 5.7). Addition of FRP sheet increased the load capacity of the tunnel. Crack initiation point (at 250 kPa) and propagation point (at 400 kPa) dictated the behavior: stiffness have decreased after 250 kPa and large deformations started after 600 kPa. Pressure increase per unit displacement on the "yield plateaus" doubled after repairing. Moreover, crack incidence on the crown part of the lining increased, 30-cm spaces between consequent cracks became 10 centimeters. The 70% repairing increased the load capacity of the tunnel as high as 0.95 kPa, but delamination occurred at the end of experiment.

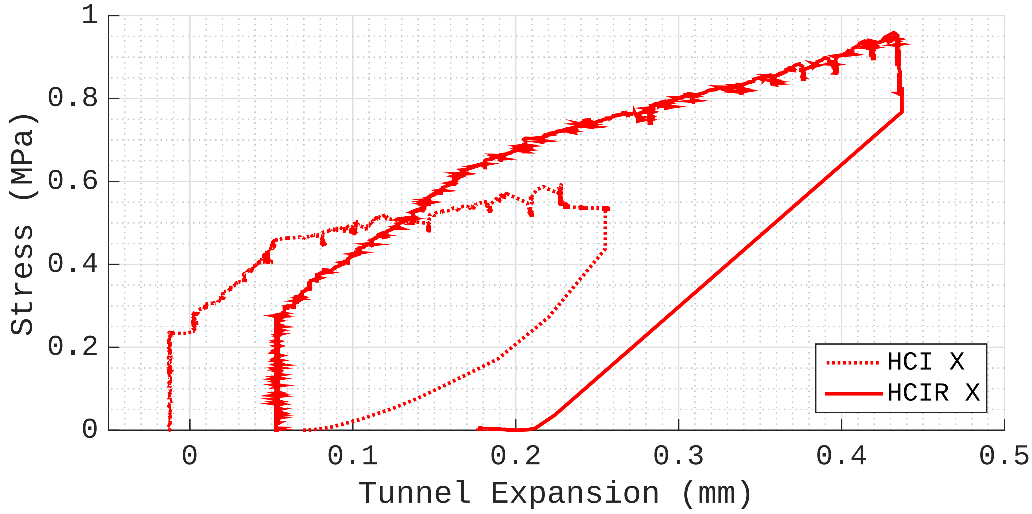

Figure 5.7: Horizontal Tunnel Expansion

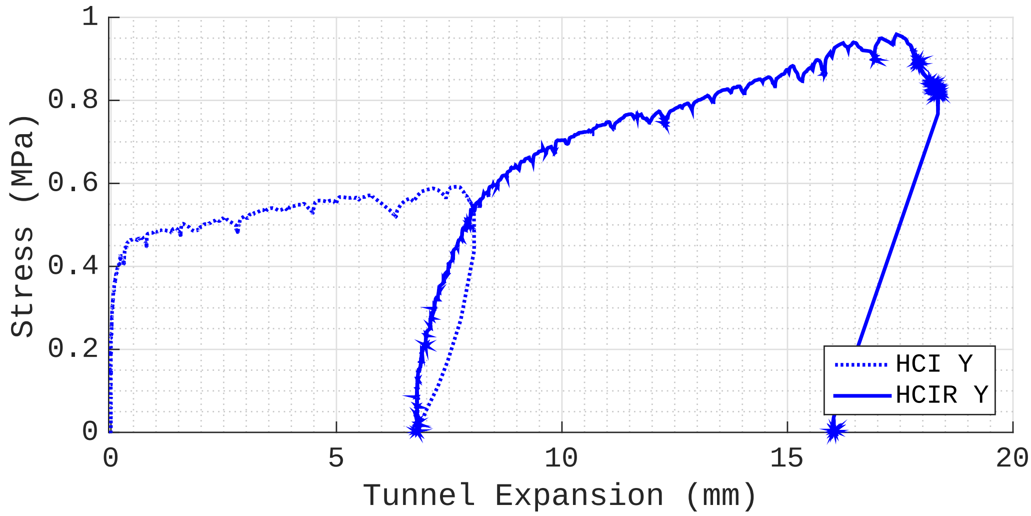

Figure 5.8: Vertical Tunnel Expansion

5.5 Effect of Fibers

Influence of fibers on the behavior of tunnel lining can be examined by comparing the NC-NCF and HCI-HCIF experiments. NC experiment defined the characteristic curve of horseshoe shaped reinforced concrete tunnel. The specimen experienced evenly distributed and deep cracks. On the NCF experiment, however, hairline cracks were not able to propagate early stage response was stiffer, and geometrical weakness points dominantly shaped the ultimate capacity of experimental model. Thus, the ratio between vertical and horizontal tunnel expansions were abruptly different on large scaled deformation. On the other two experiments, HCI and HCIF, corners on invert confined with equal level of pressure, and vertical expansion of tunnel was only possible towards crown area, where the contact condition was imperfect. The addition of fibers slightly increased the ultimate capacity, and the resultant expansion curve of HCIF experiment was similar to that of HCI. Most significant influence of fibers was the even distribution of cracks on crown.

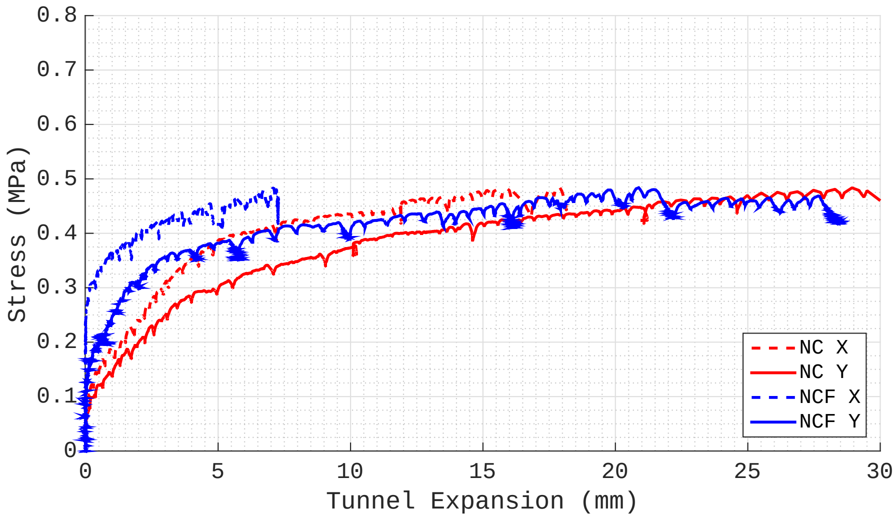

Figure 5.9: Tunnel Expansion at NC and NCF experiments

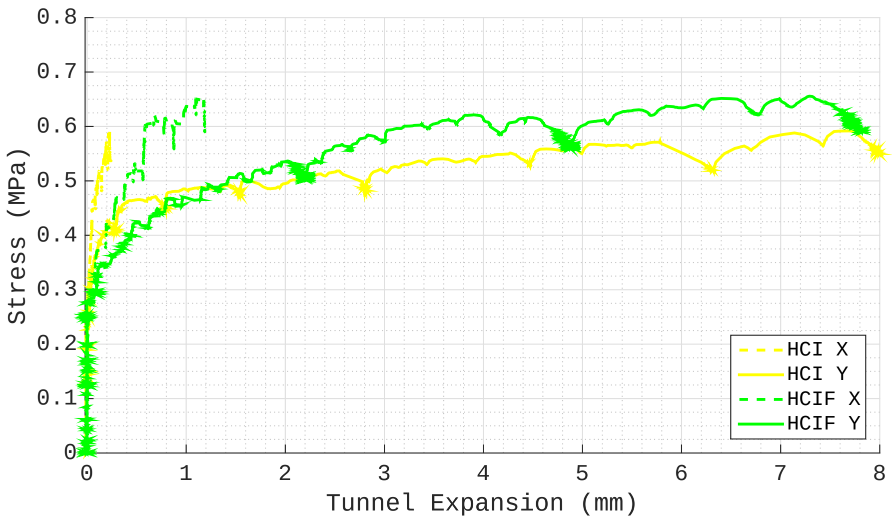

Figure 5.10: Tunnel Expansion at HCI and HCIF experiments

5.6 Notes on DIC Results

Beyond tunnel expansion measurements, crack detection and measurement was of vital importance for this experimental study. Use of digital image correlation greatly contributed to that extent. DIC-calculated horizontal and vertical opening measurements were following the trend of classical measurements, but in scaled magnitudes. Impressive attribute of DIC was the detection of cracks before they were visible. After DIC was done, the zone of crack was examined at the sequential images of interest, and virtually no crack has been found. But the calculated strain values exceeded crack limit and a while later, a crack occurs on the exact location and pattern as calculated. This also helped us locate several plastic deformations that were missed in inspection with naked eye.

5.7 Notes on Serviceability Limits

For the failure criteria that are caused by cracks may be listed as the loss of water, water head and the integrity of the lining. The ultimate and catastrophic limit is the loss of structural integrity of the lining. Putting the ultimate limit aside, the efficiency of turbines is a function of outflow from the tunnel, among other things. For the estimation of leakage, crack widths must be calculated. The key parameters horizontal and vertical tunnel expansion ($2\Delta R$) is critical in that sense. The change in perimeter of a circle (Eqn. 5.1) is defined by the change in diameter, $2\Delta R$.

$$\begin{aligned} P &= 2\pi R \\ \Delta P &= 2\pi \Delta R \end{aligned} \tag{5.1}$$

Physically, This value is equal to the elastic and plastic deformation.

$$\Delta P = \Sigma w_i + P\varepsilon_{el} \tag{5.2}$$

Put together, the sum of crack widths along circumference is given by;

$$\begin{aligned} \Sigma w_i &= 2\pi\Delta R - P\varepsilon_{el} \\ &= \pi(2\Delta R) - 2\pi R\varepsilon_{el} \end{aligned} \tag{5.3}$$

where $2\Delta R$ is the measured quantity, and π, the radius R, and the maximum elastic strain ε_{el} are all constants. When the laboratory specimen is examined with Eqn. 5.3, $0.72m$ radius and $\varepsilon_{el} = 10^{-4}$ are inserted, Eqn. 5.4 is obtained for crack width in millimeters. Fig. 5.11 shows the crack widths at maximum load. The calculations are made for circular cross-sections, in other words the complexities caused by horse-shoe geometry is simplified. Similarly, the parametric equation that gives the exact perimeter of an ellipse is rather complex, and the errors of approximations are moderately high (i.e. Euler approximation %5), therefore an interval is given for the total crack widths at Fig. 5.11.

$$\Sigma w_i[mm] = \pi\big[(2\Delta R) - 0.144\big] \tag{5.4}$$

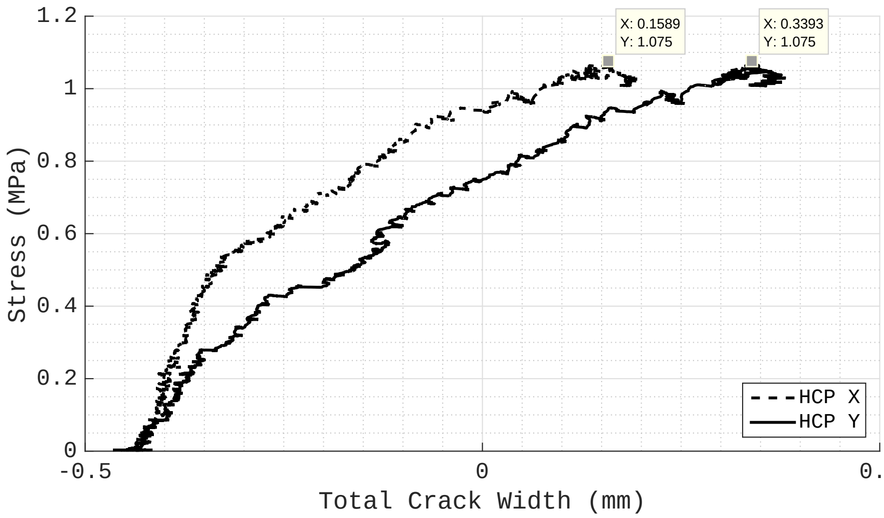

Figure 5.11: Crack widths at HCP experiment

After HCP experiment, four cracks that were not visible to eye were found thanks to DIC application. From Fig. 5.11, lower and upper total crack width limits are $\Sigma w_{i1} = 0.1589$ and $\Sigma w_{i2} = 0.3393$, respectively. If the crack widths are the same, the average crack width must be between $\bar{w}_1 = 0.1589/4 = 0.039725mm$ and $\bar{w}_2 = 0.3393/4 = 0.084825mm$.

At the HCIR experiment, there were 24 cracks, largest one 3.5 mm-wide, summation of crack widths were 36.5 mm, and the average crack width was 1.5208 mm according to 4.50. Fig. 5.12 represent the total crack width calculation made with Eqn. 5.4, lower and upper crack width limits as $\Sigma w_{i1} = 0.7414$ and $\Sigma w_{i2} = 34.43$, leading to 24 equal cracks of $\bar{w}_1 = 0.0309mm$ and $\bar{w}_2 = 1.4346mm$. This result shows the accuracy of the calculation.

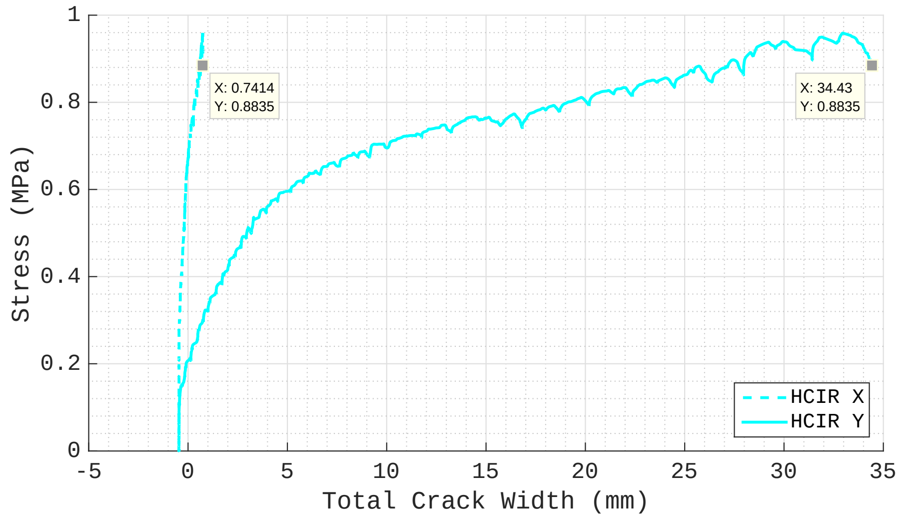

Figure 5.12: Crack widths at HCP experiment

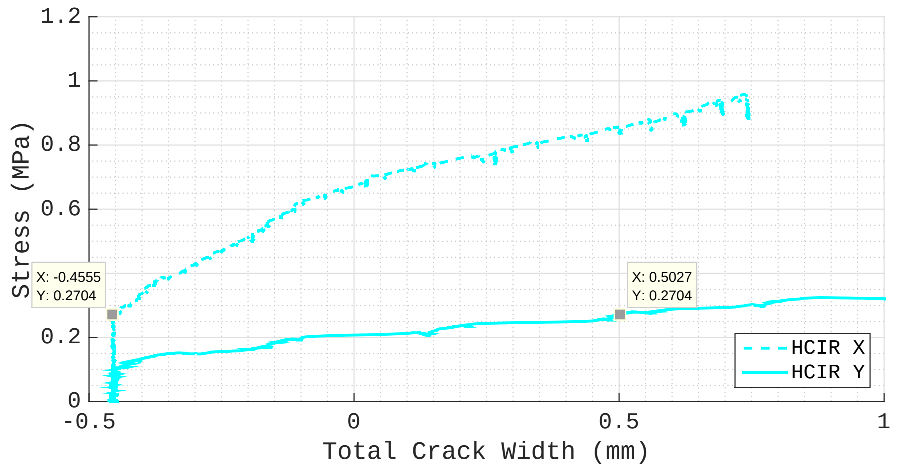

Figure 5.13: Crack widths at HCP experiment

However the serviceability limits for such a tunnel is far below these values. Fig. 5.13 shows the behavior of HCIR specimen up to $0.5mm$ total crack width, which is equivalent to the limit of five hairline cracks. With average crack widths and number of cracks in hand, the outflow from the tunnel can be calculated, by assuming laminar flow through cracks with a parabolic velocity profile between long walls (Eqn. 5.5)

$$\bar{V} = \frac{w^2}{12\mu}\frac{\Delta P}{\Delta x} \tag{5.5}$$

with $\bar{V}$ the average velocity, w the crack width, μ the viscosity, ΔP the pressure difference between inside and outside of lining, and Δx, the length of the crack. The discharge is calculated over the length L with Eqn. 5.6.

$$\begin{aligned} Q &= \bar{V}A \\ &= \frac{w^2}{12\mu}\frac{\Delta P}{\Delta x}wL \\ &= \frac{w^3}{12\mu}\frac{\Delta P}{\Delta x}L \end{aligned} \tag{5.6}$$

Equation 5.6 shows that the leakage increases with the cube of the crack width whereas the number of cracks remains linear. This implies the importance of crack propagation control. Implementation of the Eqn. 5.6 to the specimen with one one-meter-long hairline crack yields;

$$\begin{aligned} Q &= \frac{(10^{-4})^3}{12(10^{-3})}\frac{200000}{0.17}1 \\ &= 9.8039 \times 10^{-5} m^3/s \end{aligned} \tag{5.7}$$

A fairly small discharge, from one hairline crack. When the same equation is applied to the model tunnel, with 40 cm lining, three 1-kilometer-long cracks with 0.5 to 1 mm width, a massive amount of water is lost to rock body, Eqn. 5.8.

$$\begin{aligned} Q &= 3 \times \frac{(5 \times 10^{-4})^3}{12(10^{-3})}\frac{200000}{0.40}1000 \\ &= 15.6250 m^3/s \end{aligned} \tag{5.8}$$

Fig. 5.14 is obtained by implementing Eqn. 5.6 to a 40 cm thick lining with 100 meter long cracks, n being number of cracks, and again an arbitrary pressure difference of 200 MPa between inside and outside of lining. Solutions of 1.5 mm total crack width along circumference is marked at $n = 1, 2, 10$.

Although these calculations are not exact for the horseshoe shaped pressure tunnels, the degrees of water loss is close to reality. It must be noted that the pressure difference, length of a continuous crack and thickness of lining affect Q linearly and

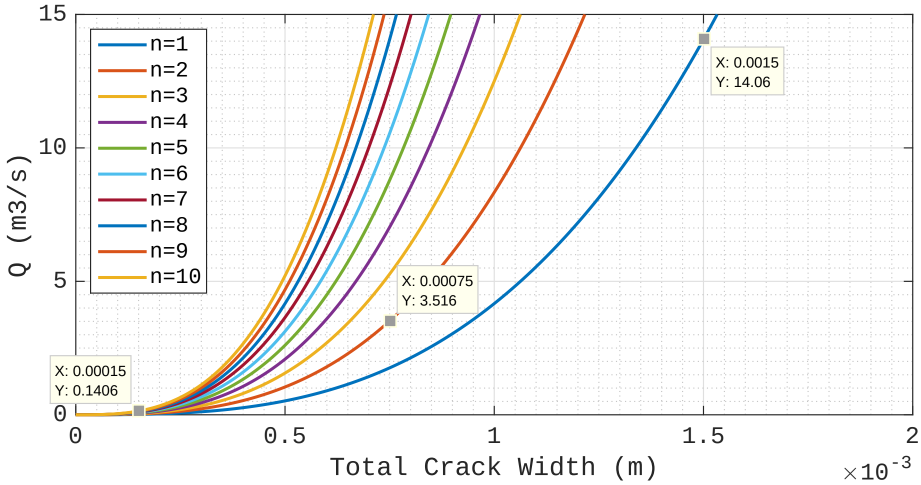

Figure 5.14: Crack width vs Leakage for 100-meter-long cracks at a 40-cm-thick lining

can be adjusted at the structural design stage, and w can be controlled with material properties.

CHAPTER 6

CONCLUSIONS

To the best of author's knowledge, this is the first experimental study that is carried out on horseshoe shaped reinforced concrete pressure tunnels in a controlled laboratory environment. The setup was prepared as a 40% scaled model of pressure tunnel at Topçam Dam in Ordu Province, Turkey. Effects of in-situ stress conditions, contact quality of rock-lining interface, material properties of lining and the performance of FRP-sheet repair method were investigated experimentally with a novel approach.

Eight distinct experiments were set up with a novel approach in order to investigate effects of in-situ conditions of pressure tunnels, contact conditions of rock-lining interface, and material properties of lining to the behavior of lining. During experiments, a special concrete mixture and AAC structure was successfully implemented as rock substitute. DIC was applied for the analysis. Stiffness of lining is related to the linear deformations of tunnel opening in horizontal and vertical axes, these are functions of elastic and plastic deformations along the perimeter of the lining. Therefore, all data was analyzed with respect to horizontal and vertical linear displacements.
In the light of the experimental data;

- the confining effects of overburden pressure on pressurized tunnels: increase in stiffness, restriction of crack openings, is stated numerically,
- Results of inadequate contact quality and intermittent discontinuities were shown,
- Increase of crack count and decrease of average crack width when the addition of synthetic fibers to the lining mixture is clearly stated,
- FRP-wrap reinforcement methods success to maintain stiffness and boost capacity was demonstrated.

REFERENCES

[1] R. Aghlara and M. M. Tahir. Measurement of strain on concrete using an ordinary digital camera. *Measurement*, may 2018.

[2] N. Barton, R. Lien, and J. Lunde. Engineering classification of rock masses for the design of tunnel support. *Rock mechanics*, 6(4):189–236, Dec 1974.

[3] C. B. Basnet and K. K. Panthi. Analysis of unlined pressure shafts and tunnels of selected norwegian hydropower projects. *Journal of Rock Mechanics and Geotechnical Engineering*, 10(3):486 – 512, 2018.

[4] J. F. Bell. Diffraction grating strain gage. *Proceedings of the S.E.S.A.*, XVII)(2):51–64, 1959.

[5] Z. Bieniawski. Engineering classification of jointed rock masses. *Civil Engineering = Siviele Ingenieurswese*, 1973(v15i12):335–343, 1973.

[6] Z. BIENIAWSKI. 22 - classification of rock masses for engineering: The {RMR} system and future trends. In J. A. HUDSON, editor, *Rock Testing and Site Characterization*, pages 553 – 573. Pergamon, Oxford, 1993.

[7] A. Bilotta, F. Ceroni, G. Lignola, and A. Prota. Use of DIC technique for investigating the behaviour of FRCM materials for strengthening masonry elements. *Composites Part B: Engineering*, 129:251–270, nov 2017.

[8] D. Brewster. Xv. on the effects of compression and dilatation in altering the polarising structure of doubly refracting crystals. *Transactions of the Royal Society of Edinburgh*, 8(2):283–286, 1818.

[9] C. Broniewska, S. Mitra, and B. Met. Photoelastic method for stress analysis. `http://eprints.nmlindia.org/3484/1/266-275.PDF`. Accessed: 2018-06-04.

[10] D. Brox. Technical considerations for tbm tunneling for mining projects. *TRANSACTIONS OF THE SOCIETY FOR MINING, METALLURGY, AND EXPLORATION*, 334:498–505, 2013.

[11] N. N. Eldin and A. B. Senouci. Measurement and prediction of the strength of rubberized concrete. *Cement and Concrete Composites*, 16(4):287–298, jan 1994.

[12] R. Goel, J. Jethwa, and A. Paithankar. Indian experiences with q and rmr systems. *Tunnelling and Underground Space Technology*, 10(1):97 – 109, 1995.

[13] J.-L. Granju and S. U. Balouch. Corrosion of steel fibre reinforced concrete from the cracks. *Cement and Concrete Research*, 35(3):572 – 577, 2005.

[14] C. Grobbelaar. The degradation and failure of concrete linings around water conveyance tunnels. *Tunnelling and Underground Space Technology*, 9(1):67–71, 1994.

[15] E. Hoek and E. Brown". "practical estimates of rock mass strength". *"International Journal of Rock Mechanics and Mining Sciences"*, "34"("8"):"1165 – 1186", "1997".

[16] E. Hoek and E. Brown. The hoek–brown failure criterion and GSI – 2018 edition. *Journal of Rock Mechanics and Geotechnical Engineering*, 11(3):445–463, June 2019.

[17] E. Hoek and T. Brown. Empirical strength criterion for rock masses. *Journal of Geotechnical and Geoenvironmental Engineering*, 106:1013–1035, 09 1980.

[18] E. Hoek and M. Diederichs. Empirical estimation of rock mass modulus. *International Journal of Rock Mechanics and Mining Sciences*, 43:203–215, 02 2006.

[19] R. Hooton, D. Goulias, and A.-H. Ali. Evaluation of rubber-filled concrete and correlation between destructive and nondestructive testing results. *Cement, Concrete and Aggregates*, 20(1):140, 1998.

[20] R. Hooton, M. Nehdi, and A. Khan. Cementitious composites containing recycled tire rubber: An overview of engineering properties and potential applications. *Cement, Concrete and Aggregates*, 23(1):3, 2001.

[21] F. Huang, H. Zhu, Q. Xu, Y. Cai, and X. Zhuang. The effect of weak interlayer on the failure pattern of rock mass around tunnel – scaled model tests and numerical analysis. *Tunnelling and Underground Space Technology*, 35:207–218, apr 2013.

[22] IEA. Technology roadmap hydropower. `http://www.iea.org/publications/freepublications/publication/2012_Hydropower_Roadmap.pdf`. Accessed: 2018-06-07.

[23] C. Jin, M. Soltani, and X. An. Experimental and numerical study of cracking behavior of openings in concrete dams. *Computers & Structures*, 83(8):525 – 535, 2005.

[24] H. G. Jodl and D. Resch. Natm and tbm – comparison with regard to construction operation / nÖt und tbm – eine baubetriebliche gegenüberstellung. *Geomechanics and Tunnelling*, 4(4):337–345, 2011.

[25] H. Kastner. *Statik des Tunnel- und Stollenbaues*. Springer Berlin Heidelberg, 1971.

[26] A. Laderian and M. A. Abaspoor. The correlation between rmr and q systems in parts of iran. *Tunnelling and Underground Space Technology*, 27(1):149 – 158, 2012.

[27] H.-H. Lee. *Model Studies of a Tunnel in Stratified Rock*. PhD thesis, McGill University, Department of Mining and Metallurgical Engineering McGill University, Montreal, Canada, 11 1973.

[28] C. Leung and M. Meguid. An experimental study of the effect of local contact loss on the earth pressure distribution on existing tunnel linings. *Tunnelling and Underground Space Technology*, 26(1):139–145, jan 2011.

[29] S. Li, Q. Wang, H. Wang, B. Jiang, D. Wang, B. Zhang, Y. Li, and G. Ruan. Model test study on surrounding rock deformation and failure mechanisms of

deep roadways with thick top coal. *Tunnelling and Underground Space Technology*, 47:52–63, mar 2015.

[30] Y. Li, D. Zhang, Q. Fang, Q. Yu, and L. Xia. A physical and numerical investigation of the failure mechanism of weak rocks surrounding tunnels. *Computers and Geotechnics*, 61:292–307, sep 2014.

[31] P. Lin, H. Liu, and W. Zhou. Experimental study on failure behaviour of deep tunnels under high in-situ stresses. *Tunnelling and Underground Space Technology*, 46:28–45, feb 2015.

[32] R. D. Mindlin. A review of the photoelastic method of stress analysis. i. *Journal of Applied Physics*, 10(4):222–241, apr 1939.

[33] K. Najim and M. Hall. A review of the fresh/hardened properties and applications for plain- (PRC) and self-compacting rubberised concrete (SCRC). *Construction and Building Materials*, 24(11):2043–2051, nov 2010.

[34] B. of Indian Standard. *CODE OF PRACTICE FOR DESIGN OF TUNNELS CONVEYING WATER- Part 4 Structural design of concrete lining in rock*. Indian Standard Bureau, 1971.

[35] B. of Indian Standard. *CODE OF PRACTICE FOR DESIGN OF TUNNELS CONVEYING WATER- Part 4 Structural design of concrete lining in soft strata and soils*. Indian Standard Bureau, 1972.

[36] B. of Indian Standard. *Criteria for Structural Design of Penstocks*. Indian Standard Bureau, 1986.

[37] B. of Indian Standard. *CODE OF PRACTICE FOR DESIGN OF TUNNELS CONVEYING WATER- Part 1 General Design*. Indian Standard Bureau, 1987.

[38] A. Palmström. Combining the rmr, q, and rmi classification systems. *Tunnelling and Underground Space Technology*, 24(4):491 – 492, 2009.

[39] A. Palmstrom. Norwegian design and construction experiences of unlined pressure shafts and tunnels. 1987.

[40] W. H. Peters, W. F. Ranson, M. A. Sutton, T. C. Chu, and J. Anderson. Application of digital correlation methods to rigid body mechanics. *Optical Engineering*, 22(6), dec 1983.

[41] T. R. Pryor and W. P. T. North. The diffractographic strain gage. *Experimental Mechanics*, 11(12):565–568, dec 1971.

[42] L. Rabcewicz. The new austrian tunnelling method. *Water Power*, 16(11):453–457, 1964.

[43] S. Raffoul, R. Garcia, K. Pilakoutas, M. Guadagnini, and N. F. Medina. Optimisation of rubberised concrete with high rubber content: An experimental investigation. *Construction and Building Materials*, 124:391–404, oct 2016.

[44] K. Ramesh, T. Kasimayan, and B. N. Simon. Digital photoelasticity – a comprehensive review. *The Journal of Strain Analysis for Engineering Design*, 46(4):245–266, may 2011.

[45] J. Rand and D. Grant. Optical measurement of biaxial strain in thin film polymers. In *Nontraditional Methods of Sensing Stress, Strain, and Damage in Materials and Structures*, pages 123–123–15. ASTM International.

[46] E. Romeo and A. Montepara. Characterization of reinforced asphalt pavement cracking behavior using flexural analysis. *Procedia - Social and Behavioral Sciences*, 53:356–365, oct 2012.

[47] J. C. Ruthledge. Experience with engineering classifications of rock. *Proc. Int. Tunnelling Sym*, 1978.

[48] T. S. and G. J.N. 1952.

[49] R. SINHA. Underground structures in rock. In *Developments in Geotechnical Engineering*, pages 159–202. Elsevier, 1989.

[50] J. Standing and C. Lau. Small-scale model for investigating tunnel lining deformations. *Tunnelling and Underground Space Technology*, 68:130–141, sep 2017.

[51] J. R. Standing, D. M. Potts, R. Vollum, J. B. Burland, A. Tsiampousi, and S. Afshan. Investigating the effect of tunnelling on existing tunnels. In *Proc. Underground Design and Construction Conference 2015*, pages 301–312. IOM3 Hong Kong Branch, 2015.

[52] G. Sun, X. Liu, G. Zheng, Z. Gong, and Q. Li. On fracture characteristics of adhesive joints with dissimilar materials - an experimental study using digital image correlation (DIC) technique. *Composite Structures*, jun 2018.

[53] K. Terzaghi. *Theoretical Soil Mechanics*. John Wiley and Sons, 1943.

[54] TSE. Ts648 Çelik yapilarin hesap ve yapim kurallari, building code for steel structures, 1980.

[55] S.-H. Tung and C.-H. Sui. Application of digital-image-correlation techniques in analysing cracked cylindrical pipes. *Sadhana*, 35(5):557–567, oct 2010.

[56] A. Turatsinze and M. Garros. On the modulus of elasticity and strain capacity of self-compacting concrete incorporating rubber aggregates. *Resources, Conservation and Recycling*, 52(10):1209–1215, aug 2008.

[57] G. Wickham, H. Tiedemann, and E. Skinner. Support determinations based on geologic predictions. *International Journal of Rock Mechanics and Mining Sciences & Geomechanics Abstracts*, 12(7):95, 1975.

[58] G. E. Wickham, H. R. Tiedemann, and E. H. Skinner. Support determinations based on geologic predictions. In *13R. PROCEEDINGS RETC. AIMMPE*, pages 43–64, 1972-6.

[59] S.-Q. Yang, M. Chen, H.-W. Jing, K.-F. Chen, and B. Meng. A case study on large deformation failure mechanism of deep soft rock roadway in xin'an coal mine, china. *Engineering Geology*, 217:89–101, jan 2017.

[60] O. Youssf, R. Hassanli, and J. E. Mills. Mechanical performance of FRP-confined and unconfined crumb rubber concrete containing high rubber content. *Journal of Building Engineering*, 11:115–126, may 2017.

[61] J. Yu, J. Standing, R. Vollum, D. Potts, and J. Burland. Experimental investigations of bolted segmental grey cast iron lining behaviour. *Tunnelling and Underground Space Technology*, 61:161–178, jan 2017.

[62] S. Zare, A. Bruland, and J. Rostami. Evaluating d&b and tbm tunnelling using ntnu prediction models. *Tunnelling and Underground Space Technology*, 59:55 – 64, 2016.

APPENDIX A

UNIFORM ROCK SUBSTITUTE

Elastic modulus of concrete is mainly a function of maximum aggregate size and mechanical properties of aggregates. Several nonlinear relations between compressive strength and elastic modulus of concrete can be found in the literature Ersoy et al (2010), ASTM C469. Most of these equations set a lower bound to the modulus of elasticity. Since the required elastic modulus is lower than these minima, a change in the fundamental components of concrete was needed. There are experiments of aggregate replacements with chipped wood and crushed concrete in the literature. After they were examined, numerous trials were made by adding slag, lime, perlite and rubber while decreasing the cement and aggregate content. Most successful results among these trials were achieved by replacing crushed rock aggregates with rubber aggregates. Since rubber is among the materials with lowest elastic modulus (10-100 MPa), it was the perfect candidate to efficiently lower the overall rigidity of the material.

Examples of replacement of crushed stone to rubber aggregate are present in the literature, Goulias and Ali, (1998), Nehdi and Khan (2001), Najim and Hall (2010), Raffoul et al. (2016), Youssf et al. (2017). The interest in rubber additives to concrete (often referred as rubberized concrete) is induced by high ductility of rubber. An often desired characteristic on pavements, floorings and motorways. Together with the non-recyclability and very poor salvage values of used tires, the use of shredded tires in concrete as a filler material seemed as a great and green opportunity. Eldin and Senouci (1993) have experimented by replacing both fine and coarse aggregates separately, and have reported a 85% decrease in compressive strength with coarse aggregates. When the replacement was made between fine aggregates and crumb

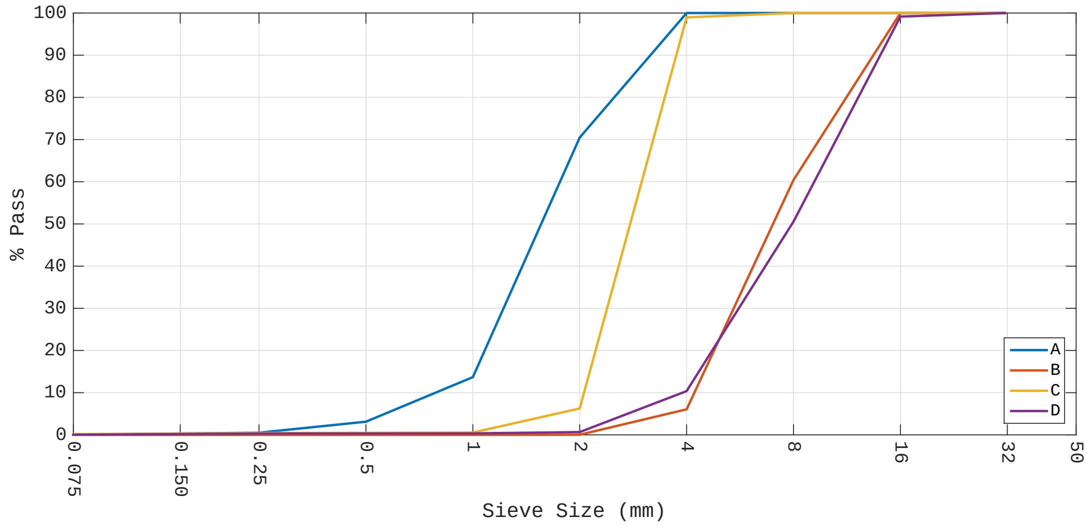

Figure A.1: Gradation of rubber particles

rubber, decrease was 65%. Another important case was the flexural experiments conducted by Turatsinze and Garros (2008). When the one fourth of the fine aggregate was replaced with rubber, flexural strength was reduced to one third of control group, while the deformation at maximum load doubled. The calculated modulus of elasticity from these experiments were promising. This is why production and efficiency of rubberized concrete was investigated.

Mechanical properties of rubberized concrete were assessed to be used on laboratory model. Rubber particles were obtained from a local tire shredding facility. Tires are processed using either mechanical disintegration by different shredders for different sizes, and/or with chemical processes. Chemical processing is done in order to obtain steel reinforcements on tires, therefore only mechanically processed shreds were acquired from the facility. Samples from four batches with different sizes of rubber were subjected to sieve analysis and specific gravity tests in Construction Materials Laboratory, METU. The gradation process is done in accordance with Turkish Standard for Lightweight aggregates - Part 1:Lightweight aggregates for concrete, mortar and grout TS 1114. Results indicate that two sample groups were consisting of mostly fine aggregates, other two were more evenly distributed on coarse aggregate region (Fig. A.1).

The specific gravity test was conducted according to ASTM C128, since rubber par-

Table A.1: Rubberized concrete mix design

Components	Control (kg/m^3)	%50 (kg/m^3)	%100 (kg/m^3)
CEM II/B-M (P-L 42.5R)	300	300	300
Water	195	195	195
Aggregate (0-3 mm)	930.3	930.3	930.3
Aggregate (3-12 mm)	933.8	466.9	0
Rubber (Batch A)	0	184.7	369.3
Total	2359.1	2076.9	1794.6

ticles were floating and even though samples B and D were classified as coarse aggregates, ASTM C127 (Specific weight for coarse test) becomes inapplicable. When the sample was introduced to a laboratory flask filled with water, less than half of the particles were floating. After stirring and clearing all water bubbles and waiting the mixture to settle, the specific weight of rubber samples were calculated to be 1.06. Since the rubber particles were light, the replacement of aggregates was done by volume (table A.1). In the scope of preliminary study, two proportions of coarse aggregate replacements were decided to be made with crumb rubber as %50 and %100, with a control group.

For three different batches, six cylindrical ($100mm \times 200mm$) and three prismatic ($75 \times 75 \times 325mm$) samples per group were casted. Compressive strength test were conducted on 7^{th} and 28^{th} days. Tests for flexural strength were made at 28^{th} day. Elasticity moduli were calculated from the displacement driven compression tests (Fig. A.2).

High ductile behavior of rubberized samples can be seen from both stress-strain diagram (Fig. A.2) and failure planes of samples (Fig. A.3) after compressive strength test. However, a sharp decrease of compressive strength was observed. Moreover, inconsistencies were seen in the modulus of elasticity tests (Table A.2). Consequently, it was decided to abandon the idea of use of rubber aggregate concrete as rock substitute model.

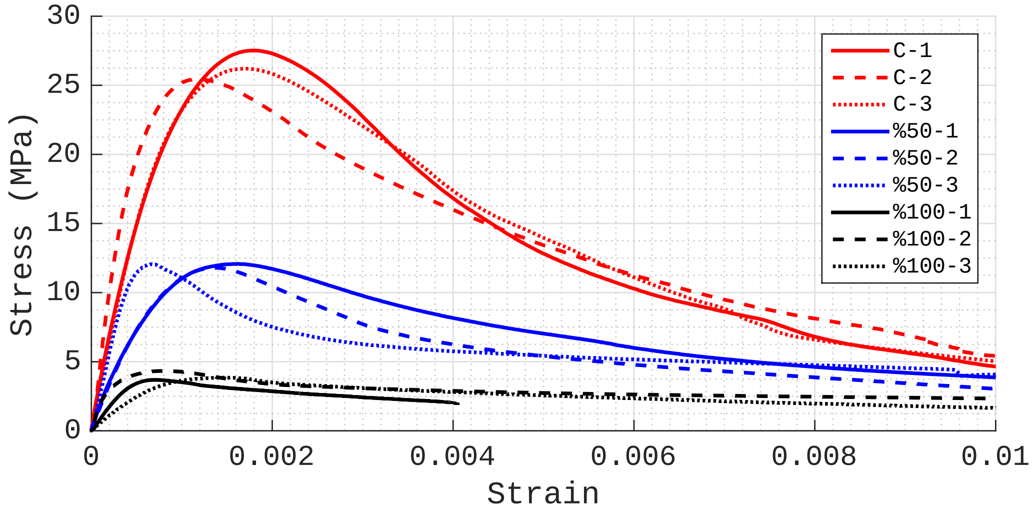

Figure A.2: Results of rubberized concrete samples

Figure A.3: Rubberized concrete samples after compression test: %100, %50 and control groups from left to right

Table A.2: Results of rubberized concrete

Material Parameters	Sample number	Control Group	%50 Rubber	%100 Rubber
Compressive Strength (MPa)	1	27.52	12.08	3.69
	2	25.46	11.80	4.33
	3	26.20	12.06	3.85
	Mean	**26.40**	**11.98**	**3.96**
Modulus of Elasticity (GPa)	1	32.63	28.04	9.24
	2	50.72	14.12	21.93
	3	31.62	13.91	5.16
	Mean	**38.32**	**18.67**	**12.11**